

Path Instabilities of a Rising or Falling Sphere in a Fluid at Rest - An Experimental Study

Shravan Raaghav K R

Technische Universiteit Delft

Path Instabilities of a Rising or Falling Sphere in a Fluid at Rest - An Experimental Study

by

Shravan Raaghav K R

to obtain the degree of Master of Science
at the Delft University of Technology,
to be defended publicly on November 29, 2019.
P & E Report Number: 3002

| | | |
|-------------------|---|---|
| Student number: | 4740475 | |
| Project duration: | November 1, 2018 - November 29, 2019 | |
| Thesis committee: | Dr.ir. Wim-Paul Breugem, Prof.Dr.ir. Christian Poelma, Dr.ir. Daniel Tam, | TU Delft, supervisor TU Delft, co-supervisor TU Delft |

An electronic version of this thesis is available at <http://repository.tudelft.nl/>.

Preface

This thesis marks the fulfilment of the required number of credits to be obtained for the Masters in Mechanical Engineering program under the track 'Energy and Process Technology' at the Delft University of Technology. The research was carried out in the Laboratory of Aero- and Hydrodynamics, Department of Process and Energy under the supervision of Dr.ir.Wim-Paul Breugem and co-supervision of Prof.Dr.ir.Christian Poelma. The present work deals with the design of an experimental setup and the development of image processing tools to study the path instabilities involved in a single sphere freely falling/rising in a quiescent fluid.

The image in the cover page used in this report is taken from the dye visualization study of Horowitz and Williamson [1]. This report aims to provide a detailed documentation of the entire experimental campaign and discusses the results obtained thereof. The reader interested in the physics of path instabilities is directed to the introduction section (chapter 1) and directly to the results and discussion section (chapter 3). The reader interested in performing similar experiments/repeating experiments is directed to Appendix I and Appendix J, where the experimental procedure and the intricacies involved are presented, as this can save much time for one wanting to perform similar experiments (say for disks/spheroids etc).

Constructive criticisms on the structure presentation of the report are welcome and I take responsibility for any flaw or loss of clarity in the report. Criticisms on any conceptual/logical flaw in the report is also welcome as I am ready to unlearn and relearn. The idea is to make the experimental data available for any form of reference or validation of numerical models. The data corresponding to the plots in the report can be obtained upon request. An experimental investigation of the wake structure by using dye visualizations and investigation to characterize the moment of inertia of the spheres is currently in progress.

Shravan Raaghav K R
Delft, November 2019

Acknowledgements

This work wouldn't have been possible without the help of many people. I would like to take this opportunity to profusely thank all of them. I would like to thank **Edwin** for always seeing to that I always had a pair of cameras to work with and for generously giving his time for troubleshooting various issues I faced. I have taken a lot of help from **Jasper** for fabricating many components to build the entire experimental setup for which I am always grateful. I would like to extend my gratitude to **Jan** for helping me with the wiring of the Arduino and calibration of the temperature sensor. The timely help offered in providing access to the Chemical lab and allowing me to use possibly anything in the lab by **Michel** is highly appreciated.

The PhD students in the lab were always available for any form of support I needed and I would like to thank them here. **Willian** - for being very kind and for all the help right from clarifying technical doubts to tolerating the extreme temperatures that I set in the Perfect Reactor lab. **Koen** - for clarifying all my doubts that I initially had when writing the particle tracking code. **Ankur** - for allowing me to use the microscope whenever I needed. **Sudarshan** - for readily sharing his ID card almost everyday. At least half of the results would not have been possible if not for late evening access with his card. **Mike's** calibration application was used in the present work. Thanks, Mike for coming out of the way and offering help during the most crucial time of the thesis.

I would like to thank **Dr.Christian** for the co-supervision. Although we had very few meetings, the insights gained in signal processing and particle tracking were very useful. This entire thesis is a result of my main supervisor **Dr.Wim-Paul's** truly contagious enthusiasm. Thanks for being such an ideal supervisor that a student like me would wish for. Thanks for being extremely approachable, friendly and critical of the results at the same time. There was a period when I was trying all possible things but had nothing in hand to meet you and discuss. The patience that you showed during that time and the full freedom that you gave me to work my way through is something that I am always indebted to. The high interest levels you showed for every new regime of motion that we observed and the wonderful words of motivation after every meeting bespeaks your passion and kindness. In fact, the impact of some meetings made me work even harder, pushing the limits further. Finally, if there is a big take away for me, it is your strong hold in mathematics and your analytical approach to reduce any complex phenomenon to the fundamental equations. I admire the same. Thanks for all the lengthy derivations you worked out in the meetings, I am not sure if anybody would sit with a Master student for such lengthy derivations. I truly enjoyed this collaboration to say the least.

I am lost for words to thank my **friends** (of 8th Horcrux group at van Hasseltlaan) who have made these two years very special and because of whom I never missed Indian food. All the late-night discussions over tea about various topics are definitely to be remembered and cherished. Finally, I would like to thank my **mentor** and my **family** for everything.

*Shravan Raaghav K R
Delft, November 2019.*

Abstract

Multi-phase flows are ubiquitous in nature and in everyday life surrounding us, impacting us in almost all possible ways. The presence of particles in a flow can change the flow behaviour in an unpredictable manner. The simplest example of a particle-laden flow, that one can think of, is the settling of a single sphere under gravity in a quiescent fluid. This seemingly simple problem has very high relevance in various practical applications ranging from sedimentation of particles for water treatment, process industries, transport of a dense suspension (slurry) through a pipe and even in land reclamation. The settling/ascension of a single sphere, even after having been subject to extensive study for more than a century, remains far from being understood completely.

The path and the wake of a falling/rising sphere in a quiescent fluid may be subject to various instabilities depending upon two dimensionless quantities which are sufficient to characterize the motion. One being the Galileo number (Ga), which is the ratio of the net gravity force to the viscous force and the second one being the mass density ratio ($\bar{\rho}$), which is the ratio of the density of the solid to the density of the fluid. Depending upon Ga and $\bar{\rho}$, the sphere can take up various regimes of motion such as vertical, oblique, zigzagging, helical to name a few. This is mainly due to wake instabilities that trigger such path instabilities. Based on Ga and $\bar{\rho}$, various regime maps have been proposed in literature. There have been several disagreements regarding the characterization of such paths taken by the sphere. This is due to the strong solid-fluid coupling and the inherent complexity due to triggering of the instabilities in such cases, which is far from being trivial to model numerically and also to test experimentally. The disagreements between different numerical works and different experimental works make the problem hard pressing and tempting to study. Moreover, the settling behaviour of a single sphere can also aid in understanding the collective effects displayed in the settling of dilute suspensions.

The goal of the present study is to shed light on the confusion/disagreements in literature until now and characterize various path instabilities. A detailed experimental investigation is conducted to cover the parameter space (regime map) by employment of over 250 different combinations of Ga and $\bar{\rho}$ to cover as many regimes of motions as possible within the given time framework. The motion of a sphere is tracked in time using high-speed cameras and corresponding path/regime of motion, higher-order statistics like velocity and physical characteristics such as the Strouhal number/drag coefficient has been computed. The results validate well for some simple regimes of motion for which results from the previous studies perfectly agree with each other. With the confidence obtained after the validation, the current work attempts to draw points of consensus and disagreements with these earlier works for other more controversial regimes. Some regimes, which had only been observed using numerical simulations, have been observed experimentally for the first time. Also, intriguing bi-stable regimes (coexistence of two regimes) have been observed. Moreover, attempt is also made to characterize the suppression of the high-frequency oscillations with increase in the sphere inertia. An update of the regime maps is proposed with the results obtained from the experiments conducted. The results obtained will also serve as an excellent tool for validation of new numerical models, using which the Ga - $\bar{\rho}$ parameter space can be covered in great detail. Recommendations for future work are given.

Nomenclature

A_{fs} - Planform area of sphere (m^2)

C_d - Drag coefficient (-)

c_i - Camera (index denotes camera number)

d_p - Sphere diameter (m)

F_L - Fluctuating lift force on the sphere (N)

f - Frequency (Hz)

f_g - Gravitational frequency scale (Hz)

\bar{f} - Dimensionless frequency (-)

g - Gravitational acceleration (m/s^2)

Ga - Galileo Number (-)

I - Pixel Intensity (-)

m_p - Mass of sphere (kg)

$M_{i,j}$ - Added mass tensor (kg)

p_i - plane (index denotes plane number)

Re - Reynolds Number (-)

St - Strouhal Number (-)

\bar{St} - Stokes Number (-)

t_p - Particle response time scale (s)

t_f - Flow response time scale (s)

t_g - Gravitational time scale (s)

\underline{u}_p - Sphere velocity vector (m/s)

v_i - Velocity of sphere (index corresponds to the direction -x,y and z) (m/s)

v_h - Horizontal sphere velocity (m/s)

v'_h - Horizontal sphere velocity fluctuation (m/s)

\bar{v}_y - Mean fall (y) velocity of the sphere (m/s)

V_p - Volume of sphere (m^3)

X - x coordinate in physical space (mm)

Y - y coordinate in physical space (mm)

Z - z coordinate in physical space (mm)

ρ_p - Sphere density (kg/m^3)

ρ_f - Fluid density (kg/m^3)

$\bar{\rho}$ - Density ratio (-)

ν_f - Kinematic viscosity (m^2/s)

Contents

| | |
|--|-------------|
| Acknowledgements | v |
| Abstract | vii |
| Nomenclature | ix |
| List of Figures | xiii |
| List of Tables | xvii |
| 1 Introduction | 1 |
| 1.1 Theory | 2 |
| 1.1.1 Morison's Heuristic Equation | 2 |
| 1.1.2 Relevant Scales of Motion and Related Dimensionless Quantities | 3 |
| 1.2 Review of Previous Literature | 4 |
| 1.3 Motivation | 11 |
| 1.4 Research Questions | 11 |
| 1.5 Research Goals and Approach to Studying the Regime Map | 11 |
| 1.5.1 Research Goals | 11 |
| 1.5.2 Approach to Studying the Regime Map | 11 |
| 1.6 Structure of the Report | 12 |
| 2 Experimental methodology | 13 |
| 2.1 Experimental Setup | 13 |
| 2.1.1 The Tank | 13 |
| 2.1.2 Precision Spheres | 14 |
| 2.1.3 Estimation of the Galileo number | 15 |
| 2.1.4 Releasing the Spheres | 16 |
| 2.1.4.1 Release Mechanism - Falling sphere | 16 |
| 2.1.4.2 Release Mechanism - Rising sphere | 17 |
| 2.1.5 High speed cameras and LED | 18 |
| 2.1.6 Camera calibration | 19 |
| 2.2 3D Particle Tracking Algorithm | 21 |
| 2.3 Post Processing | 23 |
| 2.3.1 Signal Filtering | 23 |
| 2.3.2 Correcting Spectral Leakage | 24 |
| 3 Results and Discussion | 26 |
| 3.1 Test for repeatability and effect of release mechanisms | 26 |
| 3.2 Establishment of regions of interest and jargon used | 26 |
| 3.3 Focus of the present work | 28 |
| 3.4 Falling Sphere | 29 |
| 3.4.1 Results low density cases ($\bar{\rho} \approx 1.12$) | 29 |
| 3.4.2 Results high density cases ($\bar{\rho} \approx 3.19$ and 3.9) | 38 |
| 3.4.3 Drag Curve - Falling sphere | 41 |
| 3.4.4 Suppression of high frequency oscillations with sphere inertia | 42 |

| | | |
|----------|---|-----------|
| 3.5 | Rising Sphere | 45 |
| 3.5.1 | Drag Curve - Rising sphere. | 52 |
| 4 | Summary and Conclusions | 53 |
| 4.1 | Summary | 53 |
| 4.2 | Conclusions. | 53 |
| 5 | Recommendations for future work | 56 |
| A | Literature Summary Table | 58 |
| B | Measurement of Sphere diameter | 60 |
| C | Water absorption by the spheres | 62 |
| D | Uncertainty Analysis | 63 |
| E | Density variation of Precision Spheres | 69 |
| F | Pseudo Arduino Program | 70 |
| G | Release Mechanism - Rising Case | 71 |
| H | Other Images | 72 |
| I | Experimental Procedure | 73 |
| J | Take-aways from doing experiments the wrong way (Experimental Intricacies) | 74 |
| | Bibliography | 76 |

List of Figures

| | | |
|------|--|----|
| 1.1 | a) Cyclone Separator, b) Fluidized Bed, c) Spray dryer (Images adapted from Crowe et al.[2]) | 1 |
| 1.2 | Force balance on a sphere falling with terminal settling velocity, all transient terms in Eq.1.3 is dropped. The orientation of axis is defined and g is the acceleration due to gravity. Here j corresponds to y direction | 3 |
| 1.3 | Regime map by Jenny et al.[3] representing various trajectories of ascending/falling free sphere (here \bar{f} is the dimensionless frequency - the dominant frequency of oscillation of sphere scaled with the gravitational frequency (f_g from Eq.1.6)). The symbols denote the simulations: +, steady oblique regime; , oblique and oscillating regime with low frequency ($0.045 \leq \bar{f} \leq 0.068$); \times , oblique and oscillating regime with high frequency ($\bar{f} \approx 0.180$); \circ , zigzagging periodic regime ($0.023 \leq \bar{f} \leq 0.035$); \square , three-dimensional chaotic regime. The domain of coexistence of a chaotic and a periodic state ($\bar{f} = 0.14$) is approximately delimited by the dotted line. | 5 |
| 1.4 | Wake patterns of settling of a single sphere ([4]) of $\bar{\rho} = 1.5$ and for $Ga = 155, 178, 190$ and 250, adapted from [5] | 5 |
| 1.5 | Sphere Trajectory for $\bar{\rho} = 0.5$ and $Ga = 170$ [3] | 6 |
| 1.6 | Critical values of Ga at the onset of the Hopf secondary bifurcation vs. $\bar{\rho}$ [3] | 6 |
| 1.7 | Regime map by Horowitz and Williamson [1] representing various trajectories of ascending/falling free sphere (here Re is the Reynolds number, the relation between Re and Ga is given in Eq.1.10) | 7 |
| 1.8 | 4R wake structure for zigzagging regime [1] | 7 |
| 1.9 | Regime map by Zhou and Dušek [6] representing various trajectories of ascending/falling free sphere (over lapping areas correspond to bi-stability), x and y axis are same as Fig.1.3 | 9 |
| 1.10 | Trajectory and vortical structure of the helical regime at $\bar{\rho} = 0.1$ and $Ga = 500$ [6] | 9 |
| 1.11 | Regime map by Auguste and Magnaudet [7] presenting various trajectories of freely ascending sphere with annotations SV - steady vertical, SO - steady oblique, PO - periodic oscillating, ZZ - zigzagging, ZZ ₂ - zigzag-2, IT - intermittent, ZO - oblique zigzagging, SP - spiralling, 3DC - chaotic | 10 |
| 2.1 | Experimental setup with the components annotated as, 1 & 2) Cameras, 3) Acquisition PC, 4) Components of the sphere release mechanism, 5 & 6) LEDs, 7) Water bath for pre-wetting the sphere before release, 8) Tank | 14 |
| 2.2 | Tank | 14 |
| 2.3 | PT 100 temperature sensor, 1) Multi-meter, 2) PT-100 probe | 14 |
| 2.4 | Tweezer | 16 |
| 2.5 | a) Schematic of vacuum suction release mechanism with annotations 1) Cross bar, 2) Tubing line, 3) Valve, 4) Drain chamber, 5) Vacuum pump, b) Cross bar with annotations 1) Tubing, 2) Cross bar, 3) Interface where sphere is held | 17 |
| 2.6 | Robotic gripper arm with annotations, 1) Arduino and 2) Servo Motor | 18 |
| 2.7 | Schematic of release mechanism for rising sphere with annotations 1) Spheres held under suction, 2) Tubing lines, 3) Valves, 4) Drain chambers, 5) Pressure relief valve and 6) Vacuum pumps | 18 |

| | | |
|------|--|----|
| 2.8 | a) Imager sCMOS camera and b) Imager pro HS camera | 19 |
| 2.9 | Schematic of camera and LED setup, with annotations 1&2) LEDs, 3&4)Cameras . . . | 19 |
| 2.10 | Calibration setup with annotations, 1&2) Calibration grid, 3&4) Mechanical traverse . | 20 |
| 2.11 | a) Grid with marker locations detected b) Back projected Image | 21 |
| 2.12 | Flow chart describing steps involved in the Particle tracking algorithm | 21 |
| 2.13 | a) Raw Image, b) Image after preprocessing, c) Centre position estimated | 22 |
| 2.14 | Estimation of 3D coordinate from the 2D coordinates from four different planes . . . | 23 |
| 2.15 | Variation of standard deviation of x-velocity with frame length employed. Red arrow depicts the chosen filter length | 23 |
| 2.16 | Plot of the velocity signal and line regressed through the signal to correct for drift . . . | 25 |
| 2.17 | Plot of velocity signal corrected for drift and plot of velocity signal after applying the Hanning window | 25 |
| 3.1 | Regime map by Zhou and Dušek [6] representing various trajectories of ascending/falling free sphere and horizontal red lines represent the region investigated in the present study, x and y axis are same as Fig.1.3 | 27 |
| 3.2 | Regime map by Auguste and Magnaudet [7] presenting various trajectories of freely ascending sphere (here Ar stands for the Archimedes number, which by definition of AM is same Ga),and horizontal red line represents the region investigated in the present study. The annotations are as follows: SV - steady vertical, SO - steady oblique, PO - periodic oscillating, ZZ - zigzagging, ZZ ₂ - zigzag-2, IT - intermittent, ZO - oblique zigzagging, SP - spiralling, 3DC - chaotic | 28 |
| 3.3 | Drifting Steady vertical trajectory for $\bar{\rho} = 1.156$ and $Ga = 110.14$ falling with a mean vertical velocity of 0.056 m/s | 29 |
| 3.4 | a) Steady oblique trajectory for $\bar{\rho} = 1.121$ and $Ga = 166.56$ falling at an angle of 6.27° with respect to the vertical with a mean vertical velocity of 0.0869 m/s and mean horizontal velocity of 0.0096 m/s, b) Steady oblique curved trajectory for $\bar{\rho} = 1.128$ and $Ga = 169.57$ falling at an angle of 5.23° with respect to the vertical with a mean vertical velocity of 0.0837 m/s and mean horizontal velocity of 0.0081 m/s. | 30 |
| 3.5 | a) Oblique Oscillating trajectory for $\bar{\rho} = 1.121$ and $Ga = 184.4$ falling at an angle of 4.57° with respect to the vertical with a mean vertical velocity of 0.086 m/s and mean horizontal velocity of 0.0072 m/s, b) Temporal variation of vertical velocity (amplitude of oscillation $\approx 0.015v_g$), c) Temporal variation of horizontal velocity (amplitude of oscillation $\approx 0.075v_g$), d) Spectrum of the fluctuation of horizontal velocity (with the red dot indicating the dominant peak at 0.059) | 31 |
| 3.6 | a) Oblique Oscillating trajectory for $\bar{\rho} = 1.121$ and $Ga = 283.81$, b) Temporal variation of horizontal velocity, c) Spectrum of the fluctuation of horizontal velocity (with the red dot indicating the dominant peak at 0.161) | 33 |
| 3.7 | a) High frequency Oscillating trajectory for $\bar{\rho} = 1.13$ and $Ga = 259.92$, b) Temporal variation of z-velocity, c) Spectrum of the fluctuation of z-velocity (with the red dot indicating the dominant peak at 0.154) | 34 |
| 3.8 | a) Transition from a chaotic drifting trajectory to high frequency oscillating trajectory for $\bar{\rho} = 1.11$ and $Ga = 278.95$ b) Irregular high frequency oscillating trajectory for $\bar{\rho} = 1.11$ and $Ga = 277.49$ | 35 |
| 3.9 | 3D velocity plot for all the regimes along line FL1, with reach regime corresponding to a Ga and $\bar{\rho}$ as follows: Steady Vertical - $Ga = 110.14$ and $\bar{\rho} = 1.156$, Steady Oblique - $Ga = 166.56$ and $\bar{\rho} = 1.121$, Oblique Oscillating - $Ga = 184.4$ and $\bar{\rho} = 1.121$, High frequency oscillating - $Ga = 259.92$ and $\bar{\rho} = 1.13$, Chaotic - $Ga = 283.81$ and $\bar{\rho} = 1.121$ | 36 |

| | | |
|------|--|----|
| 3.10 | $Ga - \bar{\rho}$ map updated along line FL with the results of the present study. The map represents a direct comparison with map of ZD. Vertical lines represent the thresholds of different regimes from the ZD map, with annotations, SV-steady vertical, SO-steady oblique, LO-low-frequency oblique oscillating, VO-vertical oscillating | 36 |
| 3.11 | a) Helical/rotating trajectory for $\bar{\rho} = 3.19$ and $Ga = 208.4$ with half pitch and diameter of the helix is $\approx 214d_p$ and $12d_p$ respectively, b) Temporal variation of horizontal velocity, c) Spectrum of the fluctuation of horizontal velocity (dominant peaks indicated by red dots) | 38 |
| 3.12 | a) Helical/rotating trajectory with lower pitch for $\bar{\rho} = 3.88$ and $Ga = 225.58$, b) Helical/rotating trajectory with lower pitch and pronounced oscillations for $\bar{\rho} = 3.21$ and $Ga = 225.67$, c) Irregular Helical/rotating trajectory $\bar{\rho} = 3.21$ and $Ga = 231.17$, d) Irregular Helical/rotating trajectory $\bar{\rho} = 3.19$ and $Ga = 230.016$ | 40 |
| 3.13 | $Ga - \bar{\rho}$ map updated along line FH1 and FH2 with the results of the present study. The map represents a direct comparison with map of ZD. Vertical lines represent the thresholds of different regimes from the ZD map, with annotations, SO-steady oblique, HO-high-frequency oblique oscillating, P/R-Planar or rotating bistable | 41 |
| 3.14 | C_d plotted for various Re for falling cases (the fixed sphere curve is obtained from the relation proposed by Abraham (Eq1.11)[8]) | 41 |
| 3.15 | Spectrum of fluctuation of horizontal velocity for different density ratios in Table 3.4 ($\bar{\rho}$ increases in the direction of the arrow) | 44 |
| 3.16 | Trajectory of Steady oblique regime for $\bar{\rho} = 0.892$ and $Ga = 159.36$ falling at an angle of 3.47° with a mean vertical and horizontal velocity of 0.0775 and 0.004 m/s respectively | 45 |
| 3.17 | a) Oblique Oscillating trajectory for $\bar{\rho} = 0.867$ and $Ga = 179.54$ falling at an angle of 4.32° with respect to the vertical with a mean vertical velocity of 0.089 m/s and mean horizontal velocity of 0.0065 m/s, b) Temporal variation of vertical velocity (amplitude of oscillation $\approx 0.011v_g$), c) Temporal variation of horizontal velocity (amplitude of oscillation $\approx 0.05v_g$), d) Spectrum of the fluctuation of horizontal velocity (with the red dot indicating the dominant peak at 0.063) | 46 |
| 3.18 | a) Zigzagging trajectory for $\bar{\rho} = 0.874$ and $Ga = 265.7$, b) Temporal variation of z-velocity, c) Spectrum of the fluctuation of z-velocity (with the red dot indicating the dominant peak at 0.043) | 47 |
| 3.19 | a) Trajectory of improper zigzagging for $\bar{\rho} = 0.864$ and $Ga = 202.42$ b) Trajectory of improper zigzagging for $\bar{\rho} = 0.882$ and $Ga = 198.98$ | 48 |
| 3.20 | a) High frequency Oscillating trajectory for $\bar{\rho} = 0.879$ and $Ga = 279.11$, b) Temporal variation of z-velocity, c) Spectrum of the fluctuation of z-velocity (with the red dot indicating the dominant peak at 0.154) | 49 |
| 3.21 | a) Trajectory of bi-stable regime regime for $\bar{\rho} = 0.872$ and $Ga = 307.32$ b) Trajectory of bi-stable regime for $\bar{\rho} = 0.883$ and $Ga = 255.16$ | 50 |
| 3.22 | 3D velocity plot for all the regimes along line R, with reach regime corresponding to a Ga and $\bar{\rho}$ as follows: Steady Vertical - $Ga = 98.53$ and $\bar{\rho} = 0.878$, Steady Oblique - $Ga = 159.36$ and $\bar{\rho} = 0.892$, Oblique Oscillating - $Ga = 179.54$ and $\bar{\rho} = 0.867$, Zigzag - $Ga = 265.7$ and $\bar{\rho} = 0.874$, High frequency oscillating - $Ga = 279.1$ and $\bar{\rho} = 0.879$, Chaotic - $Ga = 307.32$ and $\bar{\rho} = 0.872$ | 50 |
| 3.23 | $Ga - \bar{\rho}$ map updated along line R with the results of the present study. The map represents a direct comparison with map of ZD and AM. Violet and black vertical lines represent the thresholds of different regimes from the ZD and AM map respectively, with annotations, SV-Steady vertical, SO-steady oblique, LO - low-frequency oblique oscillating, PO - periodic oscillating (same as LO but named differently by AM) and VO-vertical oscillating | 51 |

| | |
|--|----|
| 3.24 C_d plotted for various Re for rising cases (the fixed sphere curve is obtained from the relation proposed by Abraham (Eq1.11)[8]) | 51 |
| B.1 a) Microscope b) Grid used for calibration (distance between two points is $500 \mu m$) . . | 60 |
| B.2 Nylon Sphere of diameter 3.5 mm viewed under microscope and circle fit (blue line) . | 61 |
| C.1 a) Nylon sphere, b) Polypropylene sphere | 62 |
| C.2 a) Silicon Nitride sphere, b) Aluminium Oxide sphere | 62 |
| D.1 a) Plot of kinematic viscosity with temperature (red dashed line is the linear fit), b) Plot of density with temperature (red dashed line is the linear fit) | 65 |
| D.2 $Ga - \bar{\rho}$ map updated along line FL with the results of the present study including uncertainties | 66 |
| D.3 $Ga - \bar{\rho}$ map updated along line FH1 and FH2 with the results of the present study including uncertainties | 66 |
| D.4 $Ga - \bar{\rho}$ map updated along line R with the results of the present study including uncertainties | 67 |
| D.5 C_d plotted for various Re for falling cases including uncertainties (the fixed sphere curve is obtained from the relation proposed by Abraham (Eq1.11)[8]) | 67 |
| D.6 C_d plotted for various Re for rising cases including uncertainties (the fixed sphere curve is obtained from the relation proposed by Abraham (Eq1.11)[8]) | 68 |
| E.1 a) Nylon spheres (total number - 87, density specified by supplier = 1120 kg/m^3). Mean density = 1123.7 kg/m^3 , standard deviation = 9.98 kg/m^3 b) Polypropylene spheres (total number - 90, density specified by supplier = 870 kg/m^3 . Mean density = 878.02 kg/m^3 , standard deviation = 10.65 kg/m^3 | 69 |
| E.2 a) Silicon Nitride spheres (total number - 28, density specified by supplier = 3190 kg/m^3). Mean density = 3194.4 kg/m^3 , standard deviation = 26.04 kg/m^3 , b) Aluminium Oxide spheres (total number - 15, density specified by supplier = 3900 kg/m^3). Mean density = 3949.4 kg/m^3 , standard deviation = 54.9 kg/m^3 | 69 |
| G.1 Release mechanism setup -releasing a sphere from the bottom of a tank | 71 |
| H.1 Weighing Scale | 72 |
| H.2 Individual spheres stored in separate Eppendorf tubes | 72 |

List of Tables

| | | |
|-----|--|----|
| 1.1 | Various types of Zigzagging reported by ZD [6] | 8 |
| 2.1 | Sphere specifications | 15 |
| 2.2 | Frame length employed in Savitzky Golay Filter | 24 |
| 3.1 | Results of different release for a sphere with $Ga = 178$ and $\bar{\rho} = 1.12$ | 26 |
| 3.2 | Abbreviations for relevant literature | 26 |
| 3.3 | Angle with respect to vertical for oblique regime (for steady oblique and oblique oscillating) | 31 |
| 3.4 | Various $\bar{\rho}$ chosen for testing suppression of high frequency oscillations | 44 |
| 3.5 | St for Zigzag regime and comparison with previous works | 48 |

Introduction

Studying the transport phenomena in sedimentation and ascension of spheres in a quiescent fluid plays a crucial role in understanding the theory and physics behind dispersed multiphase flows. Having ubiquitous influence in many natural processes like geophysical/atmospheric flows and settling of micro-organisms (planktons), the understanding of the same is crucial and can never be neglected. It has a direct impact on many widespread industrial applications including spray drying, cyclone separators, fluidized bed reactors, paper manufacturing and also in water treatment plants [9][10][2]. Some figures are depicted below.

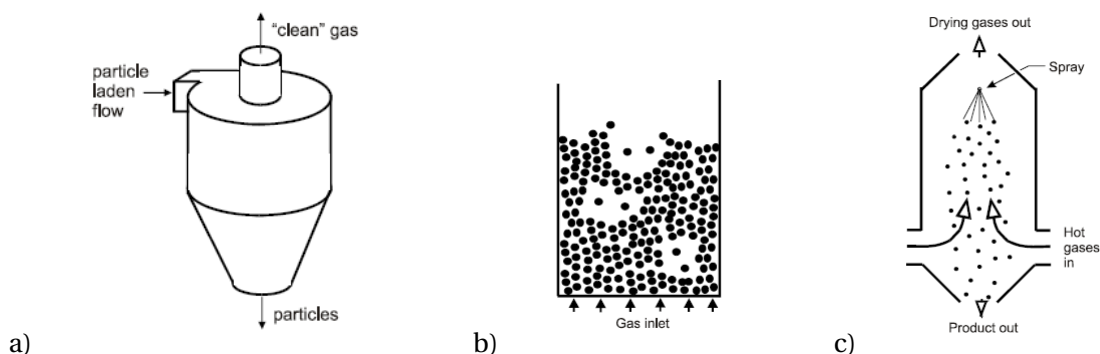


Figure 1.1: a) Cyclone Separator, b) Fluidized Bed, c) Spray dryer (Images adapted from Crowe et al.[2])

Although sedimentation of a suspension can be considered as the simplest example of a suspension flow, the settling process is extremely complex with non-linear hydrodynamic interactions and collisions [11]. Although the research conducted in this field spans more than half a century, the present understanding is far from complete and a lot of work still has to be done. These were the important conclusions of the reviews by Guazzelli [11] and Ern et. al.[12]. Only recently, with the increase of the computational capabilities, Jenny et al.[3] were the first to investigate a wide range of physical parameter space for the settling/ascension of a single sphere. Surprisingly, great richness in physics, with path and wake instabilities were observed for a very simple scenario of a single sphere settling/rising in a still fluid. The entire dynamics of the path instabilities can be summed up by characterizing them using two dimensionless quantities (density ratio and Galileo number), given by the expressions,

$$\bar{\rho} = \frac{\rho_p}{\rho_f} \quad (1.1)$$

$$Ga = \sqrt{\frac{|\bar{\rho} - 1| g d_p^3}{\nu_f^2}} \quad (1.2)$$

where ρ_p and ρ_f are the sphere and fluid densities respectively, g corresponds to the gravitational acceleration, d_p is the sphere diameter, ν_f is the kinematic viscosity of the fluid.

For a single sphere settling/rising in a still fluid, despite many works done in the past, there are several disagreements between various works in the regimes of motion, thresholds of instabilities predicted and even in drag coefficients. A numerical approach towards exploring various regimes of motion may seem best suited as it allows to cover the entire parameter space in a detailed and a systematic manner. But, owing to the complex particle fluid interactions and the accuracy of the numerical method used, including mesh resolution and domain size, different numerical works ([7][3][4][6]) disagree with each other. Even different experimental works([1], [13], [14]) disagree with each other, owing to the high sensitivity of the particle/wake structure to Ga and $\bar{\rho}$ and the uncertainty in determining these numbers accurately and also to the residual disturbances present in the fluid. Even slight inhomogeneities like air voids in the sphere or improper methodology of releasing the sphere can destroy the regime of motion the sphere was to take otherwise.

1.1. Theory

1.1.1. Morison's Heuristic Equation

The simple force balance on a falling/rising particle under gravity in a quiescent fluid can be approximated by the heuristic summation of the forces that act on the particle proposed by Morison by the following equation (adapted from Brennen[15]):

$$\rho_p V_p \frac{du_{p,i}}{dt} \approx (\rho_p - \rho_f) V_p g_i - \left(M_{ij} \frac{du_{p,j}}{dt} \right) - \left(\frac{1}{2} C_{ij} A_{fs} \rho_f |u_p| u_{p,j} \right) \quad (1.3)$$

where, u_p is the particle velocity (we shall denote it in 3-directions as v_x, v_y and v_z), ρ_p and ρ_f is the particle and fluid density respectively, V_p is the volume of the particle, M_{ij} is the added mass tensor (which for the simple case of a sphere will reduce to $\frac{1}{2}\rho_f V_p$), A_{fs} is the planform area and C_{ij} being the lift/drag coefficient tensor.

The coefficients, M_{ij} and C_{ij} , are not only functions of Re but also functions of the reduced time or frequency scales of the unsteady motion. The effect of Basset History force can be neglected for the Stokes regime, as the effect from the added mass term will dominate for short times directly after the release of the sphere, while at large times, it can be neglected with respect to the steady drag force. Moreover the motion of the particle will usually involve oscillations or acceleration from rest and the effect of history forces is neglected here. This expression(Eq.1.3) will aid in gaining an overall understanding of the force balance involved. This expression will also be used later in chapter 3, where a simple hypothesis is presented and verified experimentally. A simple schematic of the force balance of a sphere settling with terminal velocity is depicted in Fig.1.2.

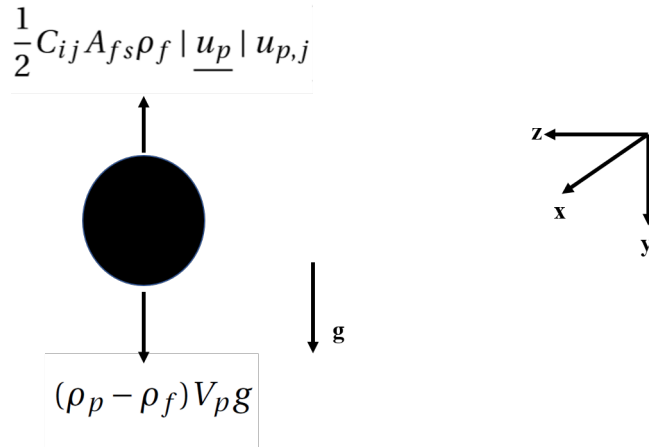


Figure 1.2: Force balance on a sphere falling with terminal settling velocity, all transient terms in Eq.1.3 is dropped. The orientation of axis is defined and g is the acceleration due to gravity. Here j corresponds to y direction

1.1.2. Relevant Scales of Motion and Related Dimensionless Quantities

Already, the two important dimensionless quantities, namely the Ga and $\bar{\rho}$ has been established in equations 1.1 and 1.2. Other scales are important to be defined as they will later be used for non-dimensionalizing the quantities in the plots/results. Other relevant scales include the inertial velocity scale (Eq.1.4) and the inertial/gravitational time scale (Eq.1.5).

$$v_g = \sqrt{|\bar{\rho} - 1| g d_p} \quad (1.4)$$

$$t_g = \sqrt{\frac{d_p}{|\bar{\rho} - 1| g}} \quad (1.5)$$

The gravitational frequency scale can be defined from the time scale as

$$f_g = \frac{1}{t_g} = \sqrt{\frac{|\bar{\rho} - 1| g}{d_p}} \quad (1.6)$$

The dimensionless frequency (\bar{f}), is then given by the following expression,

$$\bar{f} = \frac{f}{f_g} \quad (1.7)$$

where f is the frequency obtained from the spectrum of the horizontal velocity of falling/rising sphere. In the case where f is the dominant frequency in the spectrum, $\bar{f} = St$, where St is the Strouhal number.

It is important to establish the relation for the drag coefficient of the sphere, which will later be used in chapter 3, where the results of drag coefficients for various cases will be reported. Here, we will make some assumptions. First being that the sphere has reached terminal settling velocity before it

reaches the field of view of our experimental setup. This means that all the transient terms in Eq.1.3 can be dropped (depicted in Fig.1.2). The second one being that the mean vertical velocity is much larger than the horizontal velocities, hence, $|u_p| = \sqrt{v_x^2 + v_y^2 + v_z^2} \approx v_y$. Now, on equating the forces, we have,

$$(\rho_p - \rho_f)V_p g \approx \frac{1}{2}\rho_f C_d A_{fs} v_y^2 \quad (1.8)$$

Substituting expressions for v_p and A_{fs} and diving LHS and RHS by v_f^2

$$\frac{1}{v_f^2}(\rho_p - \rho_f)g \frac{4}{3}\pi \left(\frac{d_p}{2}\right)^3 \approx \frac{1}{v_f^2} \frac{1}{2}\rho_f C_d \pi \frac{d_p^2}{4} v_y^2$$

Upon further simplification, we are left with,

$$\frac{1}{v_f^2}(\bar{\rho} - 1)g \frac{4}{3}d_p^3 \approx \frac{1}{v_f^2}d_p^2 v_y^2 C_d \implies \frac{4}{3}Ga^2 \approx Re^2 C_d$$

Hence, we obtain an expression for C_d as,

$$C_d \approx \frac{4}{3} \frac{Ga^2}{Re^2} \quad (1.9)$$

On rewriting, Eq.1.9, we can relate Re and Ga ,

$$Re \approx \sqrt{\frac{4}{3} \frac{1}{C_d} Ga} \quad (1.10)$$

1.2. Review of Previous Literature

Investigation of flow regimes and wake dynamics of a fixed sphere has been dealt for a long time using experiments as well as DNS ([16–20]). Different flow regimes based on Reynolds number have been identified. The Reynolds number thresholds for wake bifurcations have been dealt in detail and even recently studied for a fixed sphere by Fabre et al.[21] and the understanding is quite clear. The various thresholds for wake bifurcations are concisely explained in the review by Ern et al. [12].

The scenario of a freely moving sphere, has received less attention when compared to the fixed sphere counterpart. The fact that there is no constraint on the sphere motion, leads to different path and wake instabilities resulting in a variety of path characteristics similar to bubbles. This has intrigued researchers over time. The additional degree of freedom in the freely moving sphere clearly distinguishes it from the classical behaviour of a fixed sphere. Some of the very earlier works include that of Preukschat [22], who observed the vibrating and rectilinear regime in rising and falling spheres. Later Karamanev et al. ([23, 24]) observed spiralling motion of rising spheres and made measurements of the drag coefficient which are discussed later in this chapter. The first extensive study on the dynamics of rising and falling spheres and their associated instabilities were by Jenny et al. [3] (hereafter denoted as JDB) using high accuracy spectral-element simulations. The study neatly fits the entire dynamics of a single sphere into a map (Fig. 1.3) based on Ga (Eq.1.2) and

$\bar{\rho}$ (Eq.1.1). Regimes such as the steady vertical, steady oblique, periodic oblique, zigzagging and chaotic regime were observed for the first time. Moreover a bi-stable region where a vertically periodic regime and chaotic regime coexisted were also observed. They report the results for Ga up to 350. The work of JDB was repeated for different regimes by Uhlmann and Dusek [4], but by employing an immersed boundary method for the simulations. The wakes of various regimes are shown in Fig.1.4. It is important to establish the results of JDB in detail since all the other studies that follow will be using JDB work as the reference for comparison and even as motivation for their work.

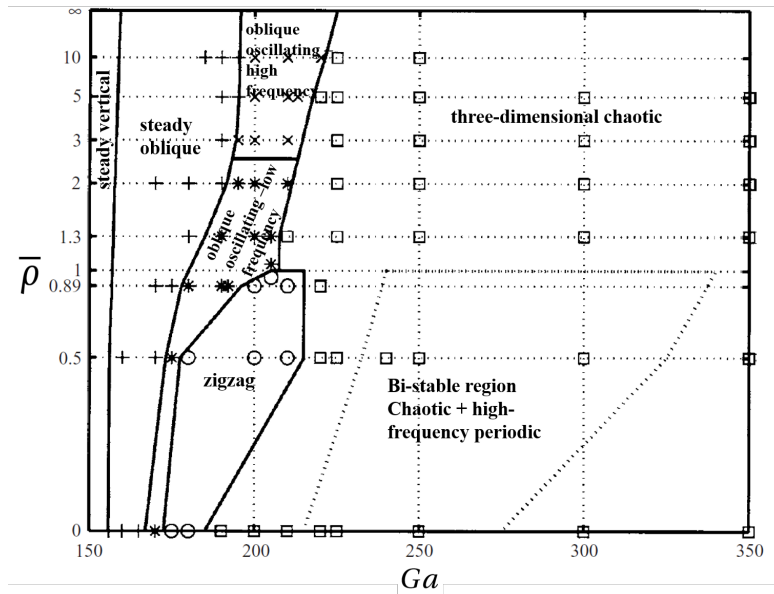


Figure 1.3: Regime map by Jenny et al.[3] representing various trajectories of ascending/falling free sphere (here \bar{f} is the dimensionless frequency - the dominant frequency of oscillation of sphere scaled with the gravitational frequency (f_g from Eq.1.6)). The symbols denote the simulations: +, steady oblique regime; *, oblique and oscillating regime with low frequency ($0.045 \leq \bar{f} \leq 0.068$); x, oblique and oscillating regime with high frequency ($\bar{f} \approx 0.180$); o, zigzagging periodic regime ($0.023 \leq \bar{f} \leq 0.035$); \square , three-dimensional chaotic regime. The domain of coexistence of a chaotic and a periodic state ($\bar{f} = 0.14$) is approximately delimited by the dotted line.

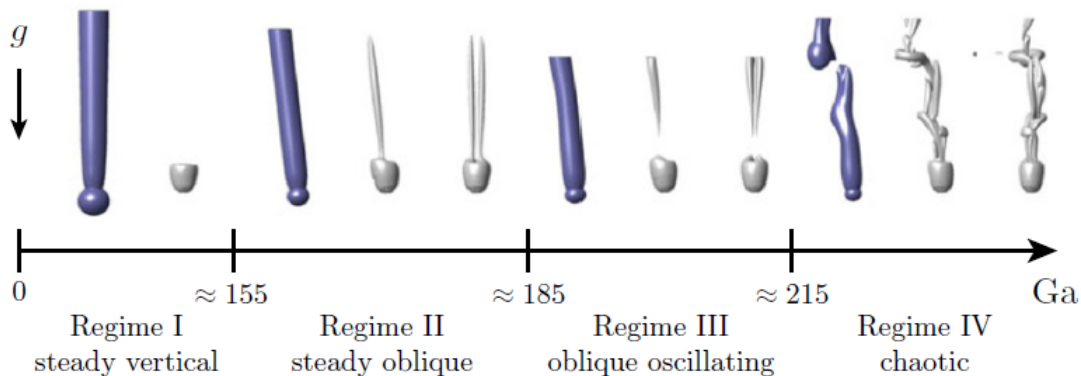


Figure 1.4: Wake patterns of settling of a single sphere ([4]) of $\bar{\rho} = 1.5$ and for $Ga = 155, 178, 190$ and 250 , adapted from [5]

Some important observations made by JDB are presented below. The sphere which initially rises in a steady vertical manner for low Ga exhibited different regimes as Ga was increased due to vari-

ous bifurcations which trigger instabilities. The steady vertical regime which was observed to have an axisymmetric wake similar to the fixed sphere, undergoes a primary bifurcation and becomes a planar symmetric wake leading to a steady oblique motion (Fig. 1.5). This bifurcation is expected around a Ga of 155 for infinitely light spheres ($\bar{\rho} = 0$) whereas Ga being 160 for the case where the $\bar{\rho}$ was infinite (similar to a fixed sphere) implying that the critical Ga for the primary bifurcation is almost independent of $\bar{\rho}$. This planar wake later undergoes a secondary (Hopf-type) bifurcation leading to an oblique oscillating regime with periodic oscillations. The critical Ga for this bifurcation was observed to be function of $\bar{\rho}$ (Fig. 1.6).

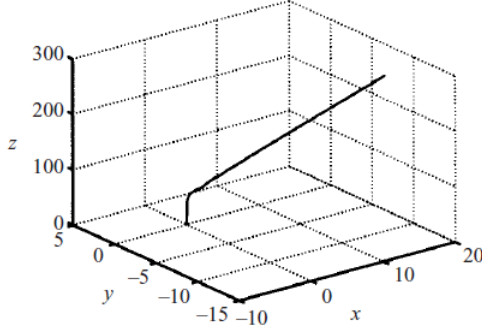


Figure 1.5: Sphere Trajectory for $\bar{\rho} = 0.5$ and $Ga = 170$ [3]

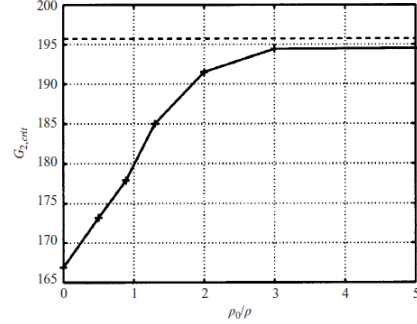


Figure 1.6: Critical values of Ga at the onset of the Hopf secondary bifurcation vs. $\bar{\rho}$ [3]

Moreover for $\bar{\rho} < 2.5$, low-frequency oscillations were observed, whereas for $\bar{\rho} > 2.5$, high frequency oscillations were observed. Finally, on increasing the Ga further, they report a tertiary bifurcation, which corresponds to the onset of chaos. For light spheres ($\bar{\rho} < 1$) a zigzagging regime was also observed and it undergoes a sub-harmonic transition (asymptotic states) with a period doubling and even period tripling. At even higher Ga , as mentioned earlier a vertically periodic regime was found to coexist with the chaotic regime. The Ga and $\bar{\rho}$ corresponding to all the above regimes can be found in the appendix A.

A series of experimental works followed the work of JDB. The work of Veldhuis et al. [13, 25] ([13] will hereafter denoted as VB) primarily focused on verifying the interesting results obtained by JDB. Particle trajectory was obtained from high-speed cameras and flow field was visualized using Schlieren optics technique. Five different test cases were chosen, namely one from each regime obtained by JDB. The vertical, oblique and the oblique oscillating regime agreed quite well with the results of JDB. Although they were not able to observe a perfect zigzagging, an occasional zigzagging was observed which was attributed to possible sphericity and inhomogeneity in mass distribution in the spheres. Another work by the same group also studied the drag characteristics of light sphere [14] (hereafter denoted as VBL) which will be discussed briefly later in this chapter.

The major experimental work in this field was by Horowitz and Williamson [1] (here after denoted as HW). Effect of Re is studied in detail ($100 < Re < 15000$) or ($90 \lesssim Ga \lesssim 10,000$) and a regime map (Fig. 1.7) was created similar to JDB. The majority of the results were in contrast with the results of the above mentioned works. Zigzagging was not observed for all spheres with $\bar{\rho} < 1$, rather new limits for zigzagging were proposed (shown below).

- $450 < Re < 1550$, critical $\bar{\rho}$ below which zigzag occurs is 0.36.

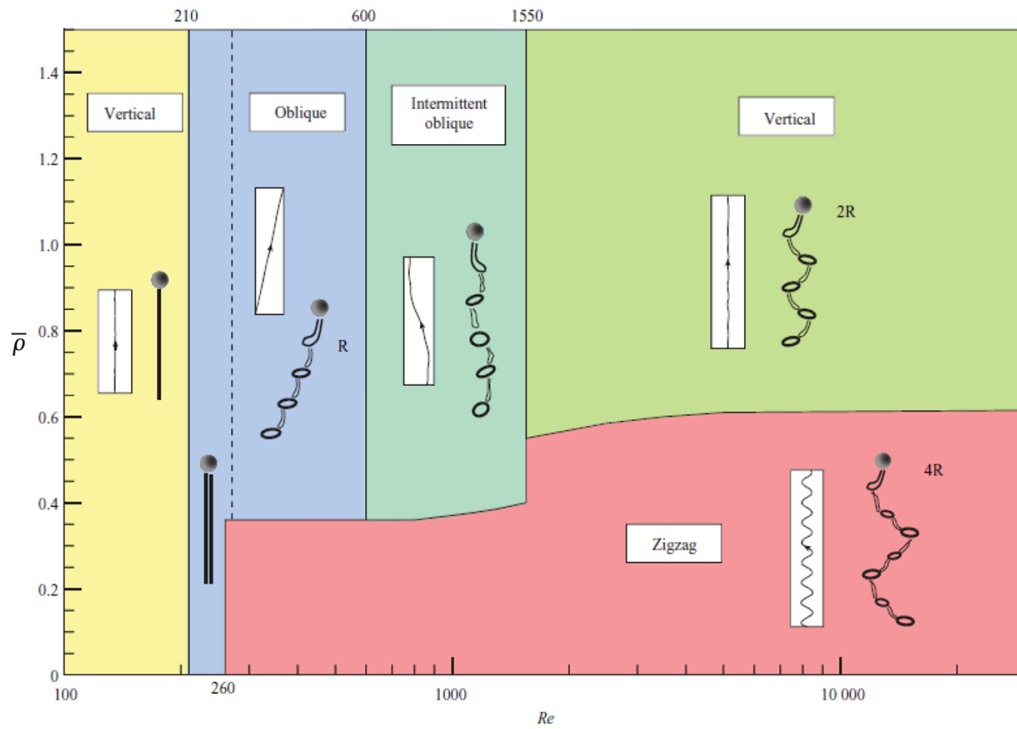


Figure 1.7: Regime map by Horowitz and Williamson [1] representing various trajectories of ascending/falling free sphere (here Re is the Reynolds number, the relation between Re and Ga is given in Eq.1.10)

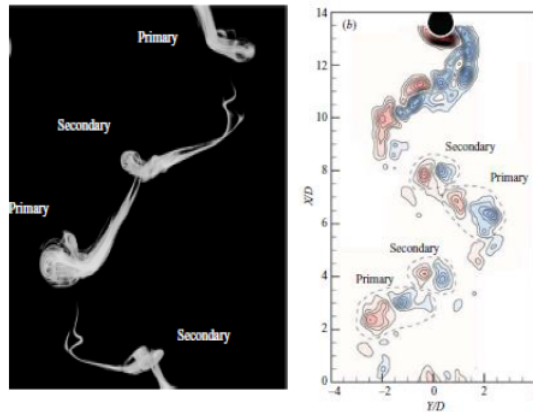


Figure 1.8: 4R wake structure for zigzagging regime [1]

- $Re > 1550$, critical $\bar{\rho}$ below which zigzag occurs is 0.6.

Also, an interesting 4R wake structure, where four time shedding (including primary and secondary vortices) in one period of oscillation (Fig. 1.8) was observed for the zigzagging mode from dye visualizations. The existence of the 4R wake structure was later numerically substantiated by Auguste and Magnaudet [7]. At higher Re vortex shedding was observed with a 2R wake structure. Also, no chaotic regime was observed even for excessively large Ga of 10000. They only observed irregular motion if the fluid was subject to initial disturbances/noise. Also, a new 'intermediate oblique' regime was identified where the path switches between an oblique and a rectilinear path and no

periodicity was detected. Moreover, no regions for the chaotic domain were proposed. Rather, the falling spheres exhibited a rectilinear/vertical path even for large values of Ga . Different wake structures were associated with each regime (depicted in the Fig. 1.7).

Due to much disagreement with the experiments of HW and numerical work of JDB, the same research group of JDB very recently performed numerical simulations and presented new results (Zhou and Dušek [6], here after denoted as ZD). They performed simulations for a larger Ga range and by allowing the sphere to travel for sufficiently long distances to check the veracity of the earlier published results by JDB. Although some results did agree with their earlier work, ZD pointed out some corrections to the map that was proposed by JDB and updated the map (Fig.1.9). The differences in the two maps can be seen by comparing Fig.1.3 and Fig.1.9. Some new and different types of motion were identified in the regime which was earlier characterized as zigzagging, the different types of zigzagging are shown in Table 2.1. But these special cases were not reported for a cloud of data but only for particular values of $\bar{\rho}$ and Ga .

Table 1.1: Various types of Zigzagging reported by ZD [6]

| $\bar{\rho}$ | Ga | Type of zig-zagging |
|--------------|-----------|---------------------------------|
| 0 | 176 | Planar imperfect zigzagging |
| (0,0.2) | (210,230) | Fast ZZ oblique |
| 0.2 | 190 | Non-planar imperfect zigzagging |
| 0.2 | 200 | Planar periodic zigzagging |
| 0.5 | 180 | Perfect planar zigzagging |
| 0.5 | 190 | Periodic oblique zigzagging |
| 0.65 | 195 | Oblique imperfect zigzagging |

The bi-stable region reported by JDB was tested for longer distances and it was found to become chaotic. Hence, the limits for bi-stability was reduced and new limits characterizing the vertically periodic regime were reported (Fig. 1.9). Also at high $\bar{\rho}$ and a narrow range of Ga a 'nearly helical' path was observed (also observed by JDB and VB). This regime was characterized in a detailed manner in this work and was found to be bi-stable with chaotic motion. For very large Ga ($\gtrsim 375$) and infinitely light spheres ($\bar{\rho} = 0$), perfect helical trajectories (Fig. 1.10) were reported (similar to the one reported by Karamanev et al. [24] and VBL [14]). A new, corrected version of JDB's map was presented with the new results (depicted in Fig. 1.9). It is important to note that, although revised, the new results of ZD did not match well with the experimental work of HW.

The final and most recent work by Auguste and Magnaudet [7] (here after denoted as AM) systematically explored the parameter space for light spheres for Ga up to 700. The major motivation of this work was that there was much discrepancy among the earlier results and only a single code had been employed for this study up till now. Many new regimes were reported in the intermediate Ga range of 200 to 300. Also the helical regime observed by ZD was also observed and a full domain of existence of this regime was reported. As mentioned earlier the 4R wake structure confirmed the experimentally observed one by HW. All the thresholds of the regimes have been discussed in appendix A. Similar to the earlier works a map of Ga and $\bar{\rho}$ was created (depicted in Fig. 1.11) The trajectories and the properties of such new regimes are explained below.

- Intermittent regime (IT) - the sphere hesitates to perform periodic planar zigzag – onset of

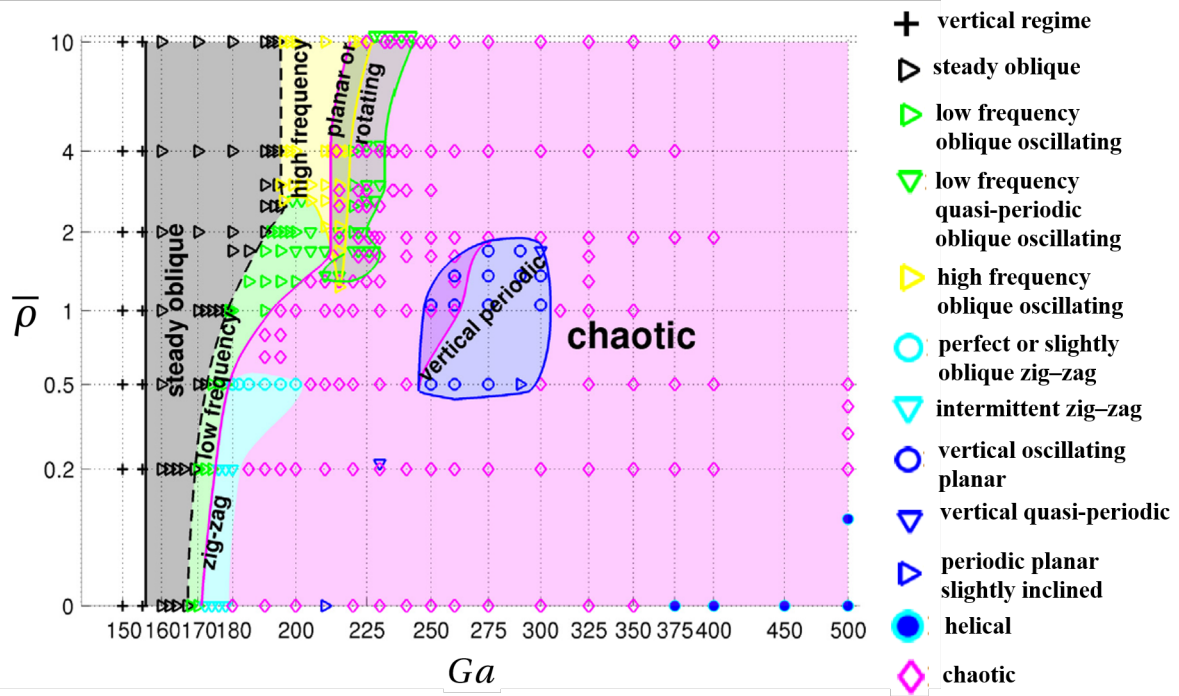


Figure 1.9: Regime map by Zhou and Dušek [6] representing various trajectories of ascending/falling free sphere (overlapping areas correspond to bi-stability), x and y axis are same as Fig.1.3

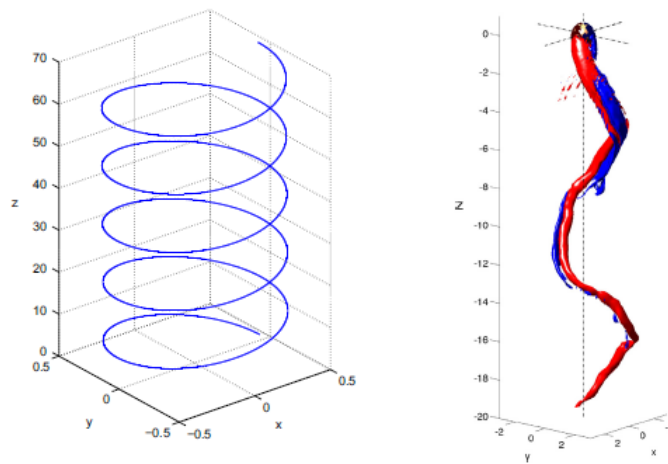


Figure 1.10: Trajectory and vortical structure of the helical regime at $\bar{\rho} = 0.1$ and $Ga = 500$ [6]

chaos can be inferred. The amplitude of the zigzag is in the order of sphere diameter (d_p). The intermittency sets in at a higher Ga for increasing $\bar{\rho}$.

- The oblique zigzag (ZO) - sphere follows a periodic planar path with non-zero mean drift and combines the characteristics of oblique periodic oscillating regime and regular zigzagging regime.
- The low amplitude/high-frequency zigzag (ZZ_2), emerges only after a long travel, the sphere consistently drifts while ascending and the path is non-planar. Amplitude is one order of magnitude smaller than the regular zigzagging regime.
- The spiral or helical (SP) regime - observed for very larger Ga , and very light spheres. The

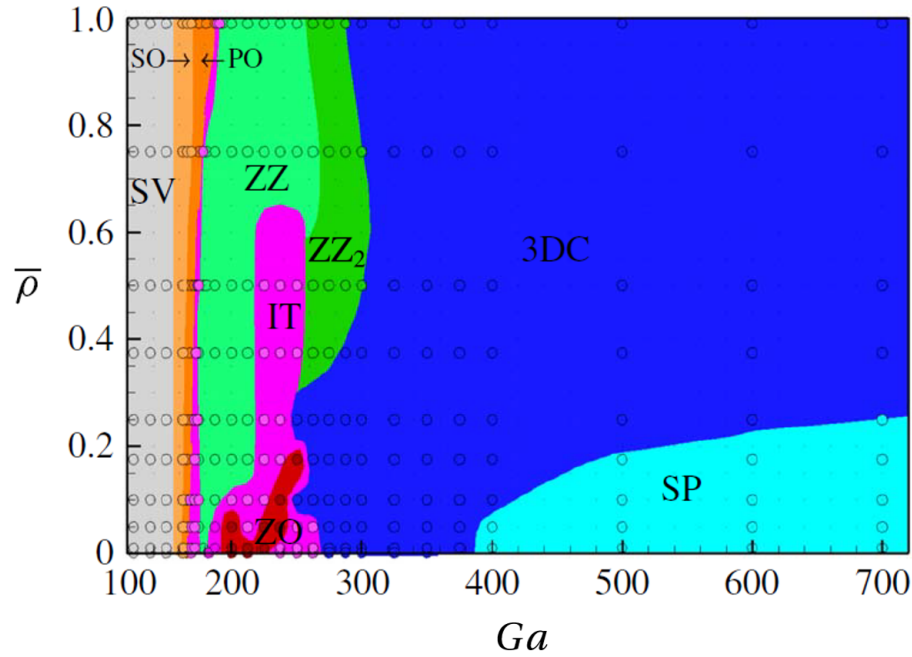


Figure 1.11: Regime map by Auguste and Magnaudet [7] presenting various trajectories of freely ascending sphere with annotations SV - steady vertical, SO - steady oblique, PO - periodic oscillating, ZZ - zigzagging, ZZ₂ - zigzag-2, IT - intermittent, ZO - oblique zigzagging, SP - spiralling, 3DC - chaotic

pitch of the spiral decreases as Ga increases. But there is not much variation in the diameter of the helix. For a given Ga , pitch decreases as $\bar{\rho}$ decreases.

Other very recent works include the study of effect of moment of inertia of the sphere on the path oscillation and characterizing the flutter to tumble transition behaviour by Mathai et al. [26]. The previous numerical work by Uhlmann and Dušek [4] has been extended to study of the secondary ice formation in clouds[27] by additionally accounting for the heat and mass transfer phenomena.

Drag characteristics

In general the C_d for freely falling spheres doesn't vary much with that of the fixed sphere scenario. The relation for variation of C_d with Re is given by Abraham (Eq.1.11) [8]. The main deviation in the C_d is observed for light spheres with high Ga or Re . Karamanev et al. [23, 24] for light rising spheres, reported sudden jump of C_d to 0.95 (constant thereafter) in the value beyond a critical Re . JDB also observed enhanced values of C_d for $Ga > 225$ and it more or less varied around 0.64 for $Ga = 350$. HW reported increased C_d values for $Ga > 874$ or $Re > 1550$ for spheres with ($\bar{\rho} = 0$ to 0.6) with C_d to be in the range of 0.75. VBL's experimental work aimed at suggesting new models for C_d by modelling an additional induced drag for rising spheres, and the results also decently agreed with the values reported by AM.

$$C_d = \left(\sqrt{\frac{24}{Re}} + 0.5407 \right)^2, \quad 0 \leq Re \leq 6000 \quad (1.11)$$

1.3. Motivation

As it is seen from the review of previous literature, dynamics of path instabilities and wake instabilities of a freely falling/rising sphere haven't been completely understood. All the disagreement between the previous works and with different results reported by every newly published work, show that the problem is still far from being explored fully. The crux of the entire literature review is summarized in Appendix A and is presented in such a way to highlight the disagreements and the differences in the regime threshold limits predicted earlier. The very recent study by Mathai et al. [26] where it was reported that, the path oscillations can be controlled by altering the moment of inertia, neatly finds direct application and high relevance in mixing/process-intensification phenomena which can be of great importance to process industries. Moreover, Chouippe et al. [27] have taken the study to the next level, which finds application in the meteorological research.

1.4. Research Questions

1. For the regimes where previous numerical works disagree with each other, which regimes are we able to reproduce experimentally?
2. Are there new regimes that haven't been observed earlier? If so, are the new results repeatable?
3. How do physical parameters like Strouhal number and drag coefficient differ in the present case from the results reported earlier?
4. Is it possible to draw consensus and disagreements of the present work with various older works to know where each one stands?

1.5. Research Goals and Approach to Studying the Regime Map

1.5.1. Research Goals

1. To design an experimental setup and image processing tools for studying the sphere motion in time.
2. To study the Ga vs $\bar{\rho}$ map thoroughly within the given time and available resources.
3. Validate the results for basic regimes where there is no disagreement between earlier works.
4. To perform a systematic set of experiments in order to populate the Ga vs $\bar{\rho}$ map and update it and present a new map.
5. Provide guidelines on the possible errors/uncertainties in the present results so that the present data is reliable for validation of new numerical models

1.5.2. Approach to Studying the Regime Map

The aim is to cover most path instabilities/regimes reported earlier in literature, test the validity and explore the characteristics of each regime systematically. Since the $Ga - \bar{\rho}$ parameter space is huge, it is of primacy to narrow down the region of interest from the existing maps from an experimental viewpoint. The older map by JDB, updated map from the same research group by ZD and the latest map by AM served as basis for identifying the regions of interest in the parameter space for the present investigation. Detailed regions chosen for investigation of the parameter space are given in chapter 3. Regions chosen for investigation can be broadly categorized into two types. First one being the regions in the parameter space where there is no disagreement in previous numerical works. These regimes have also been observed in experimental works and physical parameters also match well between authors. This region will serve as an excellent verification for the present experimental methodology and reliability of the new results. Second one is to cover the regions that

have been in continuous debate over the years and the present work will aim to investigate those regimes in detail by increasing the number of measurement points in those regions (by populating the map more in those regions). Since the $Ga - \bar{\rho}$ map is to be created by varying the parameters in Eq.1.1 and Eq.1.2, to vary the $\bar{\rho}$, spheres of different materials were purchased and to vary the Ga , the diameter of the sphere and the viscosity of the fluid were varied.

1.6. Structure of the Report

Following the introduction chapter, in the second chapter, the details of the experimental methodology are presented with the reader being directed to the supplementary information in the appendix for more details. Following it, is the results and discussion chapter, where the results for the falling cases are presented and followed by the results for the rising cases. A summary of the results and discussion is provided, where various works are compared to the present work and points of consensus and disagreement are presented. Finally, the conclusions of the entire work along with the recommendations for extension of the present work are given.

2

Experimental methodology

The goal of the present work is to track the 3D motion of a single settling/ascending sphere and capture various path instabilities accurately. The motion of a sphere is studied in a large tank and 3D particle tracking velocimetry is used to study the motion of the sphere in time. The current chapter aims at elucidating the various components of the experimental setup, the methodology employed in the systematic determination of dimensionless quantities, camera calibration, particle tracking algorithm and lastly post processing.

2.1. Experimental Setup

The design of the experiment should be cut out for tracking the 3D position of a sphere falling/rising in a tank containing still fluid. This underlines the need for high-speed imaging with cameras. The tank is illuminated using LED panels which facilitate the tracking of the sphere in time. In order to accurately capture the path instabilities, the spheres used should be perfectly round and devoid of any form of air bubbles inside. It is crucial to monitor the temperature in the tank since the Ga is a strong function of the viscosity. Ideally, one would want to release the sphere from rest and hence a very careful release mechanism is designed. Fig. 2.1 shows the overall view of the experimental setup. The individual components have been annotated for the purpose of clarity. In the following sub-sections, each component of the setup will be explained in detail.

2.1.1. The Tank

The experiments were performed in a glass tank of rectangular cross-section of dimensions ($0.30 \times 0.32 \times 1.5$ m) shown in Fig. 2.2. Size of the tank was chosen on the basis of the following conditions:

- The sphere is able to travel several hundred sphere diameters [3] before it reaches the field of view of the cameras.
- It is possible to track the sphere for sufficiently large distance ($70d_p$ for the largest sphere in the current study and $375d_p$ for the smallest one).
- There is no effect of side walls in the dynamics of the sphere motion [28].

Owing to the large volume (144 litres) of the tank, filtered tap water was used for all experiments and the viscosity was varied by controlling the ambient temperature in the room with air conditioning. In the present work, the water temperature was varied from 16 to 30 °C. Careful temperature control of the room was crucial as Ga can vary significantly even with 1 degree increase in temperature. At

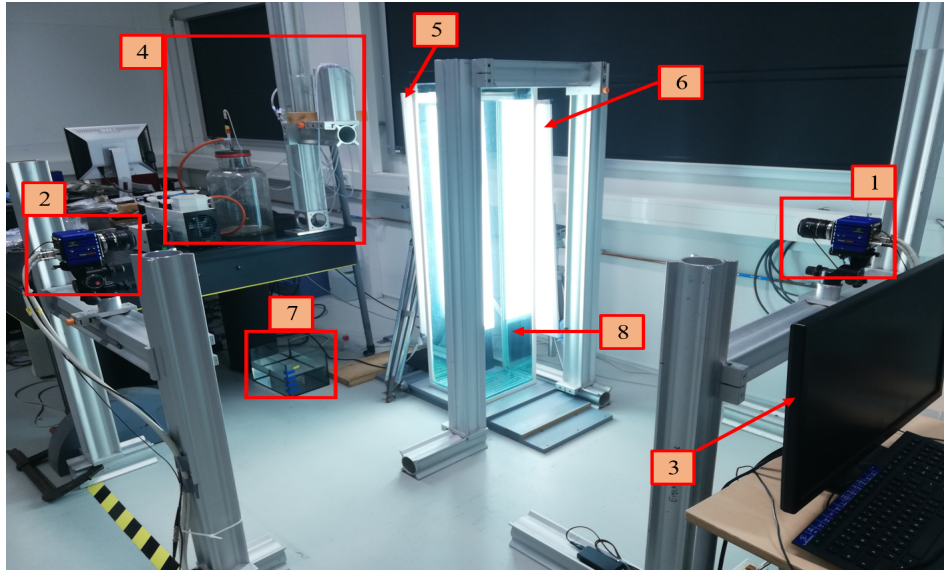


Figure 2.1: Experimental setup with the components annotated as, 1 & 2) Cameras, 3) Acquisition PC, 4) Components of the sphere release mechanism, 5 & 6) LEDs, 7) Water bath for pre-wetting the sphere before release, 8) Tank

the same time, it is important to check the presence of any temperature gradients along the height of the tank. A PT-100 sensor (Fig. 2.3) was used to measure the temperature of water. The accuracy of the PT-100 probe was tested and found to be $\pm 0.2\text{-}0.3^\circ\text{C}$. Water temperature was measured at the top and bottom of the tank before and after experiments to check the absence of any gradients in temperature. Typical temperature difference in the top and bottom of the tank was $0.1\text{-}0.2^\circ\text{C}$. The tank was drained and refilled once in 3 to 4 days owing to the increase in the level of contamination over time for still water.

2.1.2. Precision Spheres

As mentioned in section 1.5.2 the sphere material and diameter were varied in order to cover a broad range in the $Ga - \bar{\rho}$ map. A very vital part of the whole experimental procedure was the quality of the

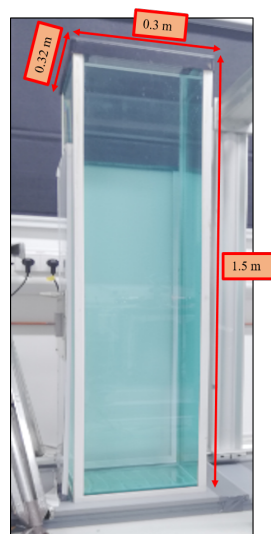


Figure 2.2: Tank

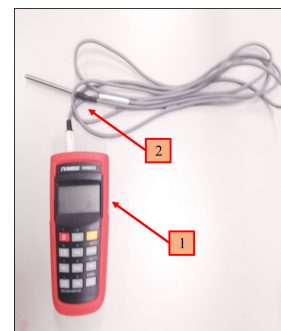


Figure 2.3: PT 100 temperature sensor, 1) Multi-meter, 2) PT-100 probe

spheres used. The quality of the spheres used can have a significant impact on the regime of motion of the sphere. Precision spheres (with sphericity $\gtrsim 0.99$ and $\lesssim 1$) of a wide range of diameters with densities ranging from 870 kg/m^3 to 6000 kg/m^3 were purchased from DIT Holland BV. Within these densities, a major portion of the regime map could be covered. Although a clear disagreement between various literature can be seen for lower $\bar{\rho}$ in the maps by ZD and AM, such low $\bar{\rho}$ weren't considered for the present study. Densities lower than 500 kg/m^3 couldn't be covered simply due to the unavailability of spheres in such density ranges. Also based on the fact that, earlier experiments used hollow spheres to cover these $\bar{\rho}$ ([13],[1]), where VB reports several improper trajectories obtained due to usage of hollow spheres which they attribute to the inhomogeneity in mass distribution in such hollow spheres. The recent paper by Mathai et al.([26]) shows that the use of such hollow spheres can significantly impact the type of motion taken by the sphere due to the change in moment of inertia. The properties of the spheres used in the present study are listed in Table 2.1. Despite careful selection of the spheres, for plastic spheres, namely Polypropylene and Nylon, the presence of small air voids was inevitable from the supplier end since injection moulding was used to manufacture the spheres. This is evident from the histogram of density of the spheres where, we can see a deviation from the value specified by the supplier (Appendix E - Fig.E.1 and Fig.E.2).

Table 2.1: Sphere specifications

| Material | Type | Density (kg/m^3) | Diameter (mm) |
|-----------------|---------|-----------------------------|---------------------------|
| Polypropylene | Plastic | 870 | 2, 3.5, 4 |
| Nylon | Plastic | 1120 | 2, 3, 4, 4.5, 5.556, 6.35 |
| Silicon Nitride | Ceramic | 3190 | 1.2, 2.381 |
| Aluminium Oxide | Ceramic | 3900 | 1.2, 2, 2.381 |
| Zirconium Oxide | Ceramic | 6000 | 1.5875 |

2.1.3. Estimation of the Galileo number

The Ga estimation was the most important and critical part of the experimental campaign. From Eq.1.2, it can be seen that Ga is a function of diameter, viscosity, fluid density and solid density. Estimation of these quantities are not as simple as they seem. Even a slight misprediction can land us in another regime, which we may wrongly characterize. The density and kinematic viscosity of water are determined from the temperature using an online tool-engineering toolbox [29]. The density and diameter of the spheres have a tolerance which are specified by the supplier. For example, in the case of Nylon, the tolerance in diameter is $25 \mu\text{m}$ to $50 \mu\text{m}$. This tolerance is much lower for ceramics owing to the high quality of manufacturing. This tolerance gives Ga a mismatch from the predicted value, making it very difficult if the values given by the supplier are used at face value. Hence the mass and diameter of the individual spheres were measured to accurately determine the Ga . Each sphere was stored in separate Eppendorf tubes (shown in Appendix H Fig.H.2) and given an identification number. The mass of individual spheres was measured using weighing scale with a least count of 0.01 mg (shown in Appendix H Fig.H.1). The diameter was measured using a microscope, where the images of each sphere for several planes were recorded and the diameter was computed from the images using a Circular Hough transform method (Appendix B). From the mass and diameter, the Ga and $\bar{\rho}$ could be computed with good accuracy. Moreover, plastic spheres like Nylon absorb water and hence, it was dried in an oven at 40°C and the measurements of mass and diameter were repeatedly performed. The variation of mass with water absorption for different materials is given in Appendix C.

It is important to note that, there are uncertainties involved in the measurement of mass, diameter

and water temperature. Hence a careful uncertainty analysis was performed (Appendix D) and the uncertainty in Ga , $\bar{\rho}$, Re and C_d are quantified systematically for every case investigated.

2.1.4. Releasing the Spheres

As mentioned in the beginning of this chapter, the release mechanism is a very important part of the experiment as one would ideally want the sphere to be released from rest with the initial perturbations being as low as possible. However, no method of releasing can guarantee zero initial perturbations. Also, there is a good chance that the initial perturbation may affect the final path taken by the sphere. The effect of different release mechanisms have not been reported in literature. In order to be confident of the results, in the present work we intend to choose different mechanisms, and study the effect of each on the path taken by the sphere. The results show that there is no effect of the methodology adopted to release on the final path taken by the sphere. The results of the release mechanism are presented in chapter 3.

When releasing, the fluid in the tank is expected to be at rest with disturbances being as low as possible. Once the sphere is released and the motion is recorded, the next experiment is performed after 15 minutes to allow the disturbances to die down [30]. The sphere which settles down in the tank is removed using suction, where a long rod is inserted into the tank with a tubing network connected to the vacuum pump. This would create large amount of disturbances in the fluid due to motion of the long rod inside the tank. In this case, the next experiment is to be performed with a minimum gap of 2 hours [1]. Typically, four experiments are performed with gap between each being 15 minutes. Then, the spheres are collected from the bottom and the next experiment is conducted after 2 hours.

2.1.4.1. Release Mechanism - Falling sphere

To release the sphere from the top of the tank, three different mechanisms were tested. The three mechanisms were chosen such that, each varies in the degree of initial perturbation that each can create.

Tweezer

Usage of the tweezer (shown in Fig. 2.4) is the most simplest of the tested release mechanisms. Using a tweezer as a release tool was recently reported by Toupoint et al. [30]. The sphere is pre-wetted (to avoid possibility of air bubbles being created when released) and is held by the tweezer. It is gently taken below the free surface of the tank and released manually. This method can create a large initial perturbation on the sphere due to manual release. But this method, practically takes very less time and is simple to carry out.



Figure 2.4: Tweezer

Vacuum Suction

The sphere is held by vacuum suction using a vacuum pump. A schematic is shown in Fig. 2.5 a. The tubing line to the sphere from the vacuum pump is laid out on a cross member or a bar which rests on the surface of the tank. The connection between the sphere and the vacuum pump is through this tube network. A leur valve was used to cut off the vacuum pump from the sphere. This would cause the sphere to be released eventually. An important point to note here is that, there is always a mild up/down flow of water through the interface where the sphere is held (marked as 3 in Fig. 2.5 b). Due to this there is a constant flow of water through the tubing and hence a drain chamber was used to collect the water. This has an advantage as well as a disadvantage. The advantage being that, due to constant water flow through the tubing, there is no presence of any air bubbles in the tubes and closing of the valve would mean that the sphere has water on either side (side exposed to the tubing line and the side exposed to the tank). This will cause a smooth release without any initial impulse being generated onto the sphere due to the built up pressure by the vacuum pump. The drawback is that, due to this mild down flow, the fluid close to the sphere is always disturbed and in motion.

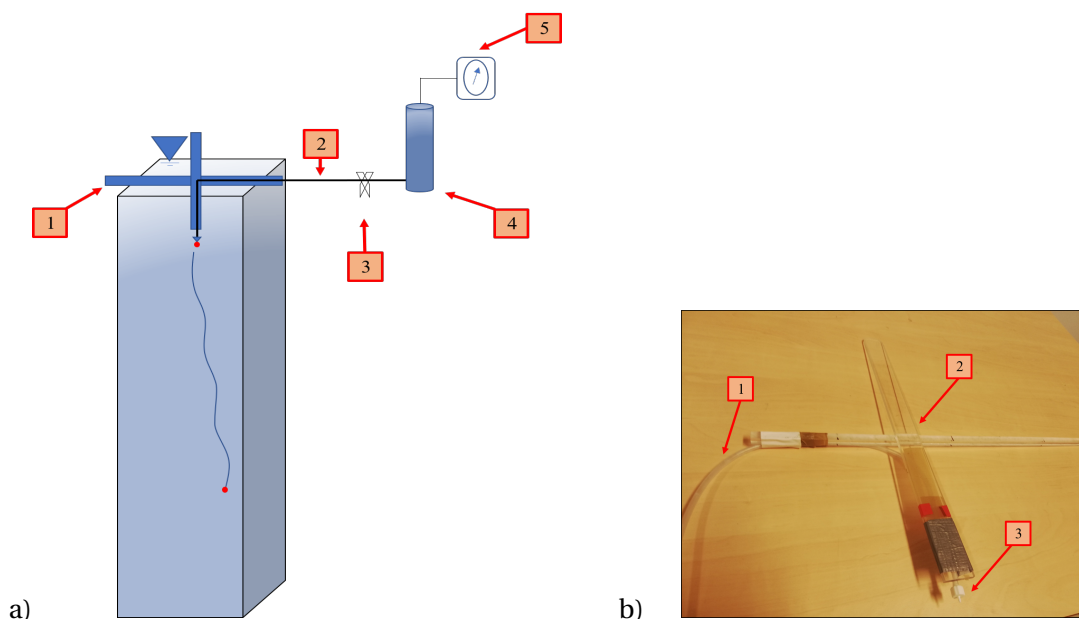


Figure 2.5: a) Schematic of vacuum suction release mechanism with annotations 1) Cross bar, 2) Tubing line, 3) Valve, 4) Drain chamber, 5) Vacuum pump, b) Cross bar with annotations 1) Tubing, 2) Cross bar, 3) Interface where sphere is held

Robotic Gripper Arm

Due to the disadvantages of the above mechanisms, as a final test, a robotic gripper arm (Fig. 2.6) was also tested. Similar to the vacuum suction setup, the gripper is mounted on a bar which is allowed to rest on the tank. The sphere is held by the arms of the robotic gripper. The gripper is employed with a servo motor, which is connected to an Arduino. The speed of the motor was controlled using a simple program (Appendix F), which causes a gentle release of the sphere.

2.1.4.2. Release Mechanism - Rising sphere

Releasing a sphere from the bottom of the tank is much more tricky and not straightforward as the falling counterparts. It was achieved through the use of vacuum suction. The schematic of the set up is shown in Fig. 2.7. The full scale set up has many intricacies and is hence depicted in detail in Appendix G. The vacuum suction tubing network is taken to the bottom of the tank by guiding the tubes through a long rod. At the bottom end of the rod, a provision is made for four spheres to

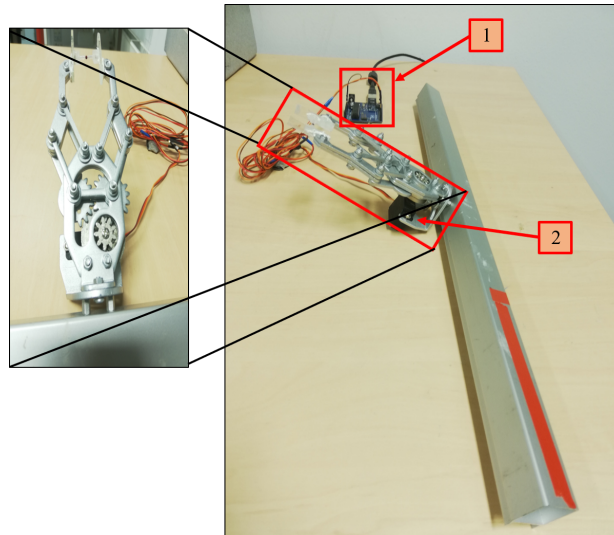


Figure 2.6: Robotic gripper arm with annotations, 1) Arduino and 2) Servo Motor

be held under suction. The rod is left immersed in the tank for two hours with the vacuum pump switched on, thereby holding the spheres at the bottom of the tank till all the disturbances created die down. Then, each of the spheres are released one after the other with the 15 minutes gap, similar to the procedure mentioned for falling spheres. The releasing of the spheres is achieved by using a 4-valve connection, with each valve being connected to one sphere, each sphere can be cut off from the vacuum pump by closing the valves independently.

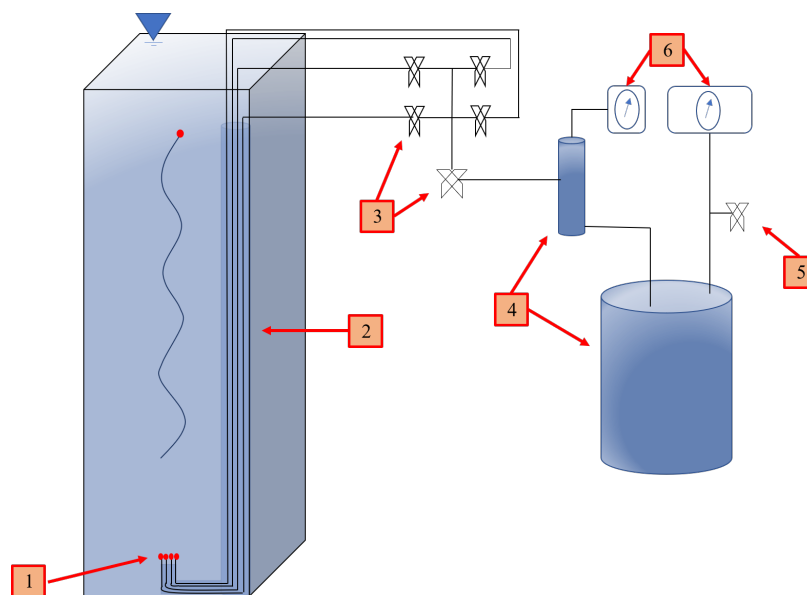


Figure 2.7: Schematic of release mechanism for rising sphere with annotations 1) Spheres held under suction, 2) Tubing lines, 3) Valves, 4) Drain chambers, 5) Pressure relief valve and 6) Vacuum pumps

2.1.5. High speed cameras and LED

A pair of synchronized high speed cameras was used to image the motion of the sphere and track it. Based on the availability, either a pair of Imager sCMOS or a pair of Imager Pro HS cameras were used (shown in Fig. 2.8). The f-number (ratio of the diameter to aperture) of the lens was set to

16 in order to have a greater depth of field in the tank. The frame rate of the cameras was chosen (based on Nyquist sampling theorem) to be greater than at least twice the frequency based on the gravitational time scale (Eq.1.6) of the sphere. It ranged from 50 to 500 Hz depending upon the case investigated. Both the cameras had a field of view of 45cm in the vertical direction, which provides adequate distance to track the sphere in time. Depending upon the camera used, the resolution was 0.208 mm/pixel for Imager sCMOS and 0.223 mm/pixel for Imager Pro HS. Two LED panels was used for backlighting on which the moving sphere would present itself as a dark circle on the bright illuminated background. The schematic of the camera and LED setup is depicted in Fig. 2.9

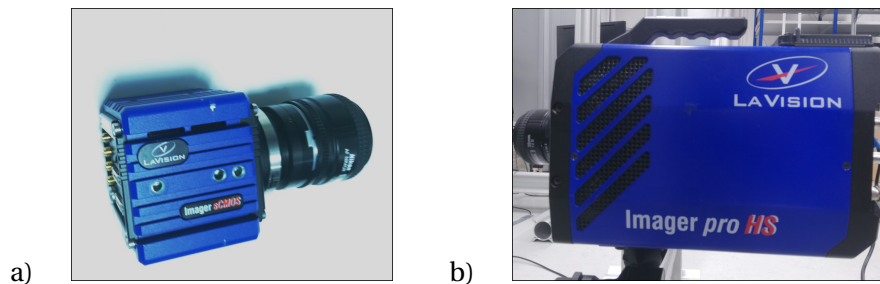


Figure 2.8: a) Imager sCMOS camera and b) Imager pro HS camera

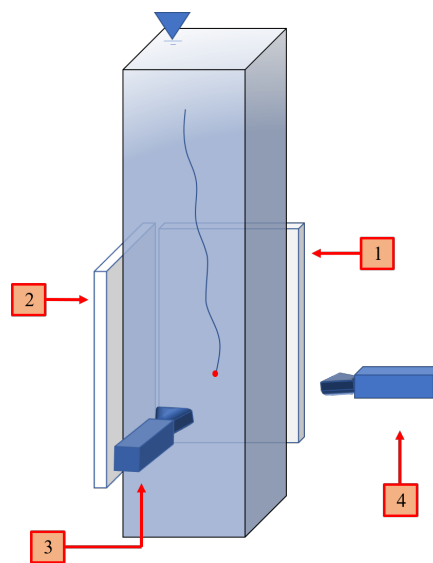


Figure 2.9: Schematic of camera and LED setup, with annotations 1&2) LEDs, 3&4)Cameras

2.1.6. Camera calibration

A proper calibration of the camera is essential to account for various refractive indices (air, glass and water) and correct for various other distortions. An in-situ calibration procedure following the work of Soloff et al. [31] was used to relate the coordinates in the object space ($[x, y, z]^T \in \mathbb{R}^3$) and the image space ($[X, Y]^T \in \mathbb{R}^2$). This is obtained through a mapping function (f). The mapping function in this case is a 3rd order polynomial. Here, two polynomials are fit for x and y directions. They are given by equations 2.1 and 2.2 for X and Y coordinates respectively.

$$X = c_0(z) + c_1(z)x + c_2(z)y + c_3(z)xy + c_4(z)x^2 + c_5(z)y^2 + c_6(z)x^2y + c_7(z)xy^2 + c_8(z)x^3 + c_9(z)y^3 \quad (2.1)$$

$$Y = c_0(z) + c_1(z)x + c_2(z)y + c_3(z)xy + c_4(z)x^2 + c_5(z)y^2 + c_6(z)x^2y + c_7(z)xy^2 + c_8(z)x^3 + c_9(z)y^3 \quad (2.2)$$

This method is the most preferred as it accounts for all the aforementioned issues. The calibration procedure involved in the present study is briefly described as follows:

- A grid (with crosses) is placed within the field of view inside the tank filled with water. The distance between the crosses is constant and is known apriori (20.2 mm in this case). This is depicted in Fig. 2.10. The grid is mounted on a mechanical traverse (shown in Fig. 2.10) which allows an out of plane motion of the grid within the tank.
- The cameras are made to focus the crosses and corresponding images are recorded. From the recorded images in each camera, the marker positions are found out (depicted in Fig. 2.11 a).
- With the known positions of the markers, a 3rd order polynomial is fit through the located markers with the distance between the adjacent markers known in the object space. This 3rd order polynomial maps the physical object plane onto the camera plane (Fig. 2.11 b). The 3rd order polynomial is fit in x and y directions. At this point four different polynomials are obtained for the two cameras.

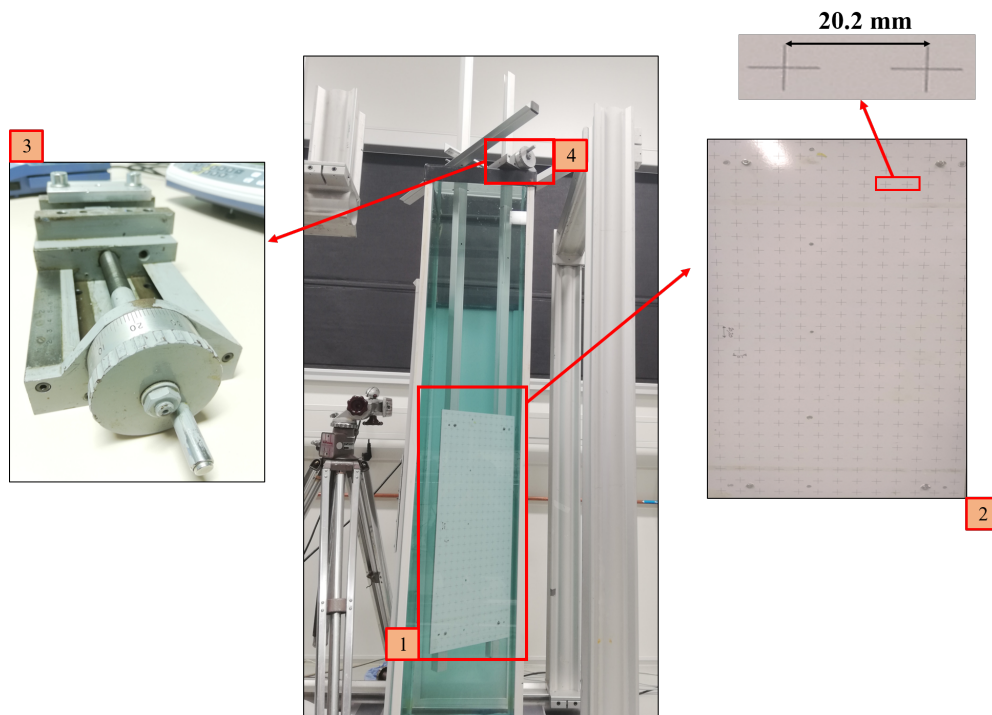


Figure 2.10: Calibration setup with annotations, 1&2) Calibration grid, 3&4) Mechanical traverse

- The grid is then moved inside the domain to a known distance, which in this case is 40 mm (this is sufficient to cover the total extent of the out of plane motion of the sphere in the present study). With the moved grid, in the new plane, four new polynomials are fit there by obtaining eight different polynomials which are then used to compute the 3D coordinate of the sphere.

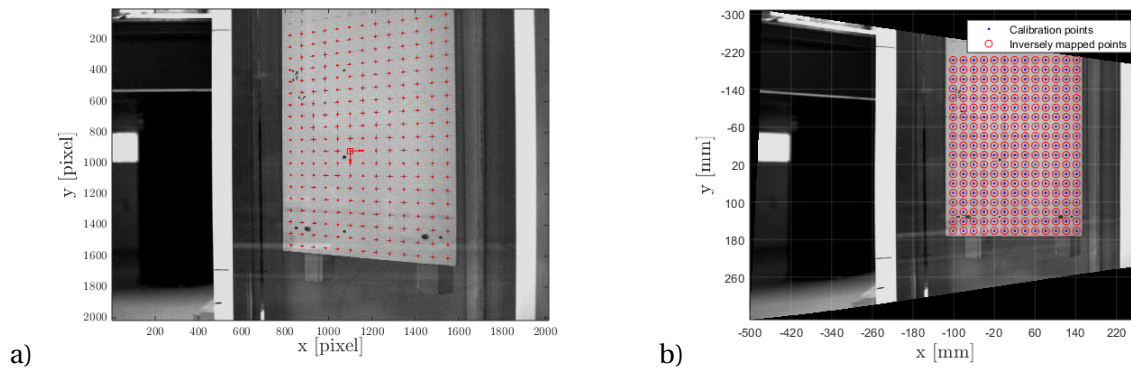


Figure 2.11: a) Grid with marker locations detected b) Back projected Image

Errors in calibration are unavoidable but systematic. Hence, we expect a systematic uncertainty. The calibration error is caused due to least squares fitting of the mapping function and due to the error made in the estimation of marker positions. In the present study, from the data considering all the calibration performed, RMS error of the calibration ranges from 0.09 mm to 0.2 mm which are approximately 0.4 to 0.89 pixels.

2.2. 3D Particle Tracking Algorithm

The particle tracking algorithm was implemented in MATLAB following the works of Mass et al.[32] and Nicholas et al.[33]. The methodology adopted is summarized in the flow chart below. (Fig.2.12)

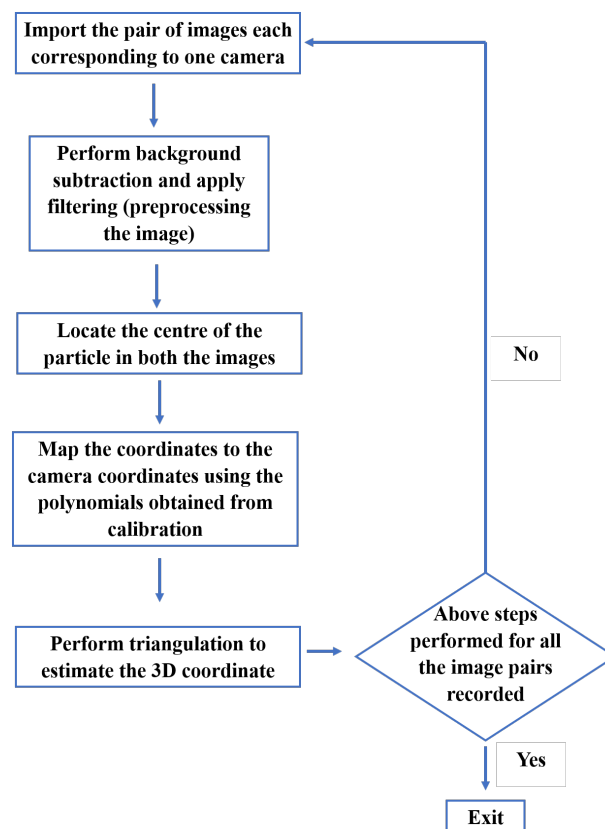


Figure 2.12: Flow chart describing steps involved in the Particle tracking algorithm

Each step is elaborated as follows:

1. Two images corresponding to the each of the cameras are imported. These are the raw images and are depicted in Fig.2.13 a.
2. Each of these raw images is subtracted with the background image, which in this case is the image taken before the particle being released. On subtraction, any form of unwanted spurious information in the image will be removed, thereby leaving us with a bright circle (particle) on a dark background. Following this, a band pass filtering is done using a MATLAB routine *bandpass.m* (from the work of Daniel et al. [[34]]) to further smoothen out the bright spot (Fig.2.13 b).
3. To estimate the centre of the bright circle, firstly, the pixel position corresponding to the highest intensity is found out. Then a search window is defined around this high intensity pixel. Using the (x, y) values and the intensity values $(I(x, y))$ of the pixels within this search window, a weighted centroid averaging method ([33]) is implemented to compute the centre of the particle (Fig.2.13 c). The corresponding equation is as follows

$$(x_c, y_c) = \left(\frac{\sum_{n=1}^N x_n I(x_n, y_n)}{\sum_{n=1}^N I(x_n, y_n)}, \frac{\sum_{n=1}^N y_n I(x_n, y_n)}{\sum_{n=1}^N I(x_n, y_n)} \right) \quad (2.3)$$

Here (x_c, y_c) is the centre coordinates of the particle, n stands for the index of the pixel within the search window considered and N is total number of cells within the window. (x_n, y_n) are the coordinates of each pixel with intensity $(I(x_n, y_n))$. Thus, at the end of this step, we obtain two coordinates, $(x, y)_{camera_1}$ and $(x, y)_{camera_2}$.

4. With the particle centres computed from both the images, the centre coordinate in each image is mapped onto the two calibration planes using the polynomials obtained from calibration. Thus, we will have four (X, Y) coordinates, namely, $(X, Y)_{c_1, p_1}$, $(X, Y)_{c_1, p_2}$, $(X, Y)_{c_2, p_1}$ and $(X, Y)_{c_2, p_2}$ where subscripts c and p corresponds to camera and plane respectively.
5. Triangulation is performed with the four coordinates to reconstruct the 3D coordinate [35]. The 3D coordinate will be the spatial intersection of the lines connecting the coordinates in plane 1 and plane 2 in both the cameras (depicted in Fig.2.14). The 3rd estimated coordinate will be the midpoint of the shortest line joining the two lines (corresponding to two cameras).
6. The above steps are repeated for all image pairs acquired from the experimental run.

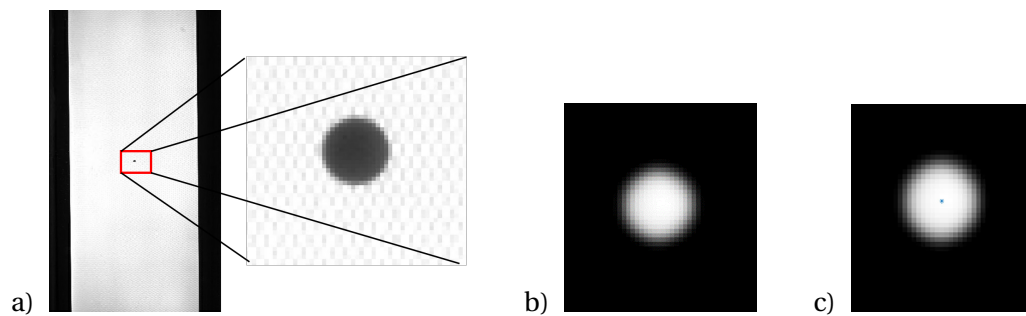


Figure 2.13: a) Raw Image, b) Image after preprocessing, c) Centre position estimated

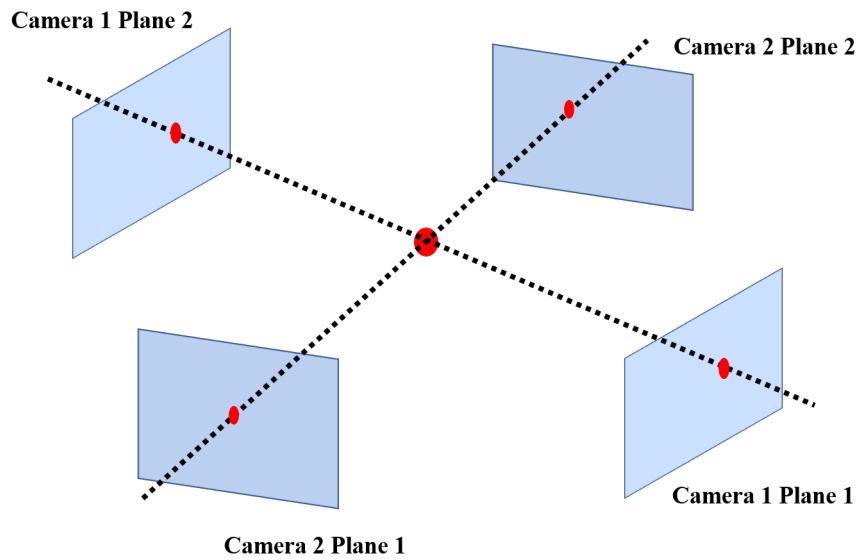


Figure 2.14: Estimation of 3D coordinate from the 2D coordinates from four different planes

2.3. Post Processing

2.3.1. Signal Filtering

The position coordinates obtained from the particle tracking routine often have noise associated to them due to the finite pixel size. Although, the position signal wouldn't look much noisy, upon taking derivatives to compute velocity or acceleration, the noise will be amplified. It is often not possible to get rid of the noise unless some kind of filtering is employed. In the present work, Savitzky Golay filter[36] is employed, which is a moving polynomial filter. For a given frame length (set of points), a polynomial of order 3 is fit through the points. This polynomial can then be analytically differentiated to compute higher order statistics like velocity and acceleration.

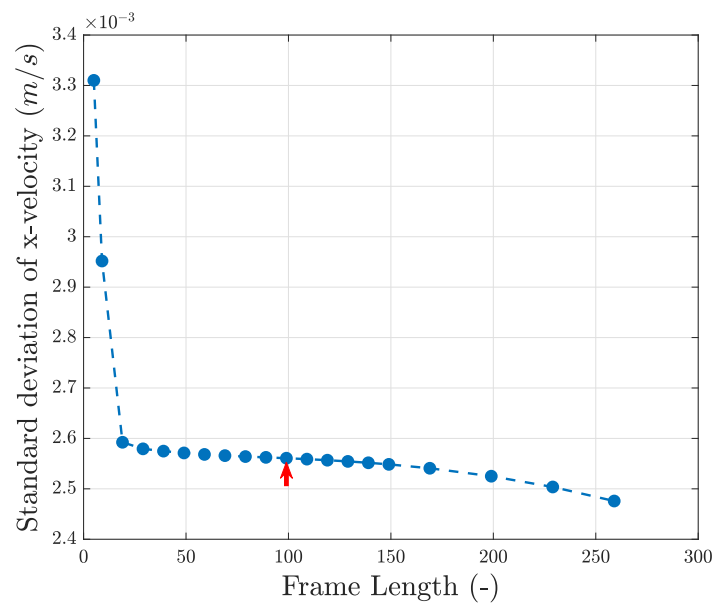


Figure 2.15: Variation of standard deviation of x-velocity with frame length employed. Red arrow depicts the chosen filter length

It is crucial to decide the frame length within which the polynomials are to be fit. It should be done in such a way that, only the noise is filtered without affecting the physical scales in the signal. In order to decide the frame length, many different frame lengths were tested and the standard deviation in the velocity signal was plotted with respect to the frame length. With increase in frame length, in the plot, there will be a region where the standard deviation will drop immediately (noise being filtered out), then we will observe a region where with increase in frame length the standard deviation will almost remain same (zone where noise is still filtered). This region is critical as beyond this region the curve will again drop down thereby filtering the physical scales in the signal. This is depicted for one such case in Fig.2.15. In the shown example, a frame length of 99 was chosen. Deciding the right frame length for a signal will depend on the frame rate and gravitational frequency of the sphere. Since the gravitational frequency is majorly a function of density of the sphere, the frame length used to filter the signal will vary for different materials of the spheres used. Similar analysis for deciding the frame length had been done for other cases as well and are shown in Table 2.2

Table 2.2: Frame length employed in Savitzky Golay Filter

| Material | Density (kg/m ³) | Frame Rate (Hz) | Frame Length |
|-----------------|------------------------------|-----------------|--------------|
| Nylon | 1120 | 100 | 39 |
| Nylon | 1120 | 500 | 99 |
| Polypropylene | 870 | 50 | 19 |
| Silicon Nitride | 3190 | 500 | 49 |
| Aluminium Oxide | 3900 | 500 | 49 |
| Zirconium Oxide | 6000 | 500 | 29 |

2.3.2. Correcting Spectral Leakage

Computing the spectrum (Eq.2.4) is very important in the present work, since we want to quantify the dominant frequencies in the signal. The spectrum will be used extensively in chapter 3. In order to compute the FFT, it is implicitly implied that the signal is periodic and the Fourier series are representative of the periodic extension of the signal (using different amplitudes and frequencies of sines and cosines).

$$F(f) = \int_{-\infty}^{\infty} w(t) f(t) e^{-i2\pi f t} dt \quad (2.4)$$

where F is the output frequency spectrum, f is the input time series signal and w is the window function which is a rectangular window (simply '1' inside the window and '0' outside the window). Since the default window used is a rectangular window, if the series is not periodic we can see a sudden blip (similar to an impulse). It might be the case that, any additional frequencies or possibly all frequencies may be required to represent the blip. This causes spectral leakage, where, due to the presence of the additional frequencies that are needed to represent the blip, the energy in one bin spreads to multiple bins creating what is called spectral leakage. In the present work, since we do not have a large time series of the signal, it is necessary to smoothen the edges of our signal to avoid spectral leakage. This is done by employing a Hanning window which is represented by Eq.2.5 (in the discrete form).

$$w(n) = 0.5 \left(1 - \cos\left(\frac{2\pi n}{N}\right) \right) \quad (2.5)$$

Moreover owing to the drifting motion of the sphere, a correction for a linear trend in the signal is also required. So the following steps were carried out

1. The horizontal velocity signal $\left(v_h = \sqrt{v_x^2 + v_z^2} \right)$ is chosen to compute the FFT.

2. A line is regressed through the points of the signal and the signal is subtracted with the regressed line. This would leave us with a signal corrected for any kind of drifting motion. Moreover, we will be left with the horizontal velocity fluctuations in the signal (v'_h) (depicted in Fig.2.16).
3. A Hanning window is used to correct for the spectral leakage by suppressing the end effects in the signal and shifting the focus to the centre portion of the signal. (depicted in Fig.2.17)

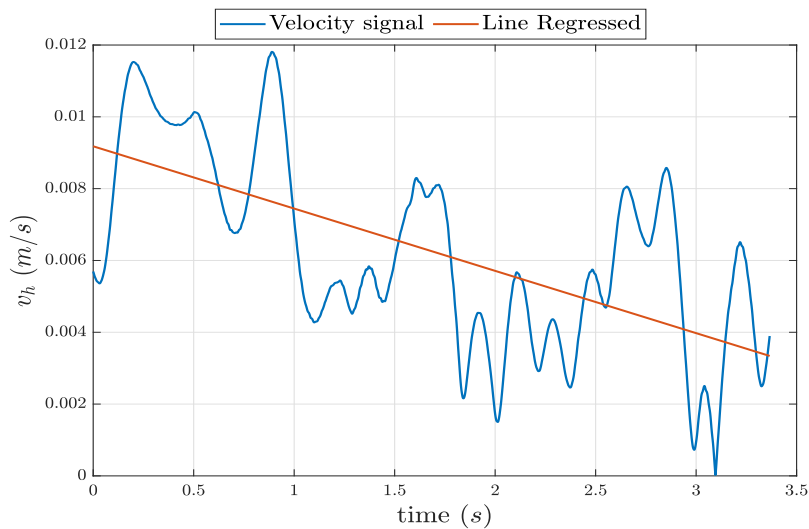


Figure 2.16: Plot of the velocity signal and line regressed through the signal to correct for drift

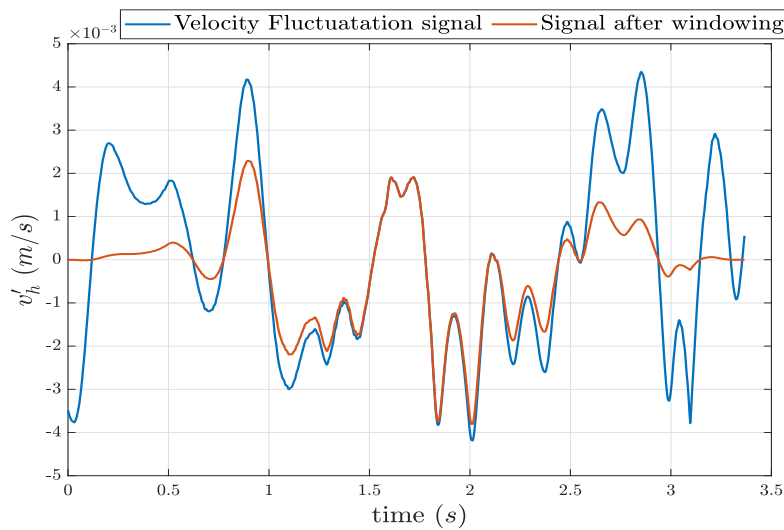


Figure 2.17: Plot of velocity signal corrected for drift and plot of velocity signal after applying the Hanning window

3

Results and Discussion

3.1. Test for repeatability and effect of release mechanisms

For one particular type of regime of motion - 'oblique oscillating regime' (which will be established later in this chapter), the effect of the different release mechanisms were tested and the same regime was repeatable in all the cases. This shows that the initial perturbations (if any), die down as the sphere has a long distance of travel before it reaches the field of view. This also proves repeatability of the results. The results for the three release mechanisms are shown in Table 3.1. Since the release mechanism has no effect on the repeatability or the path of motion taken up by the sphere, the tweezer was used for all other cases to release the freely falling spheres owing to its simplicity and a vacuum suction was used to release the spheres from the bottom of the tank.

Table 3.1: Results of different release for a sphere with $Ga = 178$ and $\bar{\rho} = 1.12$

| Physical Parameter | Tweezer | Vacuum Pump | Robotic Arm |
|---|---------|-------------|-------------|
| Mean fall velocity (mm/s) | 87.95 | 87.93 | 87.73 |
| Angle of fall with vertical($^{\circ}$) | 6.11 | 4.27 | 7.93 |
| Strouhal Number (-) | 0.058 | 0.0601 | 0.046 |

3.2. Establishment of regions of interest and jargon used

Although the abbreviations for the most relevant literature were established in chapter 1 , for the sake of clarity, the abbreviations used are tabulated below. This is mainly because, in the present chapter and the chapters to follow, we will refer to the earlier works extensively.

Table 3.2: Abbreviations for relevant literature

| Abbreviation | Author(s) and Research Article | Type of work (Experimental/Numerical) |
|--------------|--------------------------------|---------------------------------------|
| JDB | Jenny et al. [3] | Numerical |
| VB | Veldhuis and Biesheuvel [13] | Experimental |
| HW | Howrowitz and Williamson [1] | Experimental |
| ZD | Zhou and Dušek [6] | Numerical |
| AM | Auguste and Magnaudet [7] | Numerical |

For the freely falling cases, the map of ZD (depicted in Fig.3.1) is taken as the reference (note that this is the updated map from the older map of JDB by the same research group). We don't consider

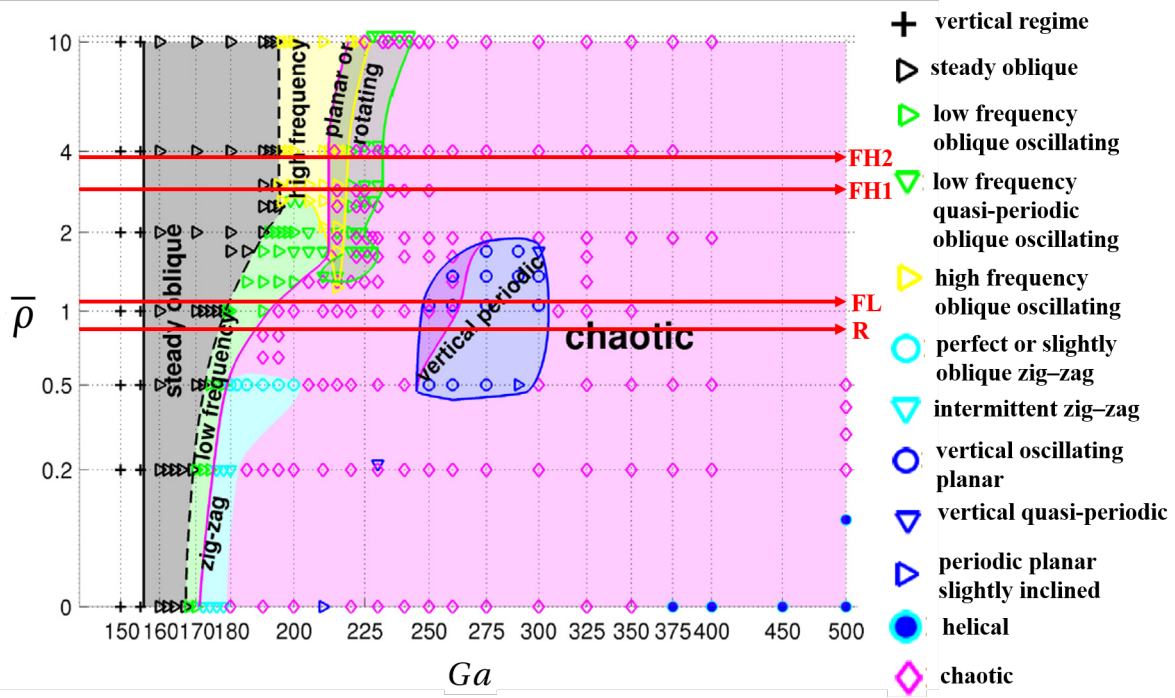


Figure 3.1: Regime map by Zhou and Dušek [6] representing various trajectories of ascending/falling free sphere and horizontal red lines represent the region investigated in the present study, x and y axis are same as Fig.1.3

the map of HW here because the results completely vary from other works. Few of the regimes reported in the map of JDB were experimentally verified by VB. But the results of HW don't agree with either JDB or VB or ZD. So, in order to choose the regions of present study, we shall rely on the results of JDB and ZD as some of their results have also been substantiated experimentally. It is important to realize that this approach is only used here to choose the regions of interest in the map. The results obtained, however will be compared with all the above works. Similarly, for rising cases the map of ZD (depicted in Fig.3.1) and the map of AM (depicted in Fig.3.2) are collectively taken as the reference as both are very recent and also disagree with each other in some cases, hence it will be worthwhile to choose both together.

For the falling cases, a wide range of Ga and three different $\bar{\rho}$ (namely 1.12, 3.19 and 3.9) are investigated (depicted in Fig.3.1 by horizontal red lines). It is clear from the map that, the transition to different regimes upon increasing Ga is different for $\bar{\rho} < 2.5$ and $\bar{\rho} > 2.5$. Hence, we would like to cover $\bar{\rho}$ in both the cases for a range of Ga , thereby covering as many regimes as possible. In this chapter, the cases of $\bar{\rho} < 2.5$ will be called 'low density' cases, whereas, the cases with $\bar{\rho} > 2.5$ will be the 'high density' or 'dense cases'. For rising cases, a single $\bar{\rho}$ (namely 0.87) is considered in the present work (depicted by the horizontal red line in Fig.3.1 and Fig.3.2).

So, for the falling cases, we narrow down our regions of investigation from the map of ZD. The lines FL, FH1 and FH2 shown in Fig.3.1 are the lines that are considered for investigation. Here, FL stands for falling cases (F) and low density (L) and hence denoted FL. By low density, it shouldn't be thought of as a rising sphere with $\bar{\rho} < 1$, rather, it is a falling case (with $\bar{\rho} \approx 1.12$). For $\bar{\rho} > 2.5$, we see lines FH1 and FH2, where F stands for 'falling' and H stands for 'high density'. Lines FH1 and FH2 correspond to a $\bar{\rho} \approx 3.19$ and 3.9 respectively. The above method of identification was chosen in such a way that,

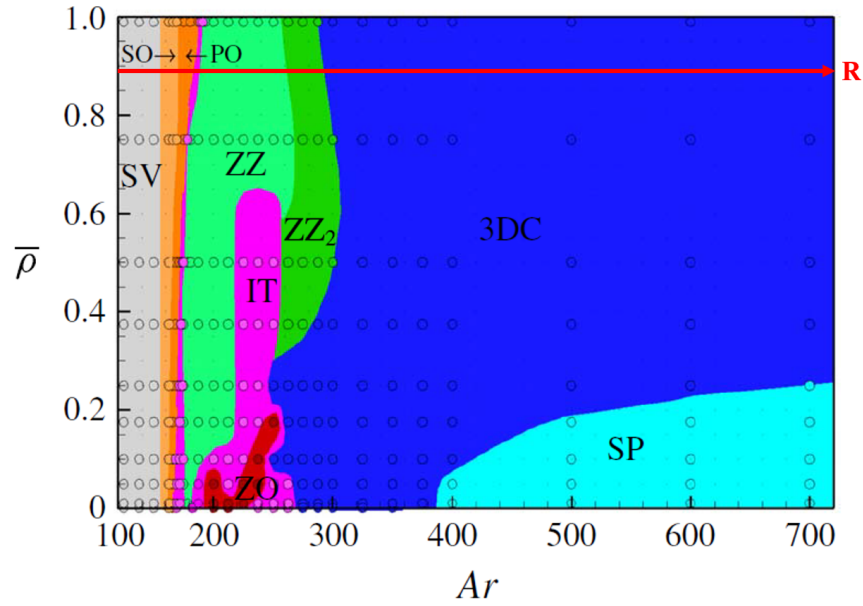


Figure 3.2: Regime map by Auguste and Magnaudet [7] presenting various trajectories of freely ascending sphere (here Ar stands for the Archimedes number, which by definition of AM is same Ga), and horizontal red line represents the region investigated in the present study. The annotations are as follows: SV - steady vertical, SO - steady oblique, PO - periodic oscillating, ZZ - zigzagging, ZZ_2 - zigzag-2, IT - intermittent, ZO - oblique zigzagging, SP - spiralling, 3DC - chaotic

we are able to make a distinction between $\bar{\rho} < 2.5$ and $\bar{\rho} > 2.5$. This is because the route to transition to chaos is different for $\bar{\rho} < 2.5$ and $\bar{\rho} > 2.5$. Although the route to transition to chaos is almost the same when moving along lines FH1 and FH2, it will be seen that the results obtained in both the cases will complement each other, thereby giving more confidence in our results. Apart from the three $\bar{\rho}$ probed for the falling cases a fourth $\bar{\rho} \approx 6$ was also studied. But for $\bar{\rho} \approx 6$, the transition to different regimes was not studied and rather only 2 different cases were studied to test a simple hypothesis (further elaborated in section 3.4). For rising cases ($\bar{\rho} < 1$), line R is shown in Fig.3.1 and Fig.3.2, here R denotes rising and corresponds to $\bar{\rho} \approx 0.87$. In this chapter, first, the results for FL will be discussed, then the results for FH1 and FH2 will be discussed together and finally the results for the rising cases (R) will be discussed.

It is important to note that, whenever it is mentioned ‘moving along line FL’, it means that, for a fixed $\bar{\rho}$, the Ga is increased. All the plots presented in this chapter are non-dimensionalized and the relevant normalization parameters are listed below.

1. Position is normalized with the sphere diameter (d_p).
2. Velocity of the sphere (v_x , v_y and v_z) is normalized with the gravitational velocity (v_g - Eq.1.4).
3. The magnitude of horizontal velocity fluctuations (v'_h) is normalized with the gravitational velocity (v_g - Eq.1.4).
4. The frequency is normalized by the gravitational frequency (f_g - Eq.1.6)

3.3. Focus of the present work

The falling and rising spheres, irrespective of $\bar{\rho}$, for a $Ga < 155$, will have an axisymmetric wake and will fall/rise in a steady vertical or rectilinear path. The older map by JDB and the updated version

by ZD report the above threshold without any disagreement. Moreover, experimentally, this was observed by HW. The focus of the current work, will be on the non-vertical regimes for $Ga > 155$. It is important to note that a perfect vertical path is not possible to capture experimentally. The sphere will always have a drift that makes the path deviate from the strict vertical ones reported in literature. This drift is random and not reproducible. The drift is due to the presence of residual disturbances in the fluid which are practically not possible to get rid off. Moreover, the sphere is never a perfect/ideal sphere like the ones employed in numerical simulations. As mentioned in section 2.1.2, the sphericity is never equal to 1 and also the density values have a deviation from the values specified by the supplier owing to possible voids in the sphere (Appendix E). A similar argument is also reported by other works of Ellingsen et al.[37], Fernandes et al.[38] and Toupoint et al.[30] for bubbles and disks. Typical trajectories of steady vertical regime with a drift observed in the present study is shown in Fig.3.3. We see a drift and it is only 2.2% of the total distance travelled by the sphere. However, there are possible ways to correct for the drift, which is beyond the scope of the present work as we only aim at characterising various path instabilities involved and their associated disagreements in literature. Hence the numerical works are the best suited to characterizing such strictly vertical regimes. The focus of the present work will be to characterize and discuss the dynamics of non-vertical regimes.

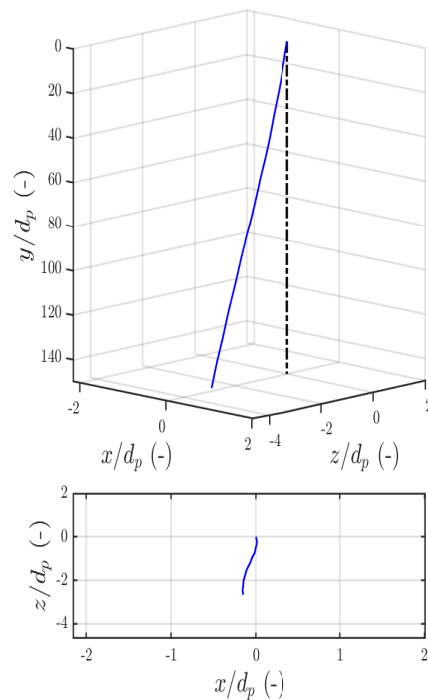


Figure 3.3: Drifting Steady vertical trajectory for $\bar{\rho} = 1.156$ and $Ga = 110.14$ falling with a mean vertical velocity of 0.056 m/s

3.4. Falling Sphere

3.4.1. Results low density cases ($\bar{\rho} \approx 1.12$)

The Steady Oblique Regime

Moving along Line FL in Fig.3.1, for $Ga > 155$, JDB report the breaking of the axisymmetric wake to a planar symmetric wake. The orientation of the symmetry plane is random in

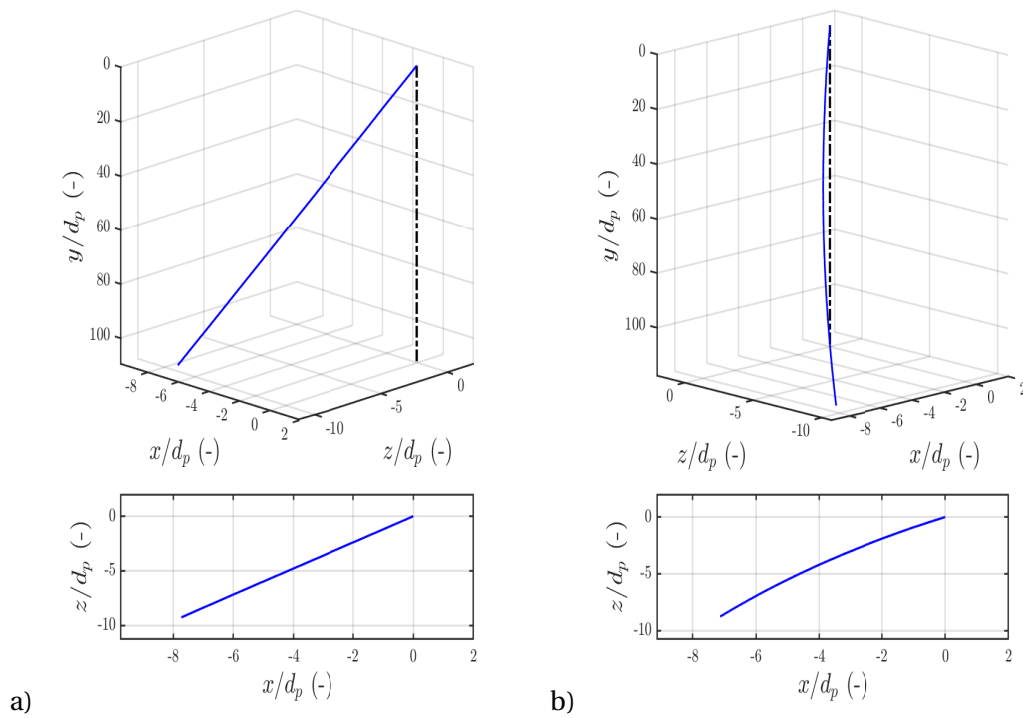


Figure 3.4: a) Steady oblique trajectory for $\bar{\rho} = 1.121$ and $Ga = 166.56$ falling at an angle of 6.27° with respect to the vertical with a mean vertical velocity of 0.0869 m/s and mean horizontal velocity of 0.0096 m/s, b) Steady oblique curved trajectory for $\bar{\rho} = 1.128$ and $Ga = 169.57$ falling at an angle of 5.23° with respect to the vertical with a mean vertical velocity of 0.0837 m/s and mean horizontal velocity of 0.0081 m/s.

the azimuthal direction and results in what is referred here as a ‘**Steady oblique**’ regime. A typical oblique motion of a sphere, from the present experiments is depicted in Fig.3.4 a. This regime was also observed experimentally by VB, HW and by some preliminary experiments of JDB. Not many data points or test cases were considered within this regime in the present work owing to the fact that, this regime has already been established in great detail. The primary goal here was to verify this regime and check if the regime is reproducible. For the cases investigated, the angle with respect to the vertical agreed with the earlier works. The angle with respect to vertical is computed from the dot product of a vector along the vertical line and a vector along the falling path of the sphere. For the steady oblique regime, the vector of the falling path is obtained by taking the first and last position. In the case when the sphere oscillates, the vector of the falling path varies at every instant and hence the angle with vertical also varies with time and hence the mean value is computed.

Table 3.3 shows the comparison of the angles obtained in other works and are compared to the present work. The table collectively represents the ranges of angle for the steady oblique regime and oblique oscillating regime (explained below).

It is also important to note that, few of the results in the present work also show an oblique curved path (Fig.3.4 b). Some low angle predictions in the present work (Table 3.3) are due to the curvature of the path. Similar curved trajectories were also observed by VB in their experiments. VB attributes it to the possibility of inhomogeneities in the sphere and its associated improper mass distribution for the reason for such curved paths.

Table 3.3: Angle with respect to vertical for oblique regime (for steady oblique and oblique oscillating)

| Research Article | Angle ($^{\circ}$) |
|------------------|----------------------|
| Present work | 2.79 to 7.4 |
| HW | ≈ 3.5 to 7.5 |
| ZD | 4 to 6 |
| AM | 2.6 to 7.3 |

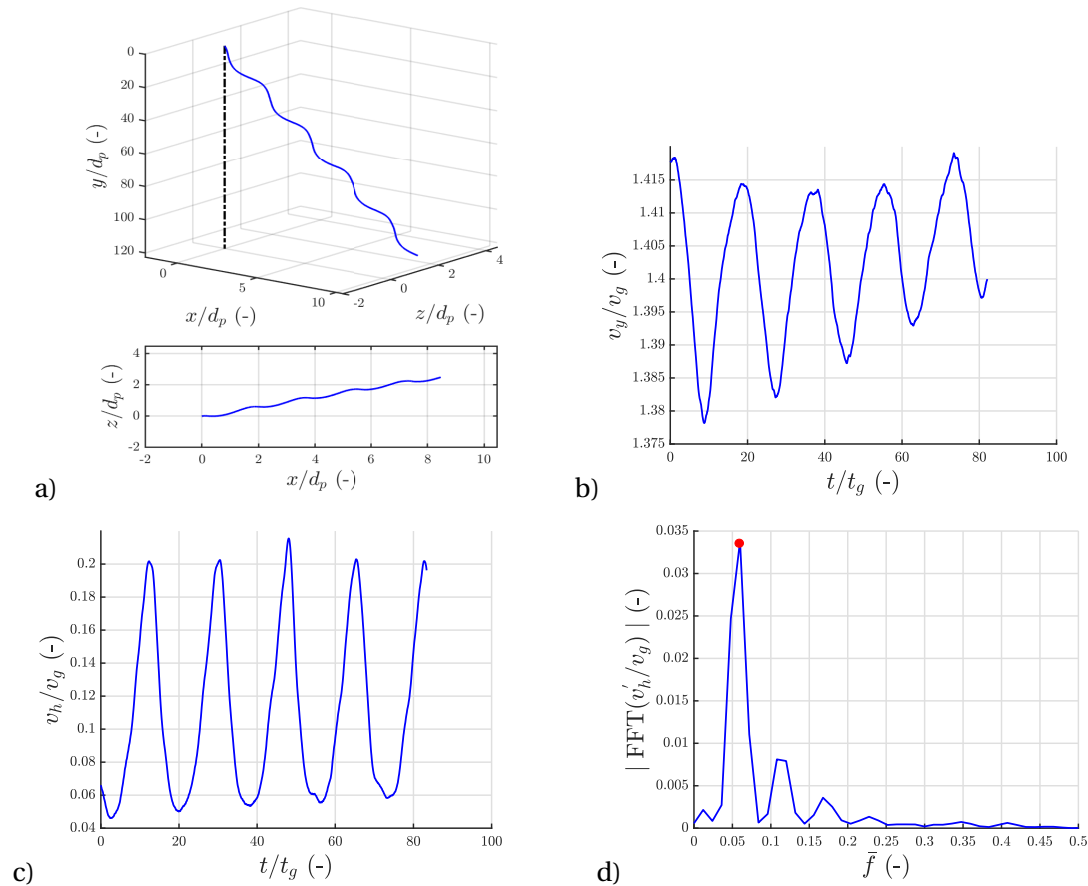


Figure 3.5: a) Oblique Oscillating trajectory for $\bar{\rho} = 1.121$ and $Ga = 184.4$ falling at an angle of 4.57° with respect to the vertical with a mean vertical velocity of 0.086 m/s and mean horizontal velocity of 0.0072 m/s,
b) Temporal variation of vertical velocity (amplitude of oscillation $\approx 0.015 v_g$),
c) Temporal variation of horizontal velocity (amplitude of oscillation $\approx 0.075 v_g$),
d) Spectrum of the fluctuation of horizontal velocity (with the red dot indicating the dominant peak at 0.059)

The Oblique Oscillating Regime

Moving along Line FL in Fig.3.1, above a critical Ga , which according to ZD ≈ 180 when (in this case where $\bar{\rho} \approx 1.12$), the planar wake undergoes a Hopf bifurcation and the oblique trajectory of the sphere begins to oscillate, leading to a new regime known as the '**Oblique Oscillating**' regime. The trajectory of such regime is depicted in Fig.3.5 a and the time evolution of the vertical and horizontal velocity are shown in Fig.3.5 b,c with the amplitude

of the velocity oscillation being $\approx 0.015v_g$ and $0.075v_g$ respectively. Similar to the steady oblique cases, a curved oscillating regime was also observed in a few cases.

The critical Ga for the onset of this regime corresponds to a $Re \approx 240$, which is well below the critical Re for the onset of shedding in the fixed sphere, which is ≈ 275 ([16]). This clearly indicates that the effect of additional degree of freedom of the sphere is evident in the quicker transition behaviour. The above explanation is adapted from the discussion of AM for a similar transition behaviour. The frequency of shedding is computed from the dominant peak in the frequency spectrum (Fig.3.5 d). We can clearly see a peak at \bar{f} or $St = 0.059$. It is important to be noted that, this St is much smaller than that observed for a fixed sphere which has also undergone a Hopf-bifurcation. This is the reason why this regime is also called ‘low frequency oblique oscillating’ regime by ZD. For the oblique oscillating regime, in the present work, the observed St is in the range of 0.046 to 0.059 which agrees very well with the range of 0.045 to 0.068 reported by JDB. So, at this, point, the present methodology agrees well with older works, where there is no disagreement between different earlier works. This serves as a good verification for the present results.

Chaotic Regime and the Hidden Bi-stable Zone

Moving along Line FL in Fig.3.1, for a $Ga \approx 200$, ZD predicts the transition to chaos. From the present results, we agree with ZD as a ‘**chaotic regime**’ is also observed for various Ga considered from 205 to 243 (depicted in Fig.3.10). In the present work, the chaotic regime was observed up to the highest Ga employed, which can also be seen in the updated $Ga - \bar{\rho}$ map of the present study (depicted in Fig.3.10). One such case of a chaotic regime is depicted in Fig.3.6. The path taken in the chaotic regime is not repeatable, but contains intermittent imprints of the stable regimes that are in the Ga limits close to it in the $Ga - \bar{\rho}$ parameter space. This is clear in the spectrum of the chaotic regime (Fig.3.6 c), where we see a dominant peak at $\bar{f} = 0.169$ and also a few low frequency peaks close to it. This was also unequivocally observed from numerical simulations of JDB, ZD and from the experiments of VB. This is also observed in the spectrum for fixed spheres where St of 0.045 and 0.167 was observed at a Re of 500 ([20]). At this point this also provides a hint that, in the close Ga limits, there is a possibility for a high-frequency oscillating regime (of $St \approx 0.1 - 0.16$). This brings us to the discussion of the next regime that is present within the chaotic domain.

Moving along Line FL in Fig.3.1, from $Ga \approx 250$ to 300, ZD reports a regime strictly vertical (2D) with high frequency oscillations ($St \approx 0.1 - 0.15$), called the ‘**Vertical Oscillating regime**’. For $\bar{\rho}$ slightly greater than 1, ZD has probed 4 points and in that 2 are characterized as bi-stable and 2 as stable vertical oscillating cases. By the term ‘**Bi-stable**’, it is meant that the sphere keeps intermittently switching between the chaotic regime and the vertical oscillating regime. It is important to note that this regime hasn’t been observed experimentally up till now. This is also not found in the older work by JDB, where a similar bi-stable regime was characterized for rising cases ($\bar{\rho} < 1$). However in their updated map (Fig.3.1), this zone is very clearly presented and the distinction between the bi-stable and fully stable paths are made. Owing to this disagreement and also owing to the fact that this regime wasn’t studied experimentally earlier, it was decided to probe this regime in great detail. Almost 50 different Ga were investigated along line FL from 240 to 300 and a clear cloud of the above vertical oscillating type regimes were observed in the present work. This

is evident from our updated map in Fig.3.10.

As mentioned earlier, pure vertical trajectories are not possible to obtain experimentally, a slight drift was present making it deviate from the strict vertical nature mentioned by ZD. Due to the drift, the above regime will be referred to (in this work as), '**high-frequency oscillating**' regime although all the characteristics are the same as the vertical oscillating regime mentioned by ZD. The typical trajectory of the high frequency oscillating regime is in Fig.3.7 a along with the temporal evolution of horizontal velocities and the spectra in Fig.3.7 b,c. A clear peak is seen at $St = 0.154$. It is interesting to note that, almost same St is observed post the Hopf bifurcation for a fixed sphere. But this regime was not observed to be consistent, but coexisting with the chaotic domain. Out of the 50 different measurement points in the $Ga - \bar{\rho}$ map, close to 30 were observed to be in the chaotic regime and 20 were observed to be perfectly high-frequency oscillating (depicted in Fig.3.10). In some cases, a smooth transition from chaos to the high frequency oscillating regime was seen (Fig.3.8 a)

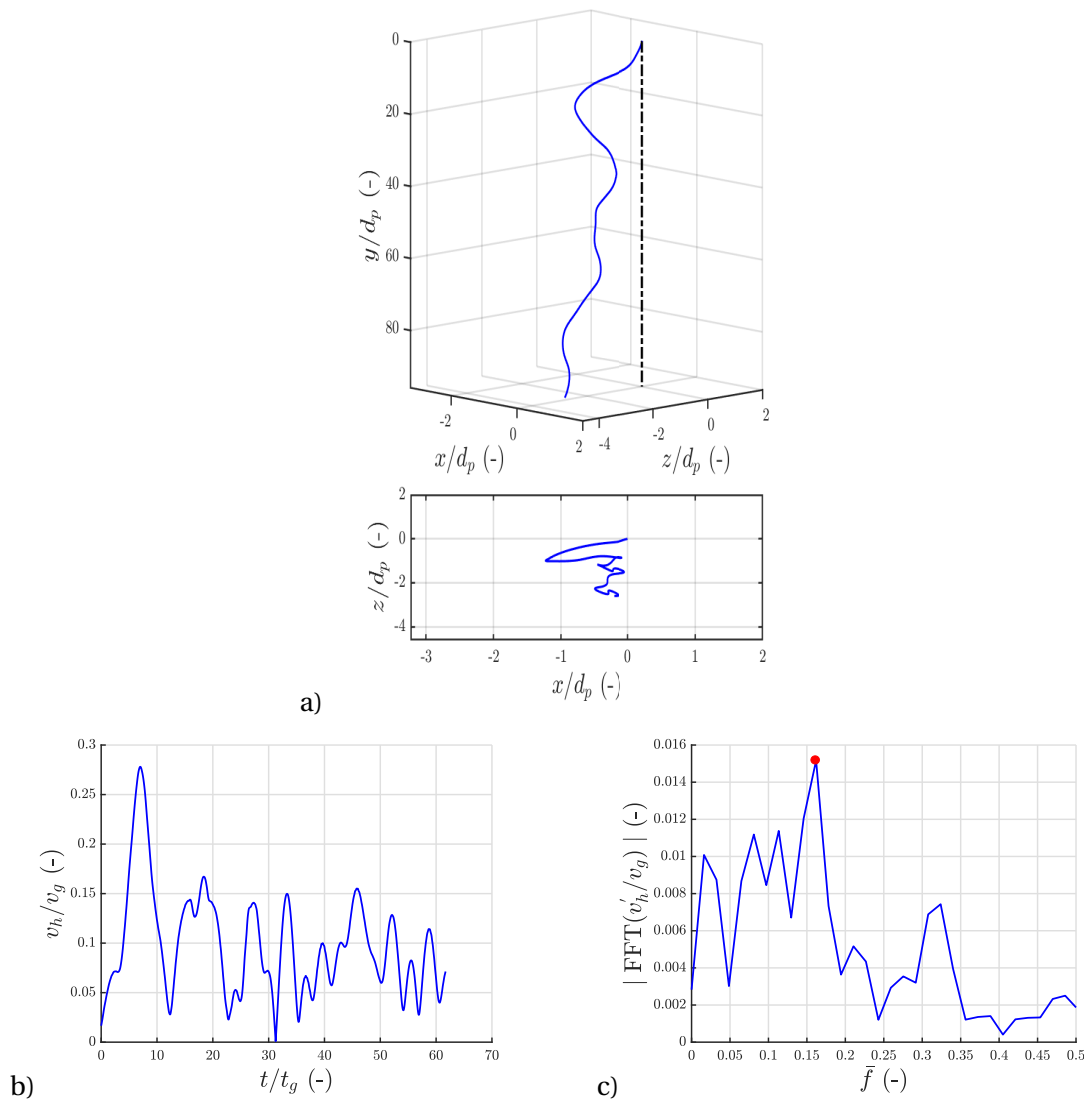


Figure 3.6: a) Oblique Oscillating trajectory for $\bar{\rho} = 1.121$ and $Ga = 283.81$, b) Temporal variation of horizontal velocity, c) Spectrum of the fluctuation of horizontal velocity (with the red dot indicating the dominant peak at 0.161)

and also in some cases a clear irregular unstable high frequency oscillations were observed (Fig.3.8 b). This is an indication of the bi-stable nature.

At this point we would like to establish the following comments:

1. There is a possibility that after a much longer distance of travel by the sphere, only one regime may exist making it purely chaotic or purely high-frequency oscillating.
2. As we can see from the transition between both the regimes in Fig.3.8 a and Fig.3.8 b, it may very well be the case reported by ZD and JDB where the sphere intermittently switches between high-frequency oscillating and a chaotic regime. Hence, in this case, the connotation ‘bi-stable’ will make complete sense.
3. To draw a conclusion from the extensive set of 50 data points, since we see that the

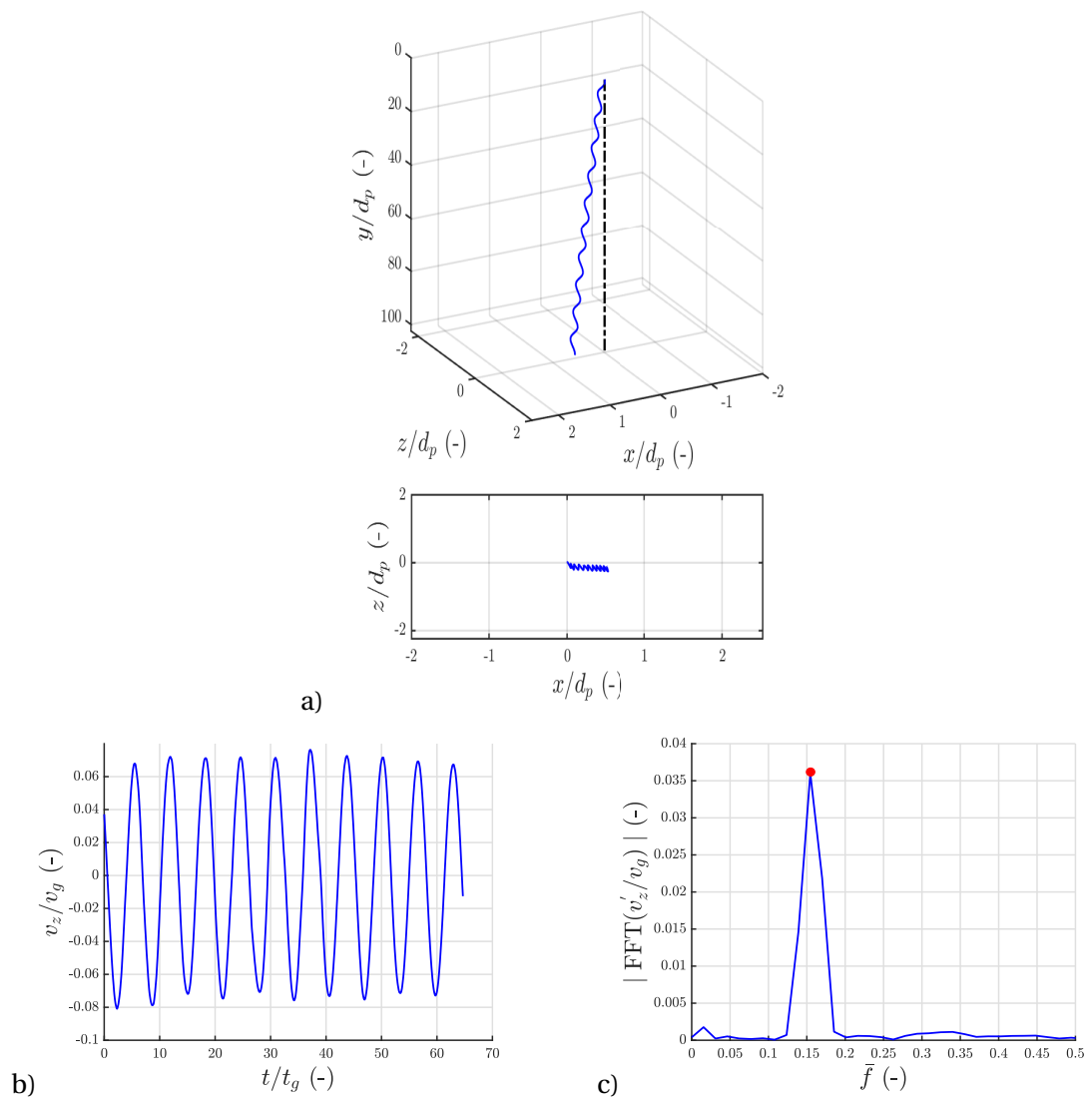


Figure 3.7: a) High frequency Oscillating trajectory for $\bar{\rho} = 1.13$ and $Ga = 259.92$, b) Temporal variation of z-velocity, c) Spectrum of the fluctuation of z-velocity (with the red dot indicating the dominant peak at 0.154)

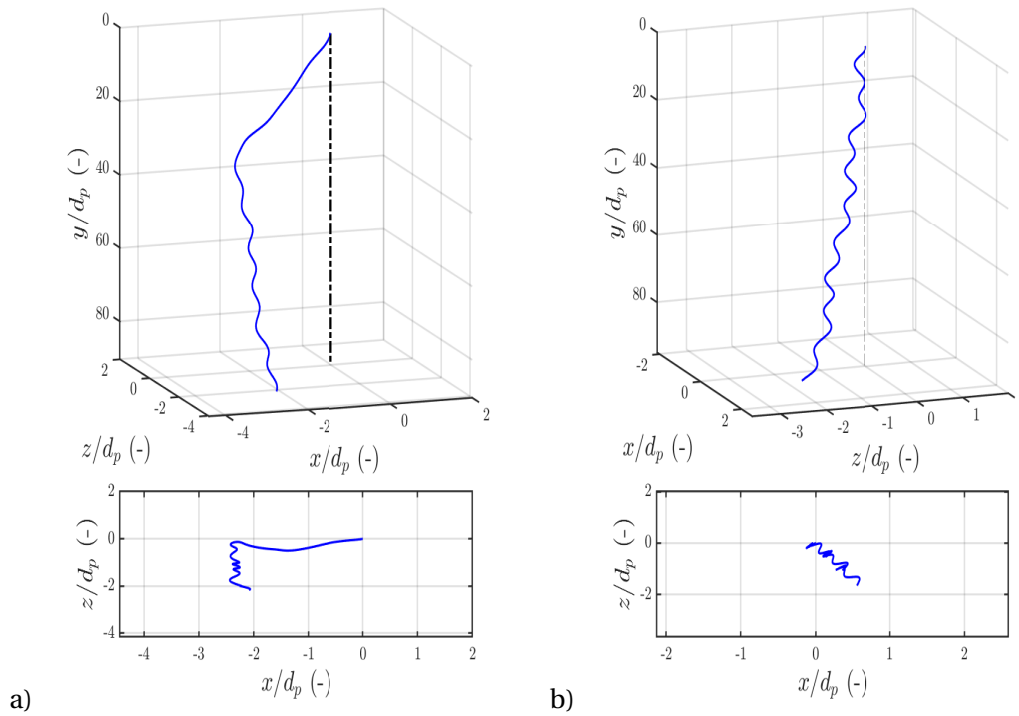


Figure 3.8: a) Transition from a chaotic drifting trajectory to high frequency oscillating trajectory for $\bar{\rho} = 1.11$ and $Ga = 278.95$ b) Irregular high frequency oscillating trajectory for $\bar{\rho} = 1.11$ and $Ga = 277.49$

high frequency oscillating regime is spread out in the entire range of Ga from 240 to 300 along with the chaotic regime, we choose to pursue the fact that this regime is bi-stable.

ZD reports that for $Ga \approx 262$ and greater, the regime is fully stable vertical oscillating regime. We tend to disagree at this point, since, from the present results, we see a clear co-existence of both the regimes from Fig.3.10. For $Ga > 300$, in the present work the chaotic regime was observed consistently and we agree with ZD. So, the results of ZD are consistent with the present results except when characterizing the bi-stability for the high frequency oscillating or vertical oscillating regime from $250 < Ga < 300$.

The three components of velocity (v_x , v_y and v_z) are plotted in form of a velocity diagram in Fig.3.9 for all the regimes observed when moving along line FL1. This will aid in better understanding of the transition to chaos. It is clear from the plot that with increase in Ga , the area occupied in the 3D space increases. With the steady vertical regime appearing almost as a dot (owing to negligible horizontal excursions) and the chaotic regime occupying the largest area with greater excursions. From the steady vertical regime to the chaotic regime, the magnitude of excursions increase, depicting that the solid-fluid coupling becoming more intense and the transition to chaos is through increase in investment of energy in the lateral direction in the form of horizontal excursions.

The updated $Ga - \bar{\rho}$ map from the present study along line FL1 is presented in Fig.3.10. The points represent the results of the present measurement campaign and the vertical lines are adapted from ZD using which the demarcation of thresholds of different regimes is shown.

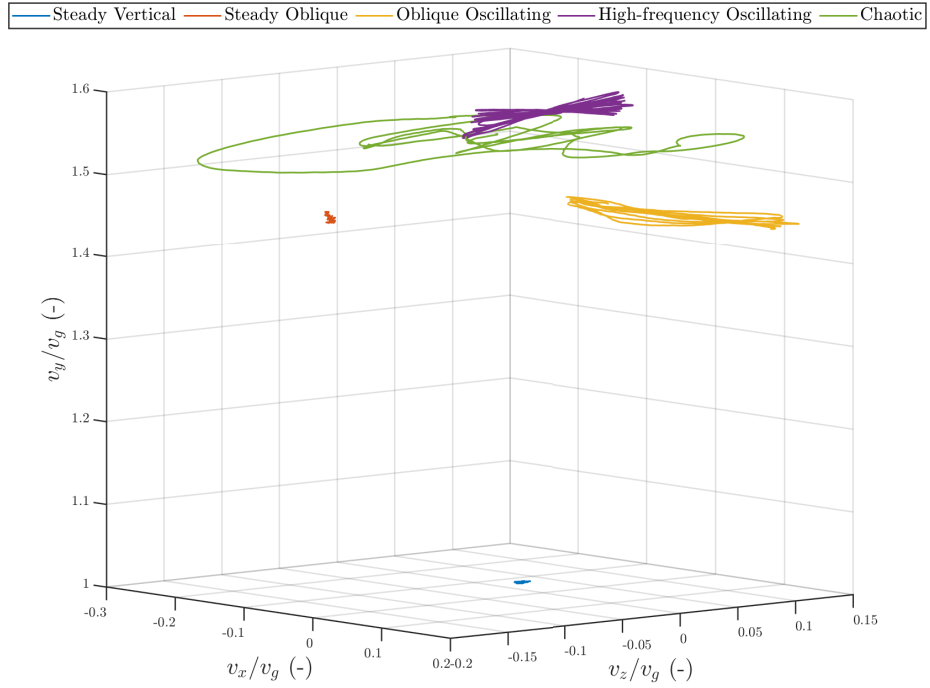


Figure 3.9: 3D velocity plot for all the regimes along line FL1, with reach regime corresponding to a Ga and $\bar{\rho}$ as follows: Steady Vertical - $Ga = 110.14$ and $\bar{\rho} = 1.156$, Steady Oblique - $Ga = 166.56$ and $\bar{\rho} = 1.121$, Oblique Oscillating - $Ga = 184.4$ and $\bar{\rho} = 1.121$, High frequency oscillating - $Ga = 259.92$ and $\bar{\rho} = 1.13$, Chaotic - $Ga = 283.81$ and $\bar{\rho} = 1.121$.

The map serves as a direct comparison between the regimes observed in the present study

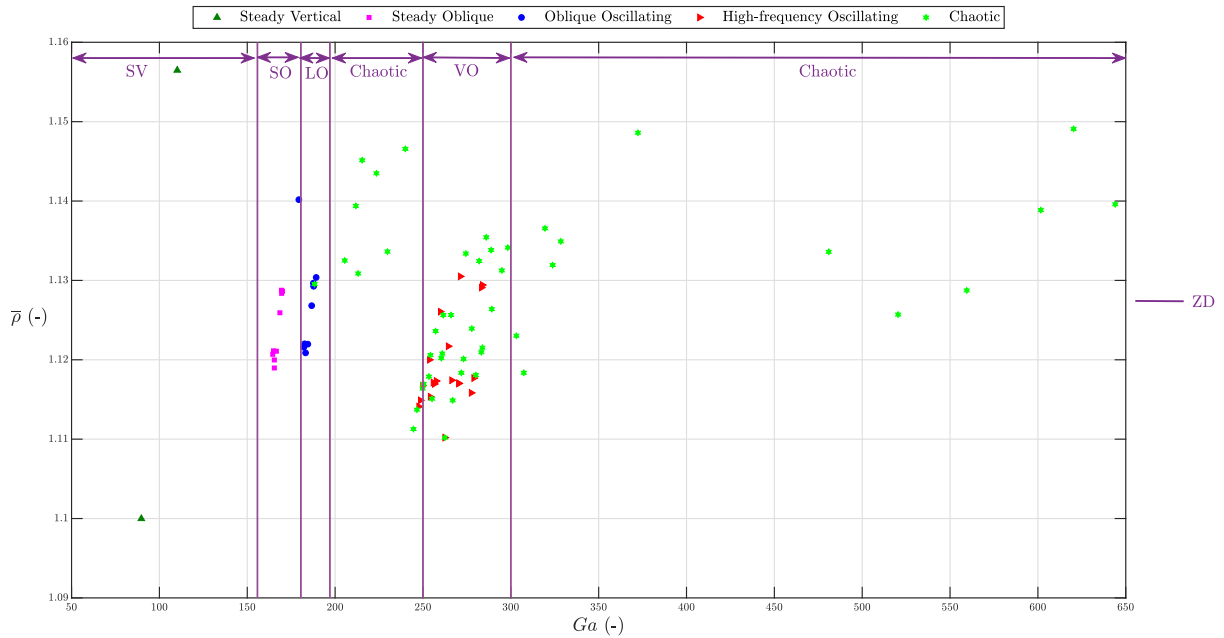


Figure 3.10: $Ga - \bar{\rho}$ map updated along line FL with the results of the present study. The map represents a direct comparison with map of ZD. Vertical lines represent the thresholds of different regimes from the ZD map, with annotations, SV-steady vertical, SO-steady oblique, LO-low-frequency oblique oscillating, VO-vertical oscillating

against the regimes reported by ZD. The map with the uncertainties included for every case is provided in Appendix D (Fig.D.2).

3.4.2. Results high density cases ($\bar{\rho} \approx 3.19$ and 3.9)

The Steady Oblique Regime

Even for the dense cases, the steady oblique regime has no disagreement between different works. Maps of JDB and ZD have no difference in this regime and also experiments of VB and HW agree well. Hence, in the present work, it was decided not to probe this regime in great detail. However, for the two measurement points on the updated map (shown as pink squares in Fig.3.13), a neat steady oblique regime was observed.

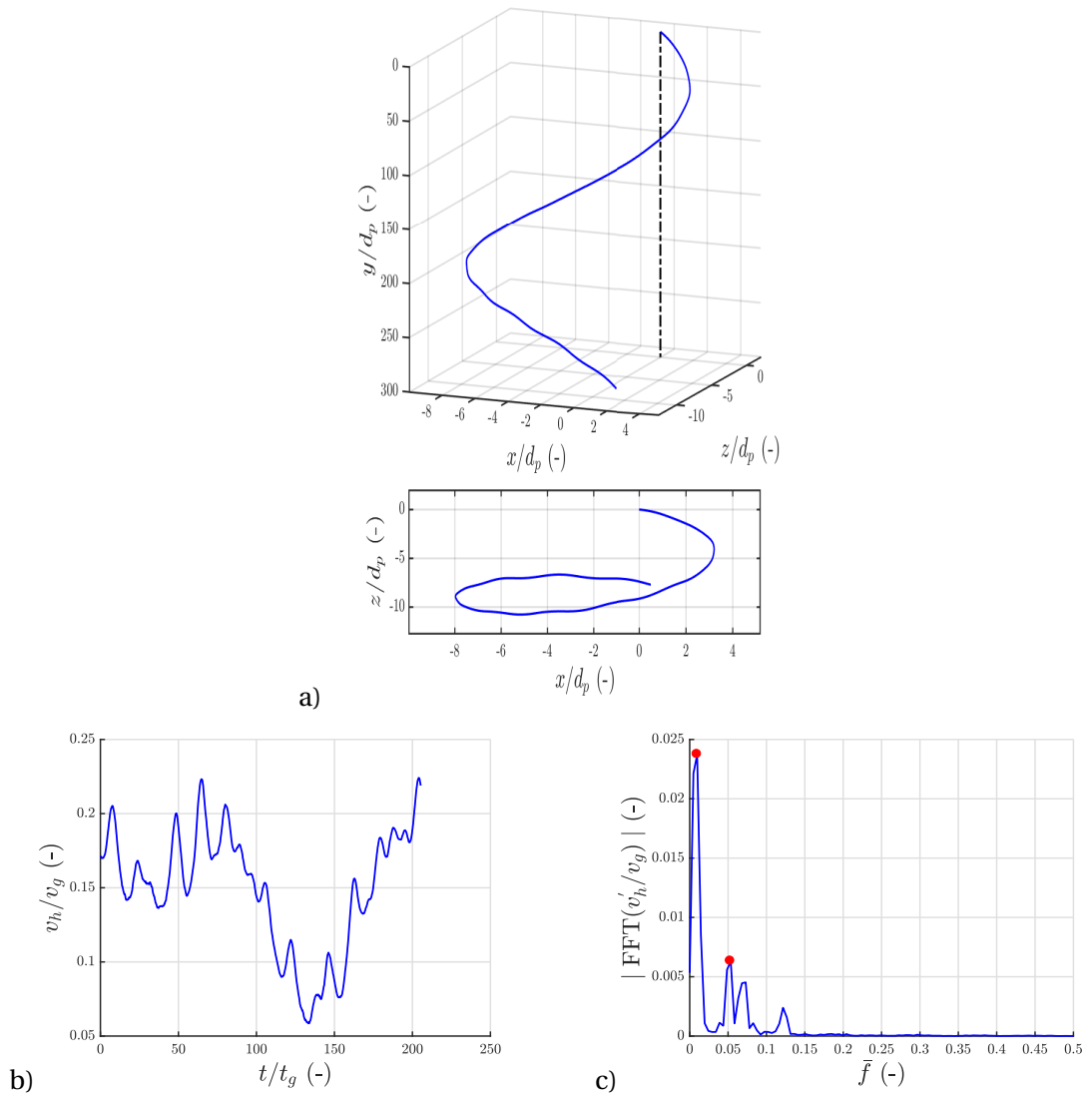


Figure 3.11: a) Helical/rotating trajectory for $\bar{\rho} = 3.19$ and $Ga = 208.4$ with half pitch and diameter of the helix is $\approx 214d_p$ and $12d_p$ respectively, b) Temporal variation of horizontal velocity, c) Spectrum of the fluctuation of horizontal velocity (dominant peaks indicated by red dots)

The Helical/Rotating Regime

On moving along line FH1 and FH2, from the works of ZD, we would expect a high-frequency oblique oscillating regime for $Ga > 195$. This was, however, not the case in the present work.

We observe a **'helical/rotating'** regime which is oblique with low-frequency oscillations superimposed on the rotation of the sphere in 3D space. A typical trajectory of the regime is depicted in Fig.3.11 a where the half pitch and diameter of the helix is $\approx 214d_p$ and $12d_p$ respectively. In the spectrum depicted in Fig.3.11 c a dominant peak can be seen at $\bar{f} = 0.0097$, which corresponds to slow rotation of the sphere and the second peak can be seen at $\bar{f} = 0.053$, which corresponds to the low-frequency oscillations that are superimposed on the rotation. Since it is not a perfect helix and hence is given the name 'helical/rotating'.

This regime was also reported by ZD for $Ga \gtrsim 212$ and they characterized it as bi-stable regime. In the present work, the measurements were repeated and $Ga - \bar{\rho}$ map (shown in Fig.3.13) was thoroughly tested in the region for many cases and we always observe a fully stable rotating/helical regime for the cases considered (from $Ga = 205$ to $Ga = 231$). For many measurement points in the range of $Ga = 205$ to 212 , we never observed any signs of high-frequency oscillations and hence we disagree with the works of ZD and JDB. Even the experimental work of VB, never reported the high frequency oblique oscillating regime. VB reported a steady oblique regime and directly a helical/rotating regime, thereby agreeing with the present work. However, the helical/rotating regime was not pursued in great detail in the work of VB, but in the present work, it is the main focus and many measurement points are probed in the $Ga - \bar{\rho}$ map (Fig.3.13) to check bi-stability and characteristics of the regime with increase in Ga . The results from lines FH1 and FH2 agree well, thereby, increasing the confidence of the results reported in the present work. Moreover, this also proves that dense spheres ($\bar{\rho} > 2.5$ in general), take a route to transition that is different from the lower density counterparts ($\bar{\rho} < 2.5$), thereby substantiating the transition characteristics reported by ZD.

On increasing Ga , within the rotating/helical regime, some new characteristics that haven't been reported earlier were observed in the present study. For $Ga \gtrsim 222$ up till 231 , the pitch of the helix decreased ($\approx 240d_p$), to almost half of that observed for Ga between 205 and 215 (an example of such phenomenon is shown in Fig.3.12 a). The oscillations also become much more pronounced (depicted in Fig.3.12 b), and in some cases the path also shows slight deviations from the helical trend indicating the onset of chaos. For $Ga = 231$, for one case we observe a helical/rotating regime (Fig.3.12 c) and in another case it is chaotic, indicating that somewhere around this Ga the regime transits to fully chaotic (Fig.3.12 d). This is in excellent agreement with ZD, where they reported critical $Ga \approx 230$. For $Ga > 240$, for all the cases investigated, a chaotic regime was observed (depicted in Fig.3.13).

The updated $Ga - \bar{\rho}$ map along lines FH1 and FH2 is presented in Fig.3.13. The points represent the results of the present measurement campaign and the vertical lines are adapted from ZD using which the demarcation of thresholds of different regimes is shown. The map serves as a direct comparison between the regimes observed in the present study against the regimes reported by ZD. We clearly do not see any high-frequency oscillating regime in the region where it was observed by ZD. Also, P/R (planar or rotating) observed by ZD was a bi-stable regime, but with the points shown in the map, we observe a fully stable helical/rotating regime. The map with the uncertainties included for every case is provided in Appendix D (Fig.D.3).

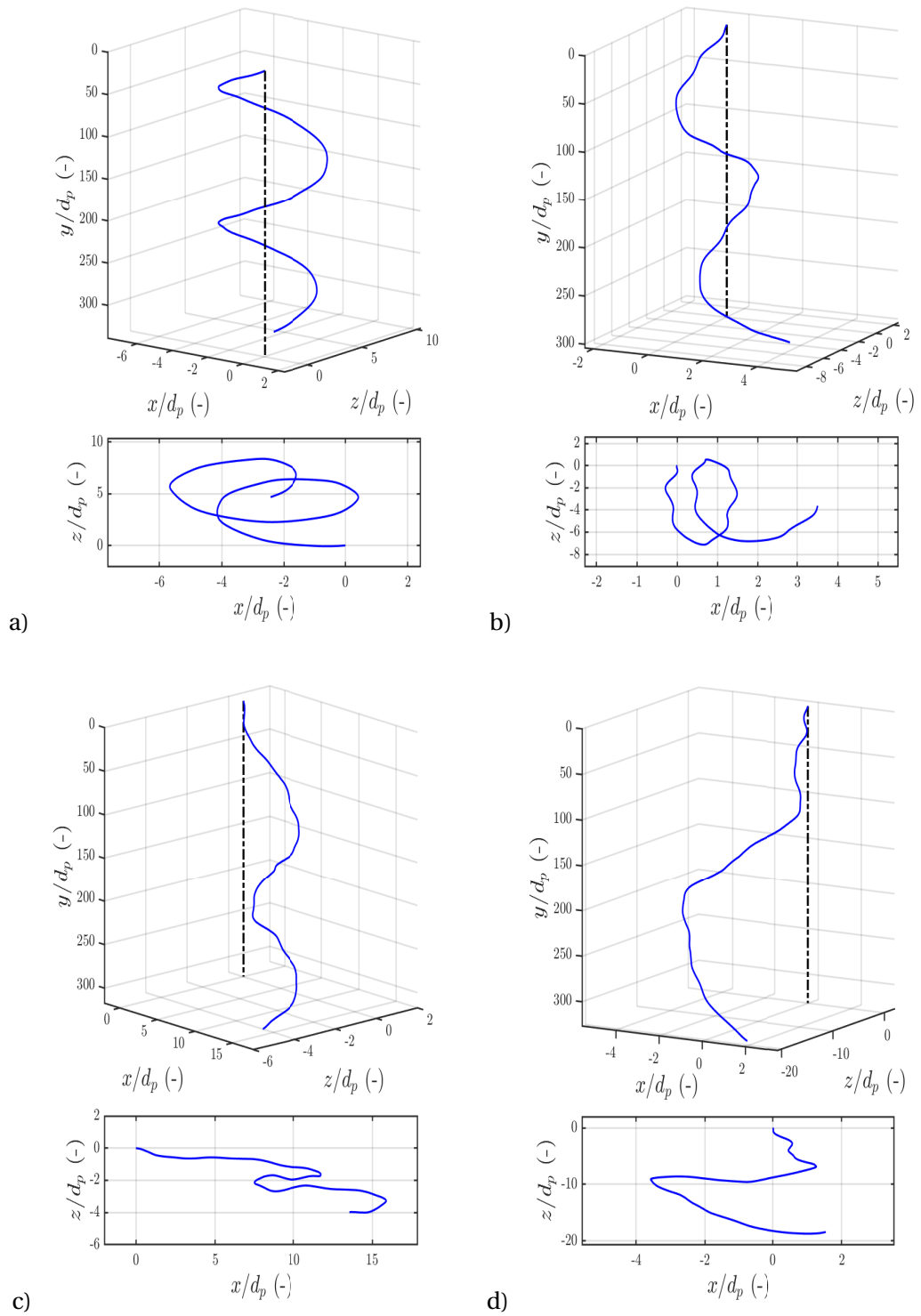


Figure 3.12: a) Helical/rotating trajectory with lower pitch for $\bar{\rho} = 3.88$ and $Ga = 225.58$, b) Helical/rotating trajectory with lower pitch and pronounced oscillations for $\bar{\rho} = 3.21$ and $Ga = 225.67$, c) Irregular Helical/rotating trajectory $\bar{\rho} = 3.21$ and $Ga = 231.17$, d) Irregular Helical/rotating trajectory $\bar{\rho} = 3.19$ and $Ga = 230.016$

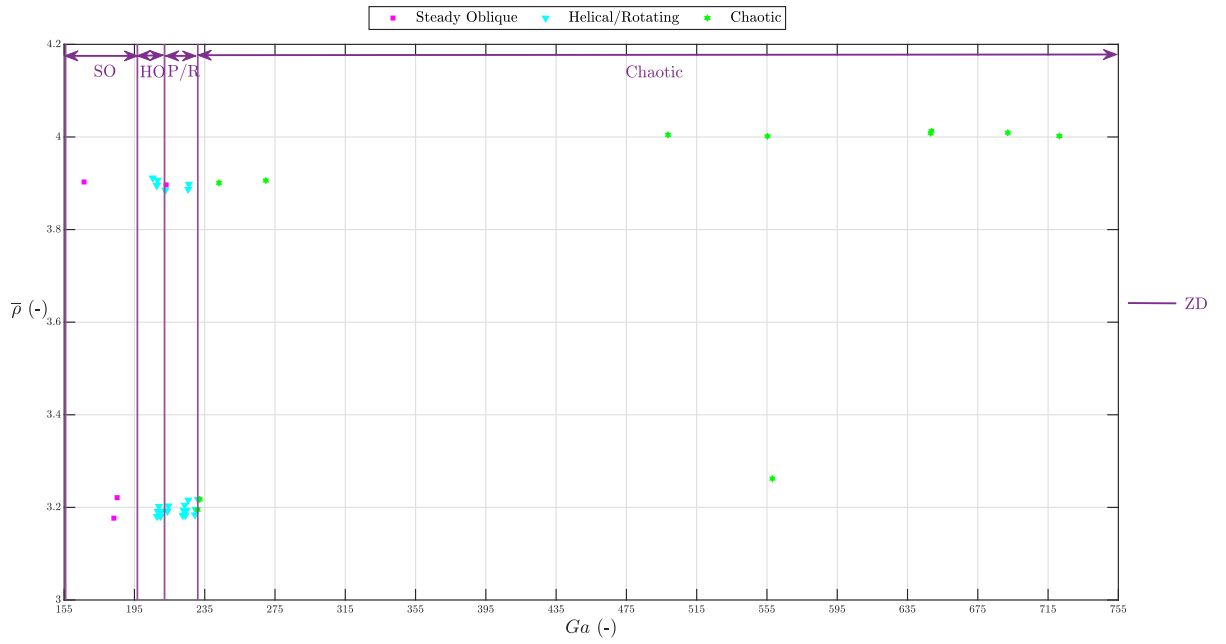


Figure 3.13: $Ga - \bar{\rho}$ map updated along line FH1 and FH2 with the results of the present study. The map represents a direct comparison with map of ZD. Vertical lines represent the thresholds of different regimes from the ZD map, with annotations, SO-steady oblique, HO-high-frequency oblique oscillating, P/R-Planar or rotating bistable

3.4.3. Drag Curve - Falling sphere

The variation of C_d with Re is shown in Fig.3.14. Although the trend follows that of a fixed sphere, the values are mostly lower, deviating from that of a fixed sphere. However, af-

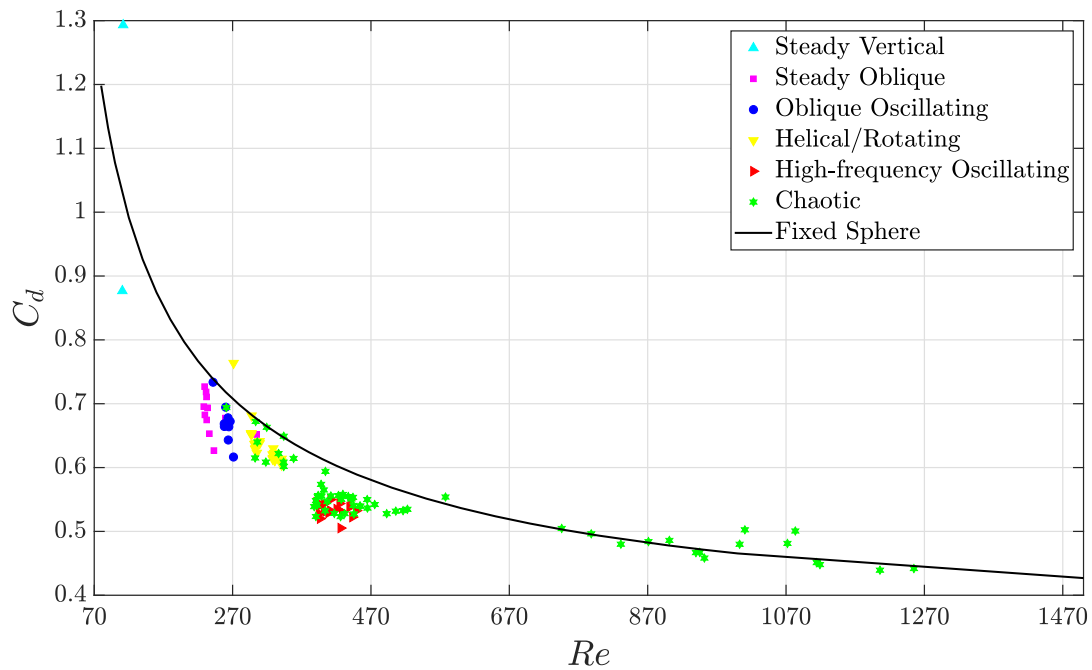


Figure 3.14: C_d plotted for various Re for falling cases (the fixed sphere curve is obtained from the relation proposed by Abraham (Eq1.11)[8])

ter performing a careful uncertainty analysis, the corresponding values of uncertainties explain the reason for the deviation observed. The main reason for the deviation is the uncertainty in diameter measurement followed by the uncertainty in mass. For a falling sphere, JDB observed the drag does not change much from fixed sphere, thereby having a good match. This trend is also supported by the results from HW. Inclusion of the uncertainty bars also gives us the same trend, thereby agreeing with the previous works. The plot with the uncertainties included for every case is provided in Appendix D (Fig.D.5).

3.4.4. Suppression of high frequency oscillations with sphere inertia

For the falling regime, a simple hypothesis was derived from the Morison's Equation (Eq.1.3). The aim was to test the validity of the result using experiments. The derivation is presented as follows:

Let us consider a scenario of a falling sphere in a still fluid (similar to one depicted in Fig.1.2). But here, we assume that the transience is still present and the sphere makes low amplitude oscillations as it falls. This would lead to retaining all the terms, including the added mass term from Eq.1.3. Substituting the expression for the added mass of a sphere ($\frac{1}{2}\rho_f V_p$) and taking the transient terms to one side, Eq.1.3 reduces to,

$$\left(\rho_p + \frac{1}{2}\rho_f\right)V_p \frac{du_{p,i}}{dt} \approx (\rho_p - \rho_f)V_p g_i - \left(\frac{1}{2}C_{ij}A_{fs}\rho_f |\underline{u}_p| u_{p,j}\right) \quad (3.1)$$

The above equation along x direction will give us,

$$\left(\rho_p + \frac{1}{2}\rho_f\right)V_p \frac{dv_x}{dt} \approx -\left(\frac{1}{2}C_d A_{fs}\rho_f |\underline{u}_p| v_x\right)$$

In the above equation, F_L is fluctuating lift force exerted by the fluid due to the shedding of the wake. Making an assumption that $|\underline{u}_p| \approx v_y$ (vertical velocity larger than the smaller horizontal velocity fluctuations), the above equation becomes,

$$\frac{1}{6}\left(\rho_p + \frac{1}{2}\rho_f\right)\pi d_p^3 \frac{dv_x}{dt} \approx -\left(\frac{1}{8}C_d \pi d_p^2 \rho_f v_x v_y\right) + F_L \quad (3.2)$$

In order to obtain an expression for v_y , we can use the vertical force balance (along y). The oscillations are dominant in the horizontal directions and hence we can assume that the sphere has reached the terminal settling velocity. Hence in Eq.3.1 the transient terms can be neglected and the resulting equation is

$$(\rho_p - \rho_f)V_p g \approx \frac{1}{2}C_d A_{fs}\rho_f v_y^2$$

Simplifying the above equation and taking v_y to one side and all other terms on the other side, yields the following expression for v_y .

$$v_y \approx \sqrt{\frac{4(\bar{\rho} - 1)gd_p}{3C_d}} \quad (3.3)$$

Substituting the expression for v_y from the above equation (Eq.3.3) into Eq.3.2, we get,

$$\begin{aligned} \left(\bar{\rho} + \frac{1}{2}\right)d_p \frac{dv_x}{dt} &\approx -\sqrt{\left(\frac{3}{4}C_d(\bar{\rho} - 1)gd_p\right)}v_x + \frac{6}{\pi d_p^2 \rho_f} F_L \\ \Rightarrow \frac{dv_x}{dt} &\approx -\frac{\sqrt{\left(\frac{3}{4}C_d(\bar{\rho} - 1)g\right)}}{\left(\bar{\rho} + \frac{1}{2}\right)\sqrt{d_p}}v_x + \frac{6}{\left(\rho_p + \frac{1}{2}\rho_f\right)\pi d_p^3} F_L \end{aligned} \quad (3.4)$$

It is clear from the above equation (Eq.3.4), that the coefficient of v_x is the inverse of the particle response time (dimensionally it is also a time scale). And hence we can define the particle response time (τ_p) by the following equation,

$$\tau_p \approx \frac{\left(\bar{\rho} + \frac{1}{2}\right)\sqrt{d_p}}{\left(\sqrt{\frac{3}{4}C_d(\bar{\rho} - 1)g}\right)} \quad (3.5)$$

We can assume the flow response time (τ_f), by the following expression,

$$\tau_f \approx \frac{d_p}{v_y} = \sqrt{\frac{3C_d d_p}{4(\bar{\rho} - 1)g}} \quad (3.6)$$

Now Stokes Number (\overline{St}), which is the ratio of τ_p and τ_f is obtain by diving Eq.3.5 and Eq.3.6 and is given by,

$$\overline{St} = \frac{\tau_p}{\tau_f} \approx \frac{4}{3C_d} \left(\bar{\rho} + \frac{1}{2}\right) \quad (3.7)$$

In the above equation, if C_d is kept constant and $\bar{\rho}$ is increased, we see that \overline{St} increases, which is intuitive because with greater inertia we expect the sphere to oscillate less or in

other words, the oscillations of the sphere should be suppressed as sphere's inertia is increased. In order to experimentally verify this C_d should be kept constant and one way of maintaining the C_d is by fixing Ga . This is clear from Eq.1.9. Hence the Ga was maintained almost constant (± 10) and was varied and 4 different cases were studied. The cases are depicted in Table 3.4

Table 3.4: Various $\bar{\rho}$ chosen for testing suppression of high frequency oscillations

| Case No. | Material | $\bar{\rho}$ | Ga |
|----------|-----------------|--------------|--------|
| 1 | Nylon | 1.12 | 559.5 |
| 2 | Silicon Nitride | 3.19 | 558.05 |
| 3 | Aluminium Oxide | 3.9 | 555.3 |
| 4 | Zirconium Oxide | 6 | 544.12 |

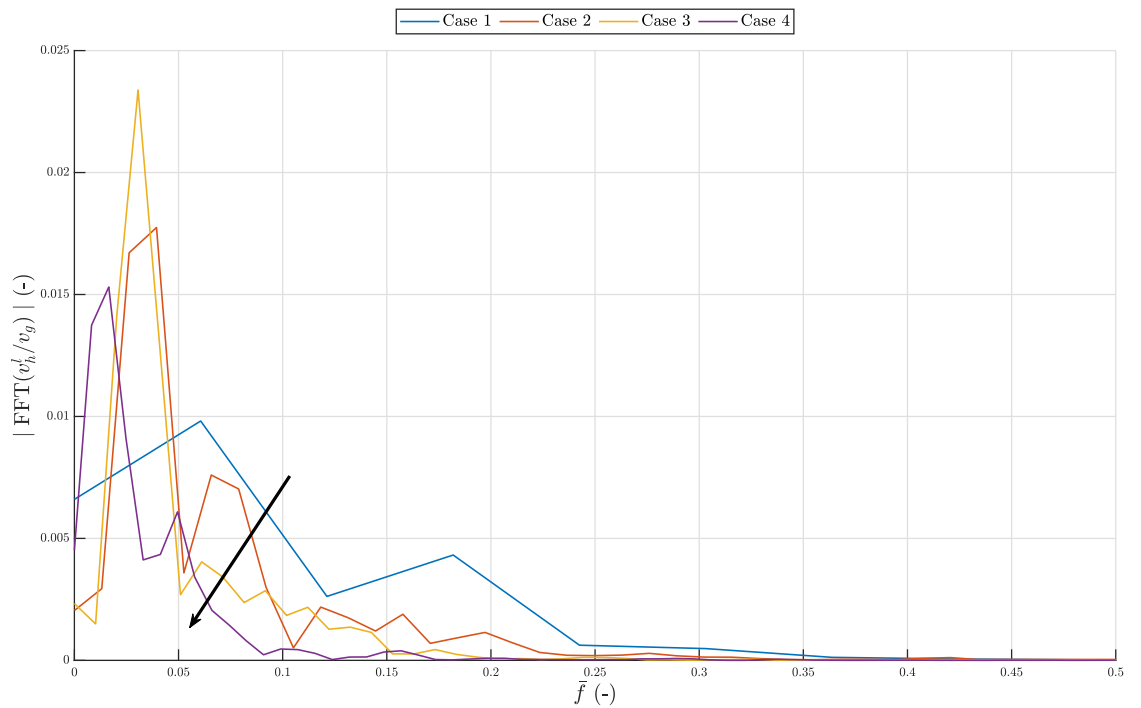


Figure 3.15: Spectrum of fluctuation of horizontal velocity for different density ratios in Table 3.4 ($\bar{\rho}$ increases in the direction of the arrow)

In Fig.3.15 the spectrum of the fluctuation of the horizontal velocity of the sphere normalized with gravitational velocity is plotted. From the figure, we can clearly see a reduction in the amplitude of fluctuations for higher frequency ranges. Hence, we do see a suppression of amplitudes for high-frequency as $\bar{\rho}$ is increased.

3.5. Rising Sphere

As mentioned in the beginning of this chapter, there are two reference maps for comparison for the rising sphere scenario. Various experimental data sets are covered along line R in Fig.3.1 and Fig.3.2.

Steady Oblique and Oblique Oscillating regime

These regimes were already established in the previous section. Previous works, even for the rising cases show no disagreement with each other in these regimes and hence this makes these two regimes a perfect validation test for the present work. Since, releasing the sphere from the bottom of the tank is much more sensitive to any form of disturbance that we may create in the fluid, this validation test is crucial to rule out the possible effect of the perturbations created due to the release mechanism. In the present study, both the regimes were tested thoroughly (shown in Fig.3.23) for rising cases and the results were consistent with the works for JDB, ZD and AM. For the steady oblique regime, for the cases investigated, the angle with respect to the vertical varied between 2.87° and 6.1° . A typical trajectory for a sphere rising for this regime is depicted in Fig.3.16. Similarly, for the oblique oscillating regime (Fig.3.17), the angle with respect to vertical varied between 2.75° and 6.17° . St ranges from 0.0496 to 0.0676, which again agrees with the previous works.

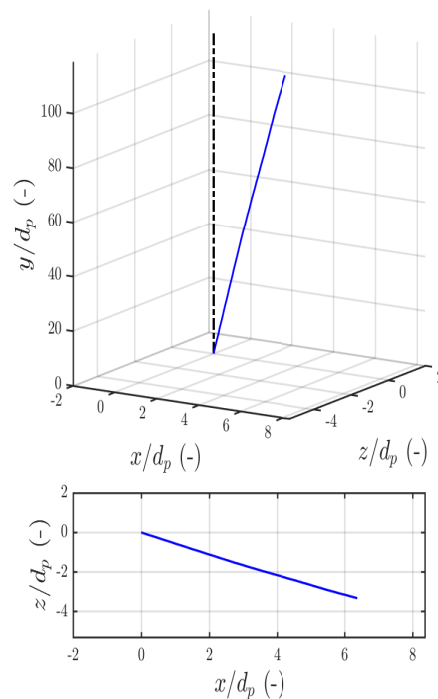


Figure 3.16: Trajectory of Steady oblique regime for $\bar{\rho} = 0.892$ and $Ga = 159.36$ falling at an angle of 3.47° with a mean vertical and horizontal velocity of 0.0775 and 0.004 m/s respectively

Zigzag Regime

Beyond the oblique oscillating regime, in the present work we observe a '**zigzag**' regime which is a characteristic of rising bubbles. From literature, the zigzag regime, is known to

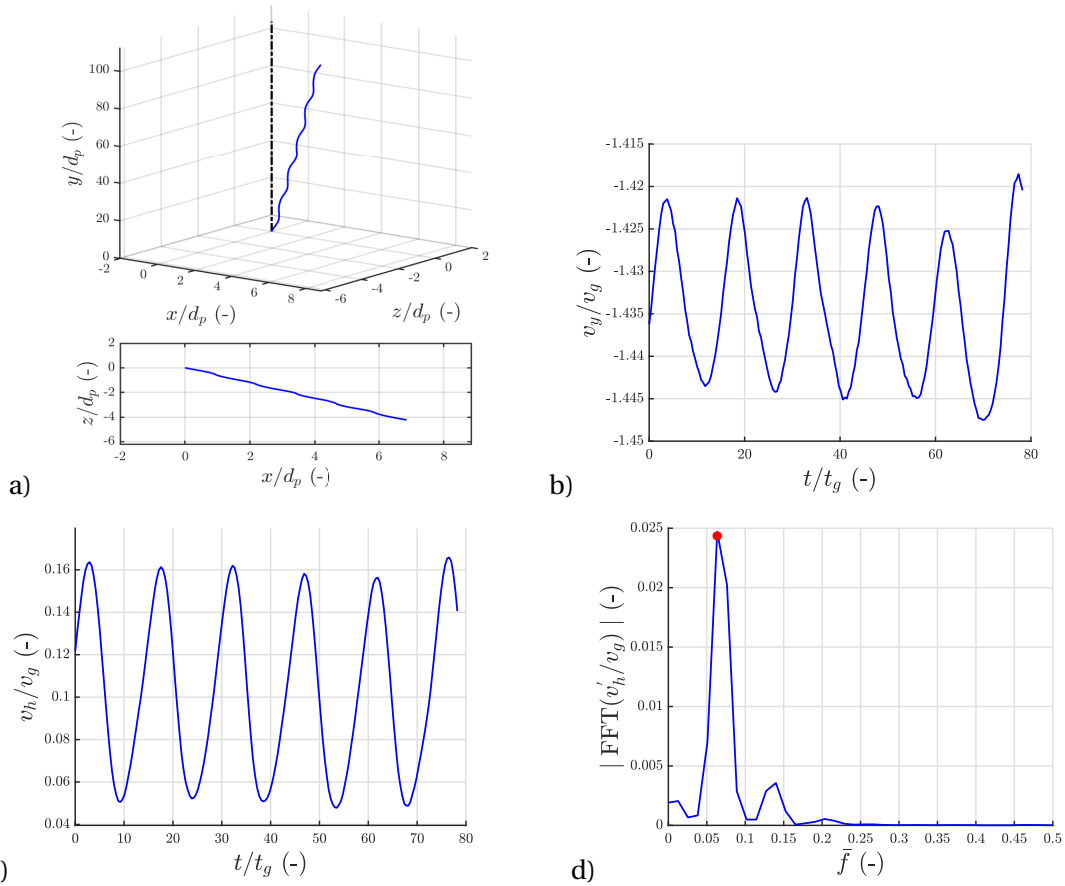


Figure 3.17: a) Oblique Oscillating trajectory for $\bar{\rho} = 0.867$ and $Ga = 179.54$ falling at an angle of 4.32° with respect to the vertical with a mean vertical velocity of 0.089 m/s and mean horizontal velocity of 0.0065 m/s,
 b) Temporal variation of vertical velocity (amplitude of oscillation $\approx 0.011 v_g$),
 c) Temporal variation of horizontal velocity (amplitude of oscillation $\approx 0.05 v_g$),
 d) Spectrum of the fluctuation of horizontal velocity (with the red dot indicating the dominant peak at 0.063)

be strictly vertical, but owing to the reasons mentioned earlier in this chapter, a drift is also seen in this regime, thereby deviating it from the vertical nature. Fig.3.18 a shows trajectory of a sphere rising in a zigzag pattern.

Beyond the oblique oscillating regime, different works disagree greatly with each other. JDB observed a zigzag regime upto $Ga = 215$. ZD reports a chaotic regime for Ga upto 250 and AM reports zigzag regime for Ga upto 250. Experimentally, HW, only observed zigzag motion for spheres with $\bar{\rho} < 0.36$ and VB never observed a proper zigzag regime. However, at this point we are in complete agreement with AM. Also, some outliers of chaotic motion are seen in this regime (depicted in the updated $Ga - \bar{\rho}$ map in Fig.3.23), which may be due to the presence of air voids in the sphere (can be seen from the histogram of density for the polypropylene spheres in Appendix E in Fig.E.1 b). The spread of the density values in Fig.E.1 b from the mean density is larger than the uncertainties determined for in $\bar{\rho}$ thereby bolstering the fact that air voids are present. The zigzag regime is very sensitive to the sphere homogeneity and this is evident from the fact that VB in their experiments only saw intersperses of zigzag motion and not a full-fledged zigzag as seen in the present results or from numerical simulations. Even in the present work, we observe a few improper

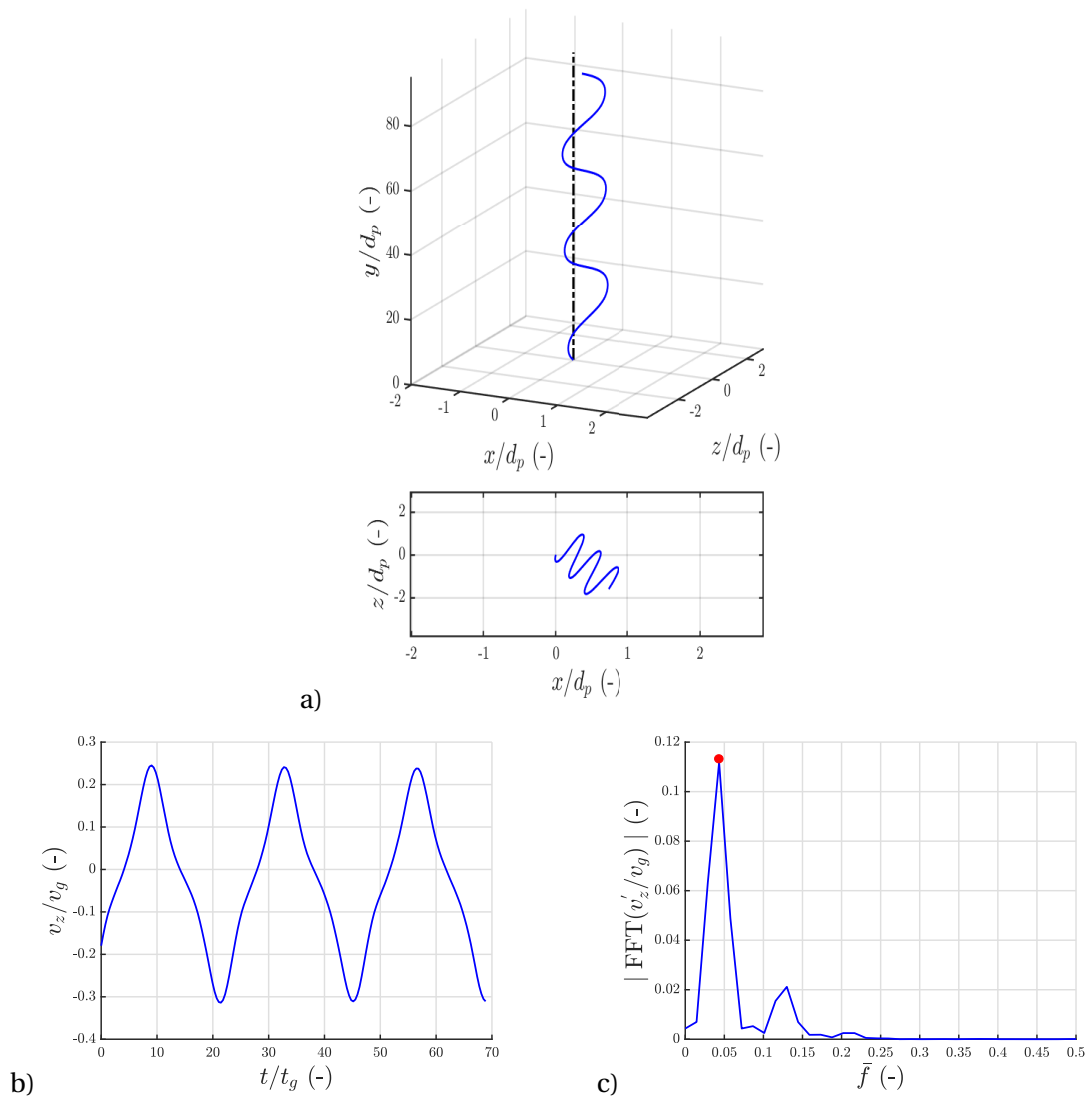


Figure 3.18: a) Zigzagging trajectory for $\bar{\rho} = 0.874$ and $Ga = 265.7$, b) Temporal variation of z-velocity, c) Spectrum of the fluctuation of z-velocity (with the red dot indicating the dominant peak at 0.043)

zigzags for a few cases investigated (shown in Fig.3.19 a,b). Also, JDB, numerically tested sphere with slight eccentricity in the centre of mass for the zigzag regime and ended up seeing the sphere take up a chaotic motion.

From the spectrum, depicted in Fig.3.18c the St is seen to be 0.043. The ranges of St observed in the present work is compared with the works of ZD and AM in Table 3.5. We see that the range slightly deviates in our case in the upper limit from ZD and JDB.

Chaotic Regime and Hidden bi-stable Regime

For $250 < Ga < 300$, we observe a 'high-frequency oscillating' regime similar to the ones observed for the low density falling sphere cases. Out of the 30 different experiments done in this region, 20 were chaotic and 10 were high frequency oscillating. By high-frequency, the St is estimated to be around 0.14-0.15. There were cases, where the St (≈ 0.08) was

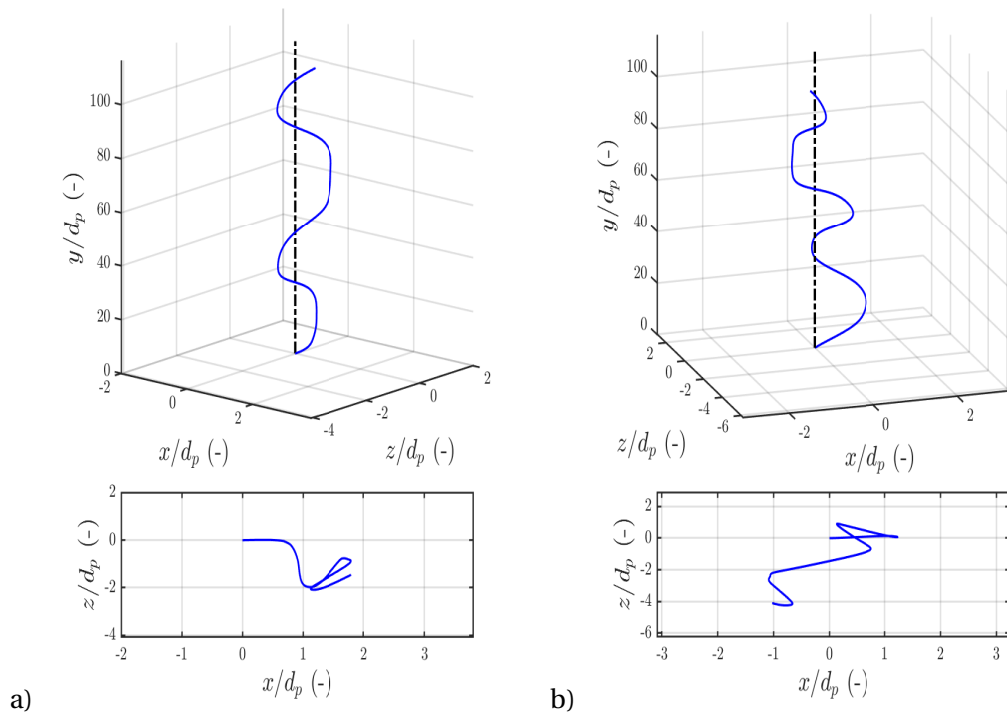


Figure 3.19: a) Trajectory of improper zigzagging for $\bar{\rho} = 0.864$ and $Ga = 202.42$ b) Trajectory of improper zigzagging for $\bar{\rho} = 0.882$ and $Ga = 198.98$

Table 3.5: St for Zigzag regime and comparison with previous works

| Research Article | St |
|------------------|-----------------|
| Present work | 0.0228 to 0.044 |
| ZD, JDB | 0.023 to 0.035 |
| AM | 0.016 to 0.036 |

lower than the expected St for high-frequency oscillating, but higher than that of oblique oscillating regime. It can be assumed that these cases are under transition and haven't reached the final regime yet, and may reach if tracked for a larger distance (this assumption will be substantiated in the following paragraph). This regime seems to coexist with the chaotic regime and hence is deemed bi-stable in the present work. A typical trajectory along with the velocity evolution and spectra given are depicted in Fig.3.20.

ZD characterized this regime as fully stable and strictly vertical(2D) and called it 'vertical oscillating' and AM characterized this regime as a fully stable high-frequency drifting regime (3D) and is called "ZZ2". AM reports the emergence of this regime after the sphere has travelled approximately $330d_p$, but in the present work, the sphere enters our field of view after approximately $187.5d_p$. This argument by AM seems convincing in the present case, as we also see a few stable regimes but with frequency of oscillation lower and we assume that it is still in the transition stage and may end up in the high frequency oscillating stage. In some cases we see a transition from chaos to high-frequency oscillating stage to chaos (Fig.3.21 a) and in some cases, we observe the chaotic regime having strong imprints

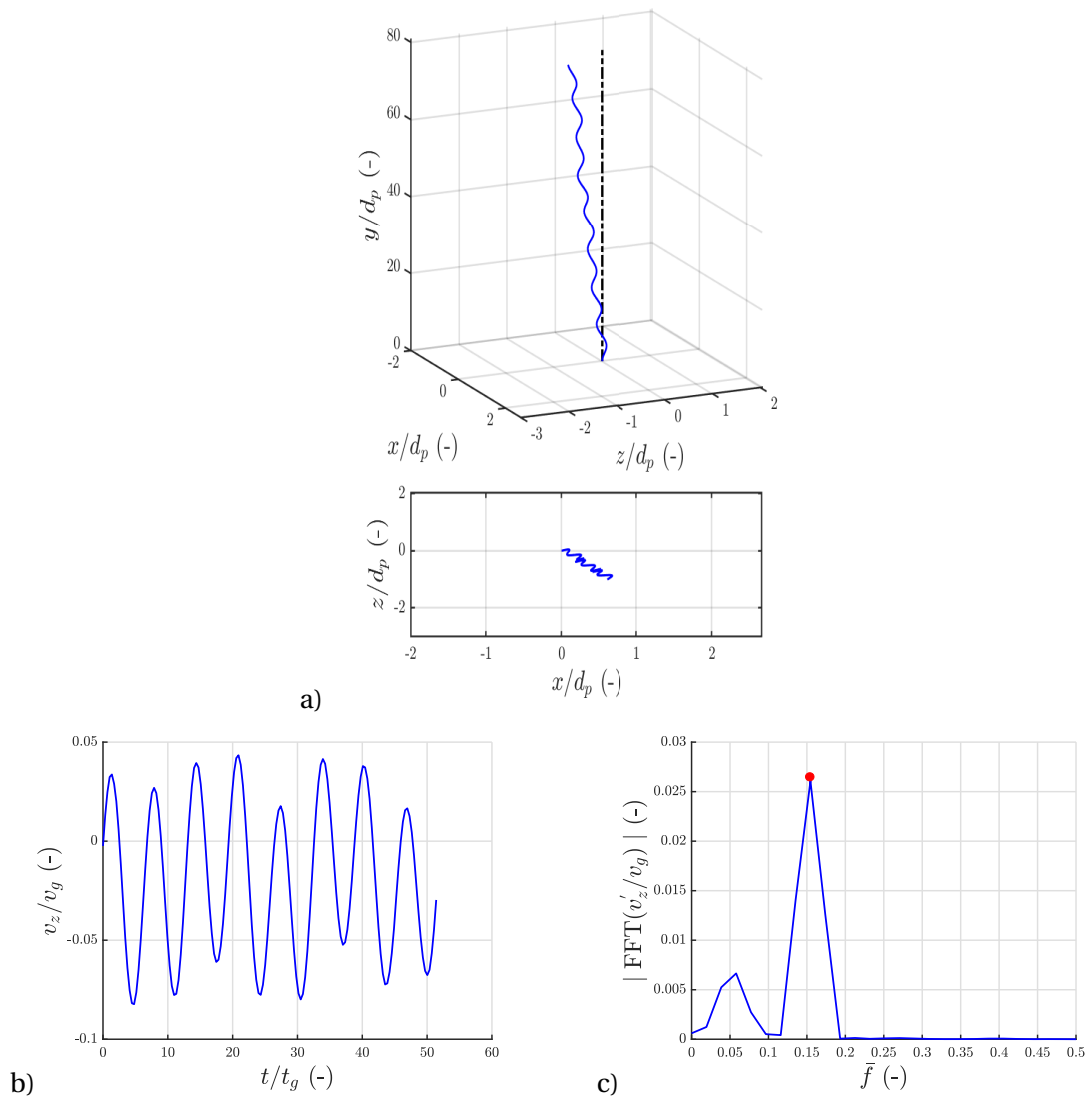


Figure 3.20: a) High frequency Oscillating trajectory for $\bar{\rho} = 0.879$ and $Ga = 279.11$, b) Temporal variation of z-velocity, c) Spectrum of the fluctuation of z-velocity (with the red dot indicating the dominant peak at 0.154)

of the high frequency oscillations (Fig.3.21 b), showing the bi-stability nature.

Also, in the experiments, since we are not able to attribute the drift to a physical effect or due to the large scale residual motions in the tank, we are not sure if we are to agree fully with ZD or AM. However, qualitatively, the regime is similar, except the fact that, we see a coexistence with chaos. Finally, moving along line R, for $Ga > 300$, mostly we observe a chaotic regime thereby agreeing with ZD and AM. This is shown in the updated $Ga - \bar{\rho}$ map in Fig.3.23. This map directly compares the present results with the results of AM and ZD, which are depicted as vertical lines indicating the thresholds demarcating different regimes. The map with the uncertainties included for every case is provided in Appendix D (Fig.D.4).

The three components of velocity (v_x , v_y and v_z) are plotted in form of a velocity diagram in Fig.3.22 for all the regimes observed when moving along line R. This plot correlates the area occupied in the 3D space due to lateral excursions of the sphere and the transition

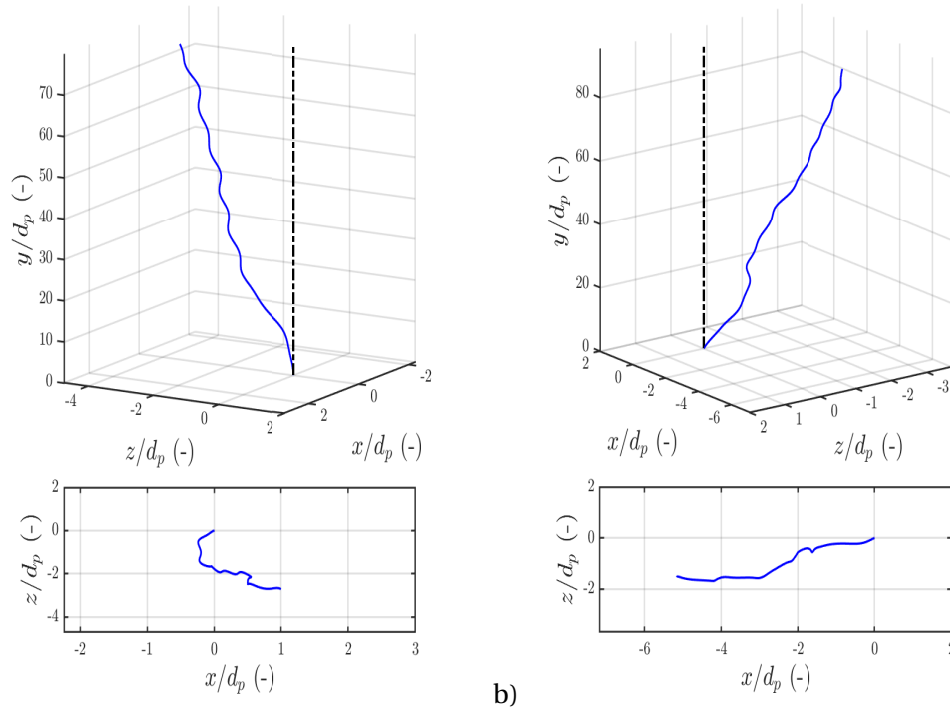


Figure 3.21: a) Trajectory of bi-stable regime for $\bar{\rho} = 0.872$ and $Ga = 307.32$ b) Trajectory of bi-stable regime for $\bar{\rho} = 0.883$ and $Ga = 255.16$

behaviour seen. The discussion is similar to the one presented earlier in this chapter for Fig.3.9.

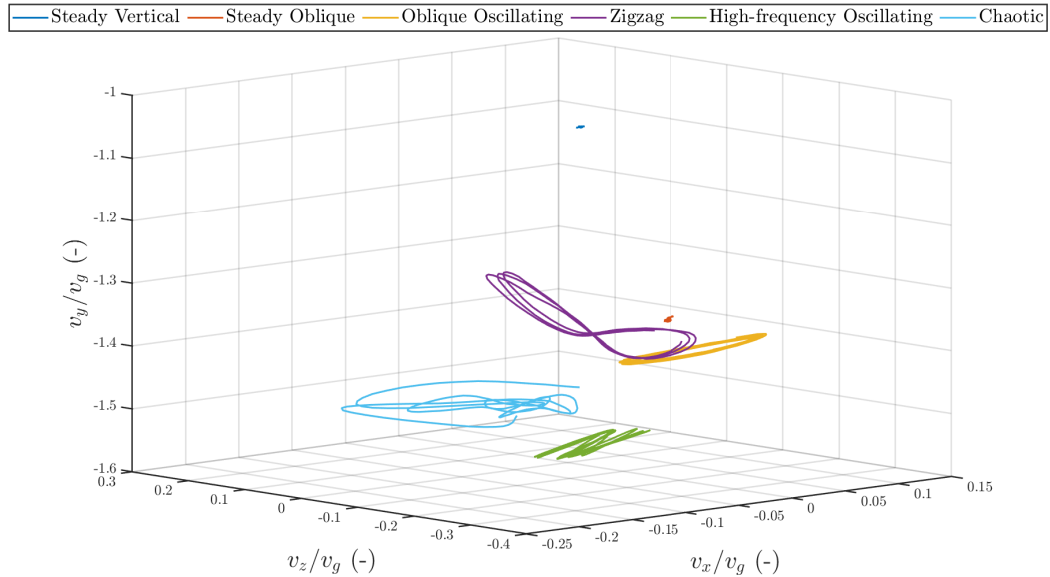


Figure 3.22: 3D velocity plot for all the regimes along line R, with reach regime corresponding to a Ga and $\bar{\rho}$ as follows: Steady Vertical - $Ga = 98.53$ and $\bar{\rho} = 0.878$, Steady Oblique - $Ga = 159.36$ and $\bar{\rho} = 0.892$, Oblique Oscillating - $Ga = 179.54$ and $\bar{\rho} = 0.867$, Zigzag - $Ga = 265.7$ and $\bar{\rho} = 0.874$, High frequency oscillating - $Ga = 279.1$ and $\bar{\rho} = 0.879$, Chaotic - $Ga = 307.32$ and $\bar{\rho} = 0.872$

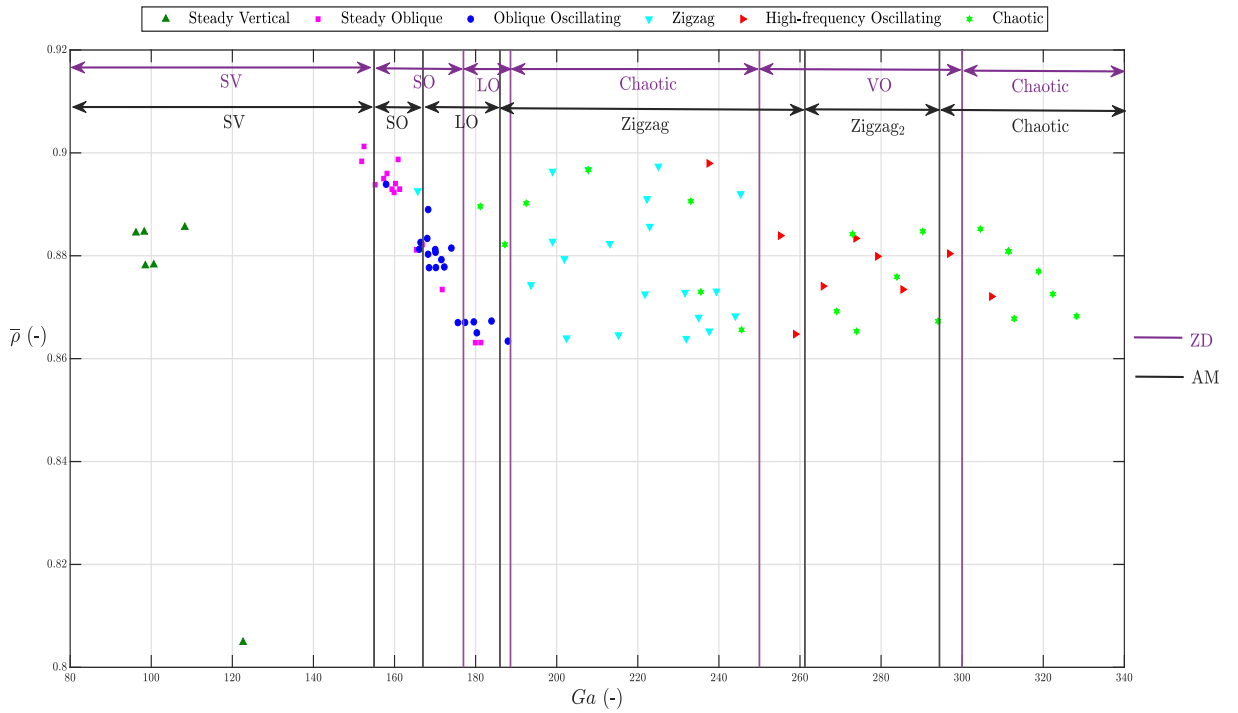


Figure 3.23: $Ga - \bar{p}$ map updated along line R with the results of the present study. The map represents a direct comparison with map of ZD and AM. Violet and black vertical lines represent the thresholds of different regimes from the ZD and AM map respectively, with annotations, SV-Steady vertical, SO-steady oblique, LO - low-frequency oblique oscillating, PO - periodic oscillating (same as LO but named differently by AM) and VO-vertical oscillating

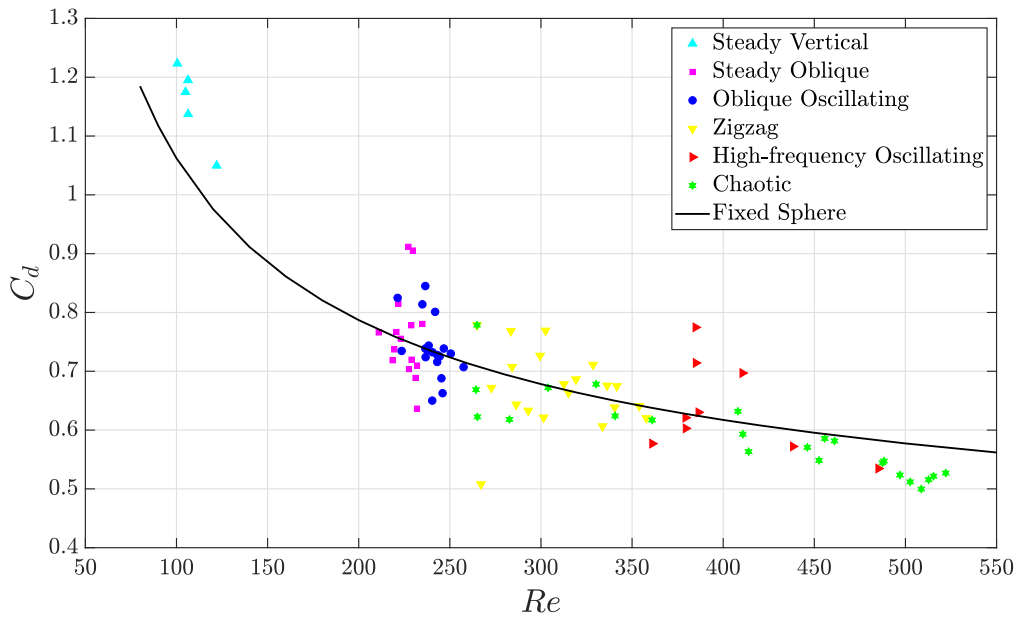


Figure 3.24: C_d plotted for various Re for rising cases (the fixed sphere curve is obtained from the relation proposed by Abraham (Eq1.11)[8])

3.5.1. Drag Curve - Rising sphere

The variation of C_d with Re is shown in Fig.3.24, following the trend of a fixed sphere case. In this case we see a spread of data, at few places being higher and in most places being lower. However, JDB and AM, report higher values of C_d when compared to the fixed sphere for very light rising cases. For the density ratio considered in the present work, JDB and AM report that the C_d will not change much from that of the standard drag curve. The experimental work of Veldhuis et al.[14] also report a spread in the data even after inclusion of uncertainties. However, in the present work, after including the uncertainty, the results agree with the previous works where the trend follows the fixed sphere trend. The plot with the uncertainties included for every case is provided in Appendix D (Fig.D.6). Similar to the discussion for our falling sphere C_d values, after quantifying the uncertainties the values C_d adhere to that of the standard drag curve for fixed spheres.

4

Summary and Conclusions

4.1. Summary

1. An experimental set-up was designed and built from scratch to track the motion of a sphere settling/ascending in a quiescent fluid.
2. High-speed cameras were used to track the motion of the sphere and Particle Tracking Velocimetry was used to reconstruct the position of the sphere and track it in time from the images recorded.
3. A careful design of the release mechanism was made and the effect of the method of releasing on the final trajectory of the sphere was studied. The release mechanism didn't have any noticeable effect of the final type motion taken by the sphere.
4. Uncertainty analysis was performed and uncertainties in Ga , $\bar{\rho}$, Re , C_d and calibration uncertainties were quantified.
5. A wide range of Ga was studied for four different $\bar{\rho}$ thereby covering most regimes reported in literature. This was done by populating the $Ga - \bar{\rho}$ map with over 250 different experimental data sets.
6. For the falling cases, three different $\bar{\rho}$ were studied. Out of the three, one corresponds to the low density case ($\bar{\rho} \approx 1.12$) and two correspond to high density case ($\bar{\rho} \approx 3.19$ and 3.9). The distinction was mainly made because, the transition to chaos is different for the low and high density cases. For rising cases, the transition and path instabilities were studied for one $\bar{\rho} \approx 0.87$.

4.2. Conclusions

1. For the low density falling case ($\bar{\rho} \approx 1.12$), the steady oblique and oblique oscillating were observed consistently for a range of Ga , thereby agreeing with the results of ZD and JDB. These two regimes were also observed experimentally by VB and the steady oblique regime was observed by HW.
2. On increasing the Ga for the low density falling cases ($\bar{\rho} \approx 1.12$), for $250 < Ga < 300$, a high-frequency oscillating regime was observed in the present work. This regime, was not reported by JDB, but reported in their updated work (ZD) and they report this regime for the similar Ga range. However, this is the first time such regime is

observed experimentally. In the present study close to 50 different experiments were conducted in this Ga range and out of the 50, 20 were stable high-frequency oscillating trajectories, whereas 30 were chaotic trajectories. Hence, in the present work, this region of $250 < Ga < 300$ region was deemed as bi-stable, where one can find coexistence of a high-frequency oscillating regime as well as a chaotic regime. Hence, the present work doesn't agree with JDB for $250 < Ga < 300$, but we agree with the map of ZD, except for the fact that the high frequency oscillating regime is characterized as bi-stable in the present work. Although VB didn't cover a wide range of Ga range as done in the present experimental campaign, for all the ranges covered by VB the present work is in excellent agreement.

3. For the dense cases considered ($\bar{\rho} \approx 3.19$ and 3.9), from the range of Ga considered, we initially observe a steady oblique regime and on increasing Ga further, we see a helical/rotating regime. This disagrees with the findings of ZD and JDB as a high frequency oblique oscillating regime is reported by them in these Ga ranges. However, repeated measurements were made and we never did we observe such a regime. The helical/rotating regime was reported by ZD but it occurred after transiting from the high frequency oblique oscillating. Moreover, they characterize the helical/rotating regime as a bi-stable one. An extensive measurement campaign was conducted for the helical/rotating regime and we saw no signs of bi-stability, rather the helical/rotating regime was well repeatable and also stable. Hence for the dense cases, we are in complete agreement with VB, who also reported a steady oblique regime and directly a helical/rotating regime without reporting presence of any kind of high frequency oblique oscillations. The same transition behaviour on increasing Ga is seen in the present work for both the $\bar{\rho} (\approx 3.19$ and $3.9)$ considered, thereby increasing the confidence in the present results.
4. Moreover, on pursuing the helical/rotating regime further, for $Ga > 225$, we observe that the pitch of the helix reduces to almost half of that observed for $Ga < 225$ and oscillations become more pronounced. On increasing it further, close to $Ga \approx 230$, we observe transition to chaotic regime. This Ga of transition matches very well with the critical Ga mentioned by ZD.
5. For rising cases, a single $\bar{\rho} (\approx 0.87)$ was investigated for a wide range of Ga . Here, we have three maps for comparison. We have a better basis for comparison as out of the three maps one corresponds to a completely different research group with a different numerical code employed for the study. The steady oblique and oblique oscillating regimes agree well with all the three works and also with the experimental work of VB.
6. After the oblique oscillating regime, a zigzag regime was observed in the present work. The transition from oblique oscillating to zigzag is reported by JDB and AM. However the limits of the zigzag regime observed by JDB was over a narrow band. We almost see the zigzag regime immediately after the oblique oscillating regime upto $Ga \approx 250$, thereby completely agreeing with AM.
7. For $Ga > 250$, we observe a high-frequency oscillating regime similar to the one observed for the low density falling sphere cases. This regime is also observed experimentally for the first time. This regime also coexists with the chaotic regime thereby making it bi-stable. In some cases, the sphere was in transition to the high-frequency state, where a state of intermediate oscillations was seen. ZD characterizes this regime

as fully stable and strictly vertical(2D) and AM characterizes this as a fully stable high-frequency drifting regime(3D). Although it is tempting to make a small disagreement here, the argument by AM seems convincing, that this regime emerges after a longer distance and is essentially 3D, which may actually be the case if the sphere is tracked after much larger distance of travel, employing a larger tank than the one used in the present work. However, with the results in hand, we quantify this regime as a bi-stable high frequency oscillating regime.

5

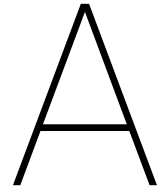
Recommendations for future work

There is great scope for extending the present work and the recommendations are presented below:

1. The effect of moment of inertia on the outliers reported in the updated maps can be studied by characterizing the moment of inertia.
2. Signal processing techniques to correct the drift of the sphere for regimes like the vertical or zigzag regime can be employed [37][30][38]. By doing so, we remove the effect of residual fluid disturbances in the tank and also the effect of inhomogeneities in the sphere, thereby making it readily comparable to numerical results.
3. Dye visualizations can be carried out to obtain qualitative information about the wake structure corresponding to the path instabilities. This is of great importance because, the cause for path instabilities are wake instabilities. Moreover, from a very recent work by Esteban et al. [39], where the entire 3D wake structure of freely falling planar polygons was studied using PIV, it opens doors to exploring the same to characterise the 3D wake structure for falling/rising spheres, which hasn't yet been done experimentally. This will also provide information about the complete flow field, which may help us in understanding the path and wake instabilities better.
4. Only four different $\bar{\rho}$ were considered in this work, a much extensive investigation might prove useful in creating a complete regime map as presented by numerical works. Moreover, for low $\bar{\rho}$ in rising cases, the map of AM and ZD shows much more interesting regimes like spiralling and oblique zigzagging. It is very important to cover these regimes experimentally as for $\bar{\rho} < 0.5$, there is severe disagreement between the maps of AM and ZD. This can be done by using glycerol/water solutions or other heavy oils, from which the lower $\bar{\rho}$ can be studied.
5. A larger tank can be employed with moving cameras since it is important for two main reasons. One being that, by following a sphere from the moment of release, we can get information about the initial path of instability development which finally leads to various regimes of motion. Second one being, it will help to characterize the bi-stable regions better. There is a possibility that the sphere, after a longer distance of travel may become either fully stable or fully chaotic. This was however, tested numerically by ZD for long simulation times and found out that the regime remains bi-stable showing coexistence of both behaviour for long distances too. But it will be

worthwhile to test this fact via experiments and increase the confidence level of the reported results.

6. The present experimental setup and postprocessing tools can also be extended to characterize path instabilities in bubbles, disks, cylinders and spheroids or even to non-Newtonian fluids.



Literature Summary Table

The table summarizes all the literature available for the settling/rising of a single sphere in a fluid at rest. The table has been constructed to provide an overview on the various disagreements in the $Ga - \bar{\rho}$ map. The guidelines to interpret the table is presented below.

1. The first row corresponds to research articles by different groups with the abbreviations being expanded in the key at the left top of the table. Each box in the first row has been coloured green or blue based on the methodology of study (experimental or numerical).
2. Under each column, Ga and $\bar{\rho}$ have been provided to indicate the ranges predicted by the authors for different regimes.
3. The first column corresponds to the various regimes that have been reported in literature and the last box in the first column is the drag coefficient reported.
4. An empty box will indicate that the regime has not been reported by a particular paper. A box may be empty for two reasons. One being that, the $Ga-\bar{\rho}$ in the regime has been investigated, but the corresponding regime has not been observed (coloured in violet). Or, the $Ga-\bar{\rho}$ range has not been investigated and hence the regime is not observed (coloured in red).
5. Also, there is a possibility that the regime is observed, but not for a range of $Ga-\bar{\rho}$ but only at few discrete points due to experimental limitations (coloured in grey).
6. The bistable regions, where coexistence of two regimes is reported has been coloured in orange.
7. Finally, the boxes that are coloured white signify that the regime is observed for a range of $Ga-\bar{\rho}$ and the regimes are in agreement between various works here.

JDB – Jenny et al. (2004), VB – Veldhuis & Biesheuvel (2007), HW – Horowitz & Williamson (2010), ZD – Zhou & Dusek (2015), AM- Auguste & Magnaudet (2018)

SV – Steady vertical, SO – Steady oblique, PO – periodic oscillating, ZZ – zigzagging, ZZO -oblique zigzagging, ZZ₂ – 3D zigzagging, OIT – Oblique intermittent, IT – intermittent, VP – Vertically periodic oscillating, SP -Spiralling or helical, 3DC – 3D chaotic and C_d – drag coefficient

Bi-stable Regions may also coexist as a small part of the regime
 Experimental
 CFD
 Not observed but regime is investigated
 Regime is not investigated and hence not observed
 Observed but as a single data point due to insufficiency of data points (experimental limitation) or only obtained at the single point

| Regime | JDB / UD | | VB | | HW | | ZD | | AM | | Characteristics |
|-----------------|-----------|--|---|---|--------------------------------|--|--|--|------------------------|---|---|
| | p_V/p_r | Ga | p_V/p_r | Ga | p_V/p_r | Ga | p_V/p_r | Ga | p_V/p_r | Ga | |
| SV | 0-∞ | (0 to 155) - (0 to 160) | 2.31 ± 0.05 | 176 ± 11 | 0 - 1.5 All $p_V/p_r > 0.6$ | 0 - 160.74 874.5 - 10000 | 0-10 | 0 - 155.8 | 0.001-0.99 | 0 - 155.6 | For Ga > 874, HW presents a 2R wake structure In this regime HW, shows a R type wake structure through the rise or fall |
| SO | 0-∞ | (155 to 166.9) - (155.8 - 195.7) | 0.56 ± 0.03 | 166 ± 15 | 0 - 0.36 0.36 - 1.5 | 160.74 - 190 (approx.) 160.74 - 380 (approx.) | 0-10 | (155.8 to 167.18) - (155.8 - 195.06) | 0.001-0.99 | (155.6 to 164) - (155.6 to 173) | For ZD and JDB, $p_V/p_r > 2.5$ - high frequency mode (fluid mode), $p_V/p_r < 2.5$ - low frequency mode (solid mode). Bistable regions with chaotic domain exist for density ratio beyond 1.5 and is spread out for further p_V/p_r |
| PO | 0-∞ | Starts from 167 and present until 224 approx. (the spread of data varies with p_V/p_r) | 2.32 ± 0.05 1.32 ± 0.04 | 198 ± 12 195 ± 13 | | | 0-10 | Starts from 167.8 and present until 230 (the spread of data varies with p_V/p_r) | 0.001-0.99 | (164 to 167.3) - (173 to 187.7) | |
| ZZ | 0-1 | Starts from 174 and present until 215 approx. (the spread of data varies with p_V/p_r) | 0.56 ± 0.04 | 198 ± 17 | 0 - 0.36 0 - 0.61 | All Ga > 190 All Ga > 874 | 0-0.5 | Starts from 171 (approx) and present until 200 (the spread of data varies with p_V/p_r) | 0.001-0.99 | Starts from 167.3 and present until 250 (approx.) (the spread of data varies with p_V/p_r) | Usually low frequency, large amplitude oscillations. JDB reported a period doubling/tripling in this regime. - VB reported this regime to be intermittent with the chaotic once and attributed the reason to sphericity. - HW reported a planar, vertical, periodic regime (vibrating regime) |
| ZZO | | | | | | | 0 0.2 0.5 | 175,176 185,190 85,190,195,200 | 0.001-0.175 | Starts from 200 and present until 250 (the spread of data varies with p_V/p_r) | For AM, is periodic planar with non-zero mean drift and combines the characteristics of PO and ZZ. The amplitude is high and nice ZZ - observed |
| ZZ ₂ | | | | | | | | | 0.3-0.99 | Starts from 250 and present until 300 (approx.) (the spread of data varies with p_V/p_r) | The low amplitude/ high frequency ZZ (ZZZ), emerges only after a long travel of 330d, it slowly consistently drifts while ascending and is non-planar. Amplitude is 1 order of magnitude < ZZ - observed. |
| OIT | | | | | 0.36 - 1.5 | 380.6 - 874 (approx.) | | | | | For HW, in this regime the path switches between oblique and rectilinear |
| IT | | | | | | | | | 0.001 - 0.65 (approx.) | Starts from 220 and present until 250 (the spread of data varies with p_V/p_r) | For AM, in this regime the sphere hesitates to perform periodic planar ZZ - onset of chaos. The amplitude of the ZZ here = O(sphere d) and not a function of density ratio . For some cases only, beyond 350d only IT was visible. The intermittency sets in at a higher Ga for increasing the density ratio |
| VP | 0-1 | Starts from 215 and present until 338 approx. (the spread of data varies with p_V/p_r) | | | | | 0.5 - 2 approx. | Starts from 240 (approx) and present until 300 (the spread of data varies with p_V/p_r) | | | This regime - high f, small amplitude, small wavelength, periodic planar trajectory with a non-zero mean horizontal velocity, symmetric vortex shedding and has small/fast oscillations. Within this region also exists a smaller bistable region with chaotic domain |
| SP | | | | | | | 0 0.1 | 375, 400, 500 500 | 0.001-0.2 | Starts from 375 and present until 700 (the spread of data varies with p_V/p_r) | For ZD, the helical regime stands out for an exceptionally large horizontal velocity (30% of the vertical velocity for $p_V/p_r = 0.1$) |
| 3DC | 0-∞ | All Ga upto 350 excluding ones listed in other regimes | 2.33 ± 0.05 0.57 ± 0.04 | 212 ± 13 218 ± 19 | | | 0-10 | All Ga upto 700 excluding ones listed in other regimes | 0.001-0.99 | All Ga upto 700 excluding ones listed in other regimes | Characterized by fully 3D chaotic trajectory with large lateral excursions |
| C _d | | Enhanced values of C _d is observed for Ga > 225 and it was more or less varying around 0.64 up till Ga = 350. | Since different motion of spheres were observed for light spheres, VB agrees the possibility of increasing C _d as reported earlier by others | C _d increases for Ga > 874 or Re > 1550 for very light rising spheres (density ratio 0 - 0.6). C _d in the range of 0.75 | | | Decrease of vertical velocity is found for rising spheres, and decrease being maximum for SP regime. ZD do agree that there will be increase in C _d but they don't agree that the decrease will correspond to the very high C _d reported earlier by others | High C _d was obtained for the spiralling case, here the value was in decent agreement with Veldhuis et al. (2009) and excellent agreement with ZD | | | Although most literature predict higher values of C _d for ascending spheres (especially very light one) there is mild and sometimes large disagreement between different works |

B

Measurement of Sphere diameter

The sphere is kept under a microscope (Fig.B.1 a) and the images in different planes are recorded. The scale factor required to convert from pixel coordinates to real coordinates (mm) is done by imaging a grid of known size under a microscope (depicted in Fig.B.1 b). A circle is fit by Circular Hough Transform method in Matlab. The procedure is carried out individually for all Nylon and Polypropylene spheres.

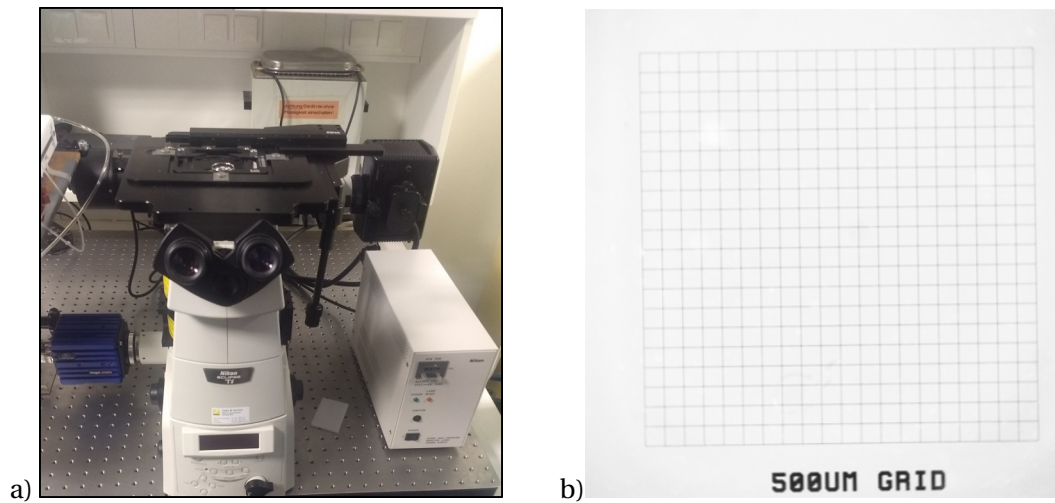


Figure B.1: a)Microscope b) Grid used for calibration (distance between two points is 500 μm)

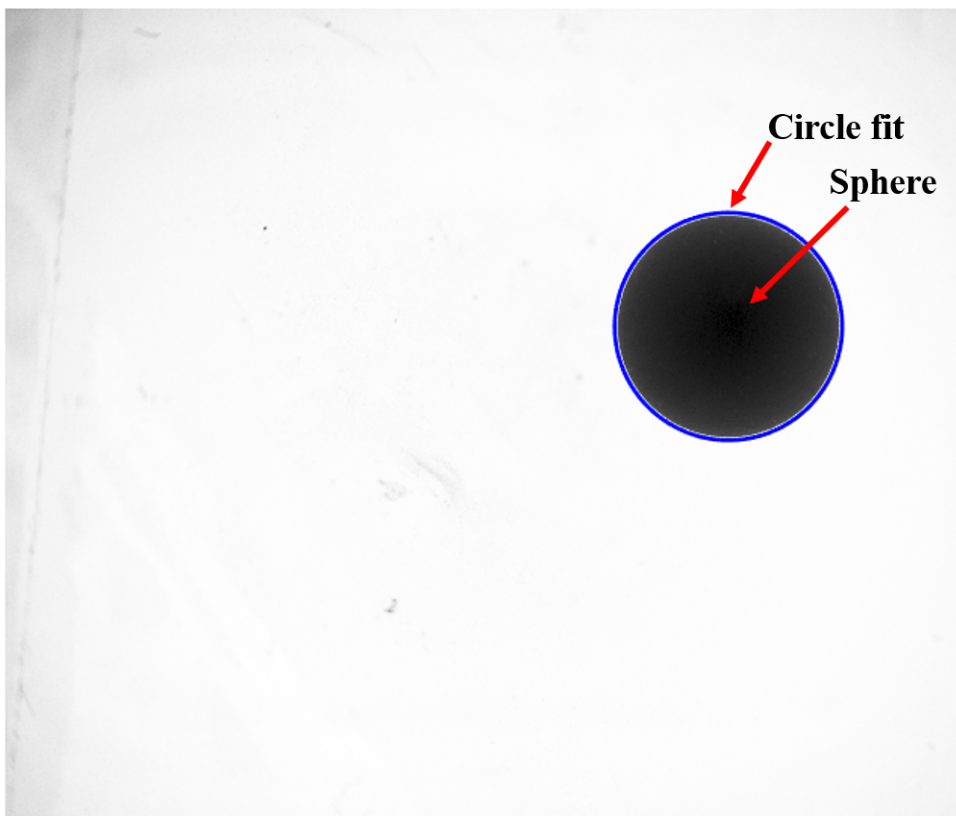
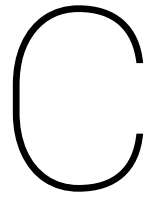


Figure B.2: Nylon Sphere of diameter 3.5 mm viewed under microscope and circle fit (blue line)



Water absorption by the spheres

Mass of the spheres were measured before immersion, after 2 hours and 5 hours of immersion in water. Polypropylene spheres and the ceramic spheres (silicon nitride and aluminium oxide) show no signs of significant water absorption. This is evident from the change in mass with time, which is insignificant. Whereas, for nylon spheres, the absorption is significant, which can cause large deviations in the Ga , hence they were dried in an oven at 40°C and the properties were remeasured.

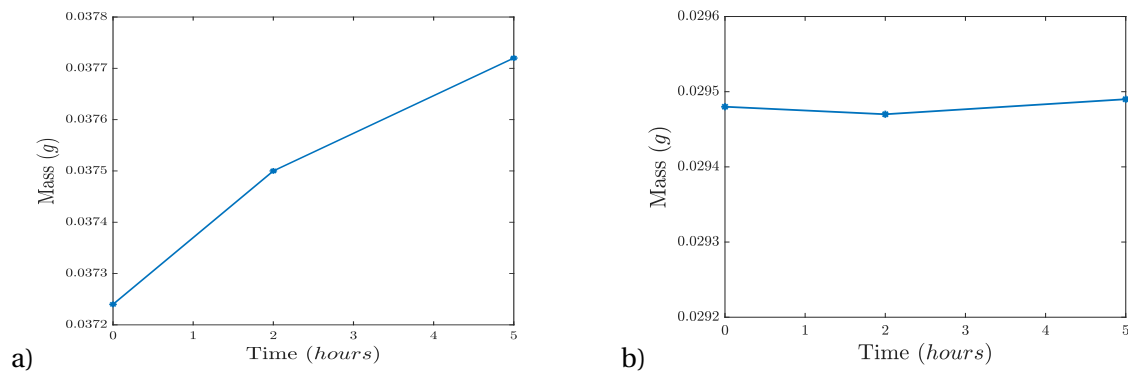


Figure C.1: a) Nylon sphere, b) Polypropylene sphere

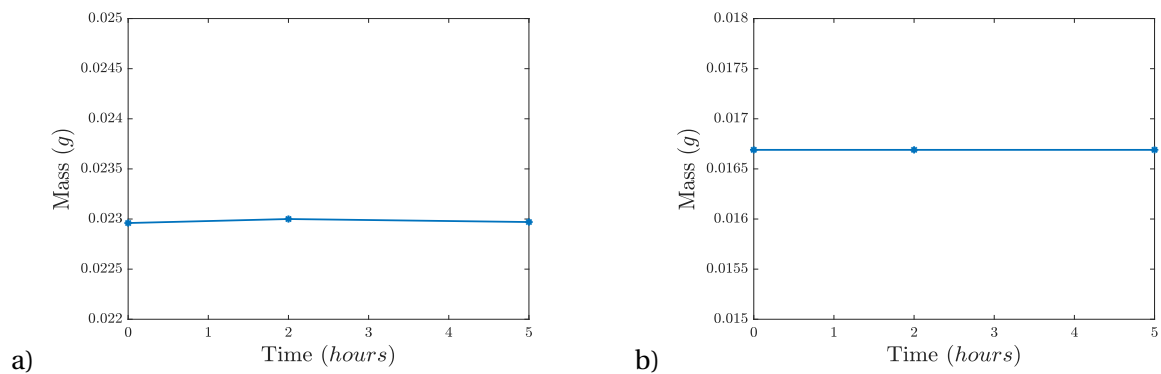
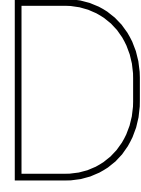


Figure C.2: a) Silicon Nitride sphere, b) Aluminium Oxide sphere



Uncertainty Analysis

The uncertainty in $\bar{\rho}$, Ga , Re and C_d is computed systematically for all the 250 cases in the present study. The expressions for $\bar{\rho}$, Ga and C_d is given by equations 1.1, 1.2 and 1.9 respectively. It is clear that Ga is a function of $(m_p, \rho_f, d_p$ and $v_f)$. Similarly $\bar{\rho}$ is a function of $(m_p, d_p$ and $\rho_f)$. Re is a function of $(\bar{v}_y, d_p$ and $v_f)$ and C_d is a function of $(Re$ and $Ga)$.

Expression for Ga from Eq.1.2 can be simplified and written as,

$$Ga = \sqrt{\frac{m_p g - \frac{1}{6} \pi \rho_f g d_p^3}{\frac{1}{6} \pi \rho_f v_f^2}} \quad (D.1)$$

The estimate of uncertainty in Ga is given by the following expressions:

$$\delta Ga = \sqrt{\left(\frac{\partial Ga}{\partial m_p} \delta m_p\right)^2 + \left(\frac{\partial Ga}{\partial d_p} \delta d_p\right)^2 + \left(\frac{\partial Ga}{\partial \rho_f} \delta \rho_f\right)^2 + \left(\frac{\partial Ga}{\partial v_f} \delta v_f\right)^2} \quad (D.2)$$

The partial derivatives in the above equation are expressed as follows,

$$\frac{\partial Ga}{\partial m_p} = \frac{3g}{\pi \rho_f v_f^2 Ga}$$

$$\frac{\partial Ga}{\partial d_p} = -\frac{3d_p^2 g}{2v_f^2 Ga}$$

$$\frac{\partial Ga}{\partial v_f} = -\frac{Ga}{v}$$

$$\frac{\partial Ga}{\partial \rho_f} = -\frac{3m_p g}{\pi v_f^2 \rho_f^2 Ga}$$

Expression for $\bar{\rho}$ from Eq.1.1 can be simplified and written as,

$$\bar{\rho} = \frac{6m_p}{\pi\rho_f d_p^3} \quad (\text{D.3})$$

The estimate of uncertainty in $\bar{\rho}$ is given by the following expressions:

$$\delta\bar{\rho} = \sqrt{\left(\frac{\partial\bar{\rho}}{\partial m_p}\delta m_p\right)^2 + \left(\frac{\partial\bar{\rho}}{\partial d_p}\delta d_p\right)^2 + \left(\frac{\partial\bar{\rho}}{\partial \rho_f}\delta \rho_f\right)^2} \quad (\text{D.4})$$

The partial derivatives in the above equation are expressed as follows,

$$\frac{\partial\bar{\rho}}{\partial m_p} = \frac{6}{\pi\rho_f d_p^3}$$

$$\frac{\partial\bar{\rho}}{\partial d_p} = \frac{-18m_p}{\pi\rho_f d_p^4}$$

$$\frac{\partial\bar{\rho}}{\partial \rho_f} = \frac{-6m_p}{\pi\rho_f^2 d_p^3}$$

The estimate of uncertainty in Re is given by the following expressions:

$$\delta Re = \sqrt{\left(\frac{\partial Re}{\partial \bar{v}_y}\delta \bar{v}_y\right)^2 + \left(\frac{\partial Re}{\partial d_p}\delta d_p\right)^2 + \left(\frac{\partial Re}{\partial v_f}\delta v_f\right)^2} \quad (\text{D.5})$$

The partial derivatives in the above equation are expressed as follows,

$$\frac{\partial Re}{\partial \bar{v}_y} = \frac{d_p}{v_f}$$

$$\frac{\partial Re}{\partial d_p} = \frac{\bar{v}_y}{v_f}$$

$$\frac{\partial Re}{\partial v_f} = \frac{\bar{v}_y d_p}{v_f^2}$$

The estimate of uncertainty in C_d is given by the following expressions:

$$\delta C_d = \sqrt{\left(\frac{\partial C_d}{\partial Re}\delta Re\right)^2 + \left(\frac{\partial C_d}{\partial Ga}\delta Ga\right)^2} \quad (\text{D.6})$$

The partial derivatives in the above equation are expressed as follows,

$$\frac{\partial C_d}{\partial Ga} = \frac{8Ga}{3Re^2}$$

$$\frac{\partial C_d}{\partial Re} = -\frac{8Ga^2}{3Re^3}$$

The individual uncertainties are computed. The uncertainty in m_p is the value of the reading in the weighing scale with the final weight fluctuating between an interval of ± 0.07 mg. The uncertainty in diameter is the largest contribution to the overall uncertainty especially for the considered spheres of smaller diameter. The uncertainty comes from the the accuracy of circle fitting over the images taken from the microscope also the pixel level errors associated with proper edge detection. The uncertainty is around $\pm 20 \mu\text{m}$. The uncertainty in \bar{v}_y is taken from the systematic uncertainty from the calibration which is ≈ 0.2 mm/s, here we take it as ± 0.2 mm/s. The uncertainty in v_f and ρ_f comes from the uncertainty in temperature which is ± 0.2 - 0.3 °C. In the present work, the experiments are conducted between the temperature ranges of 16-30°C. Hence it was decided to plot the variation of v_f and ρ_f within this temperature interval and fit a line through the points (Fig.D.1).

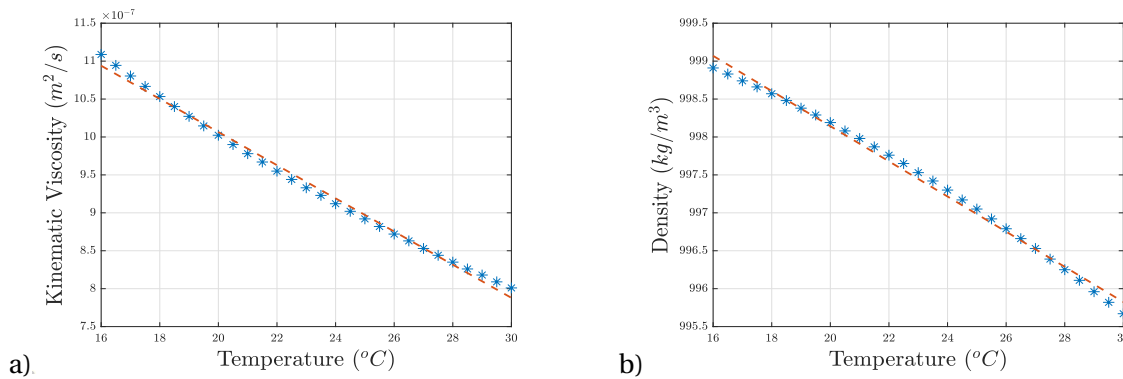


Figure D.1: a) Plot of kinematic viscosity with temperature (red dashed line is the linear fit), b) Plot of density with temperature (red dashed line is the linear fit)

Now the uncertainty in v_f and ρ_f can be obtained from the slope by $\frac{dv_f}{dT} \times \delta T$ and $\frac{d\rho_f}{dT} \times \delta T$ (where δT is the uncertainty in temperature). Hence the uncertainties in v_f and ρ_f are computed to be $\pm 5.6 \times 10^{-9} \text{ m}^2/\text{s}$ and $\pm 0.0464 \text{ kg}/\text{m}^3$ respectively. From the individual uncertainties, the net uncertainty in Ga , $\bar{\rho}$, Re and C_d is computed for every case and the results are plotted below.

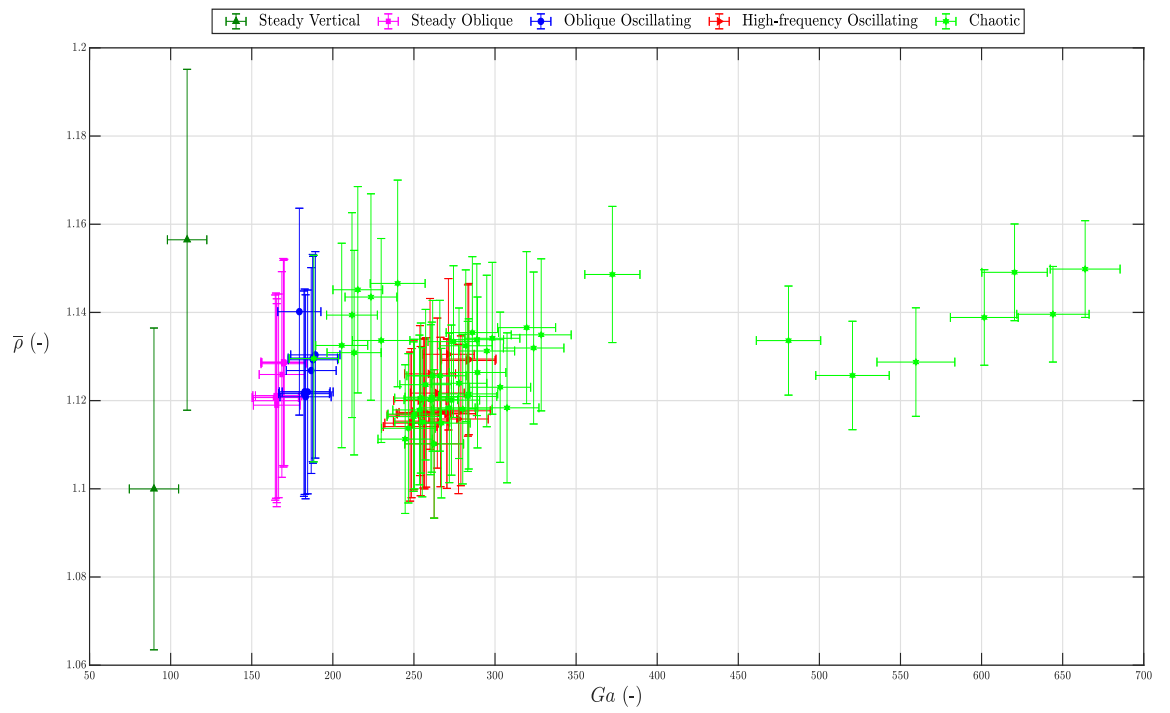


Figure D.2: $Ga - \bar{\rho}$ map updated along line FL with the results of the present study including uncertainties

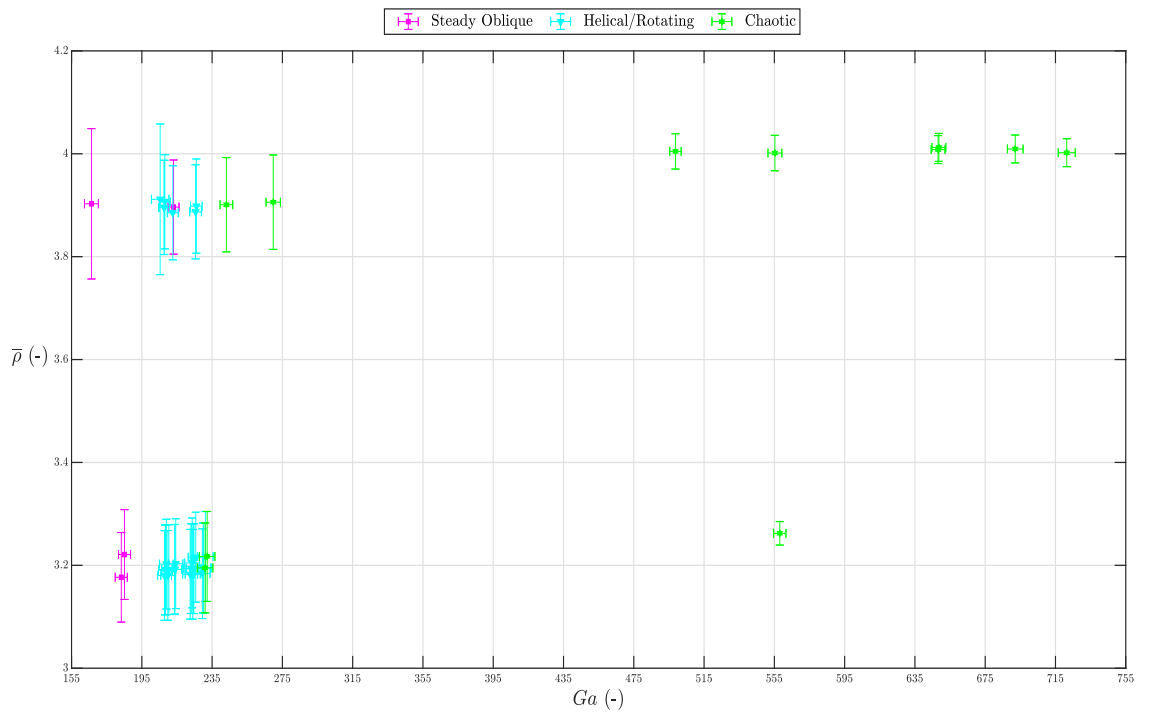


Figure D.3: $Ga - \bar{\rho}$ map updated along line FH1 and FH2 with the results of the present study including uncertainties

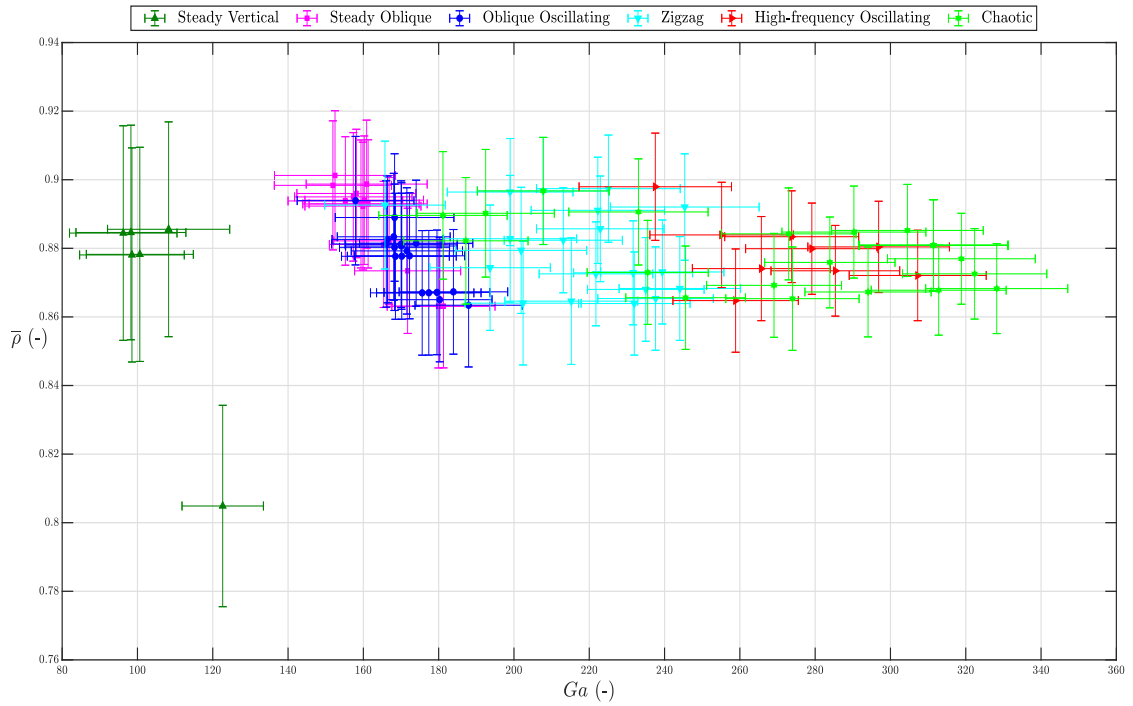


Figure D.4: $Ga - \bar{\rho}$ map updated along line R with the results of the present study including uncertainties

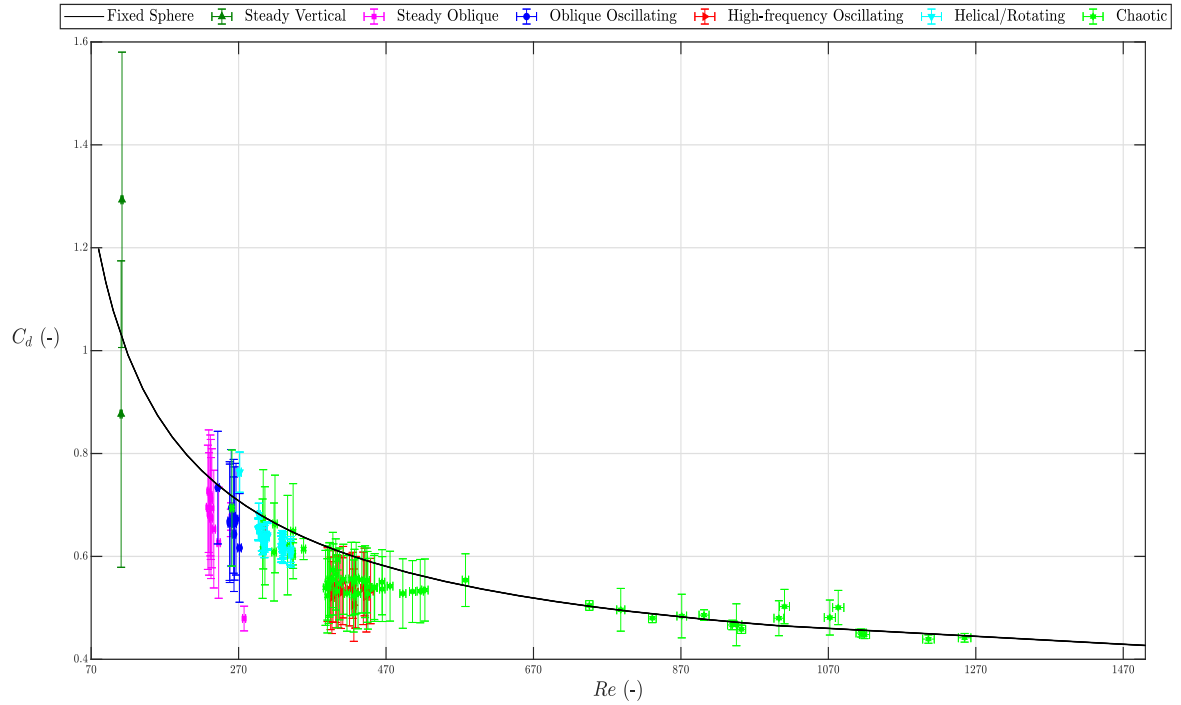


Figure D.5: C_d plotted for various Re for falling cases including uncertainties (the fixed sphere curve is obtained from the relation proposed by Abraham (Eq.1.11)[8])

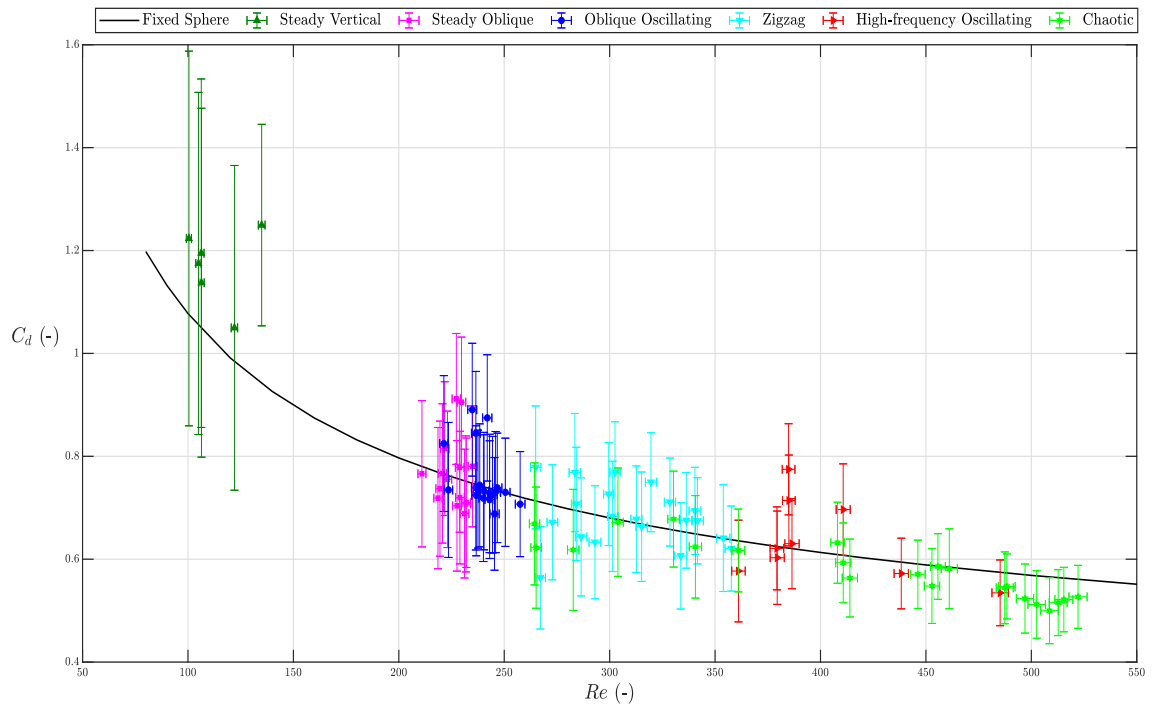
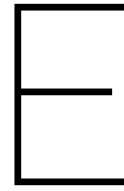
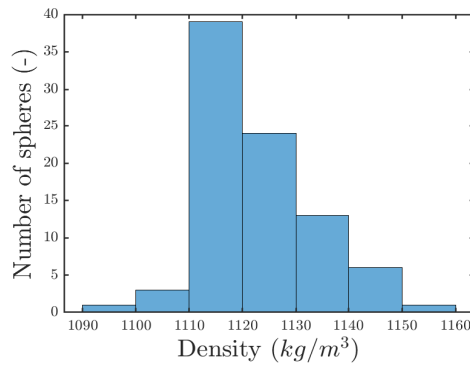


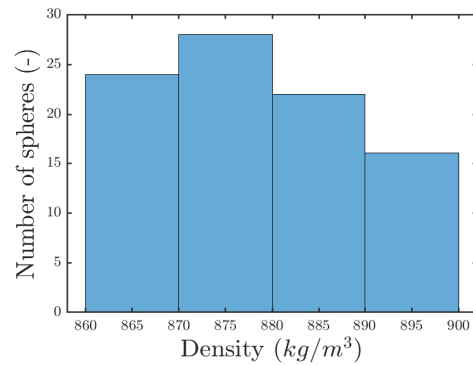
Figure D.6: C_d plotted for various Re for rising cases including uncertainties (the fixed sphere curve is obtained from the relation proposed by Abraham (Eq1.11)[8])



Density variation of Precision Spheres



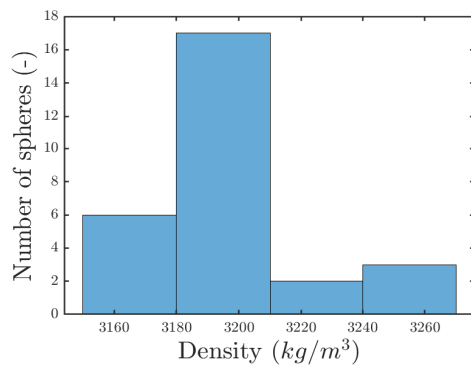
a)



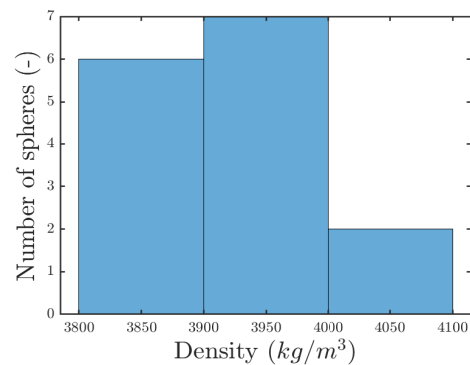
b)

Figure E.1: a) Nylon spheres (total number - 87, density specified by supplier = 1120 kg/m³). Mean density = 1123.7 kg/m³, standard deviation = 9.98 kg/m³

b) Polypropylene spheres (total number - 90, density specified by supplier = 870kg/m³. Mean density = 878.02 kg/m³, standard deviation = 10.65 kg/m³



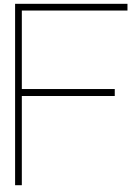
a)



b)

Figure E.2: a) Silicon Nitride spheres (total number - 28, density specified by supplier = 3190 kg/m³). Mean density = 3194.4 kg/m³, standard deviation = 26.04 kg/m³,

b) Aluminium Oxide spheres (total number - 15, density specified by supplier = 3900 kg/m³). Mean density = 3949.4 kg/m³, standard deviation = 54.9 kg/m³



Pseudo Arduino Program

```
#include <Servo.h>
Servo myservo; // create servo object to control a servo
int pos = 0; // variable to store the servo position
void setup() {
  myservo.attach(9); // attaches the servo on pin 9 to the servo object
}

void loop()
{
  Servo servoLeft; // Declare left servo signal
  Servo servoRight; // Declare right servo signal
  //servoLeft.writeMicroseconds(0.0017); // 1.7 ms -> counterclockwise
  //delay(2000);

  for (pos = 90; pos < 180; pos = pos + 1)
  {
    myservo.write(pos); // tell servo to go to position in variable 'pos'
    delay(150 ); // waits 15ms for the servo to reach the position
  }

  for (pos ; pos >=90; pos = pos - 1)
  {
    myservo.write(pos); // tell servo to go to position in variable 'pos'
    delay(150); // waits 15ms for the servo to reach the position
  }
  delay(1000);

while(1)
  {
    myservo.write(pos); // tell servo to go to position in variable 'pos'
  }
} \
```

G

Release Mechanism - Rising Case

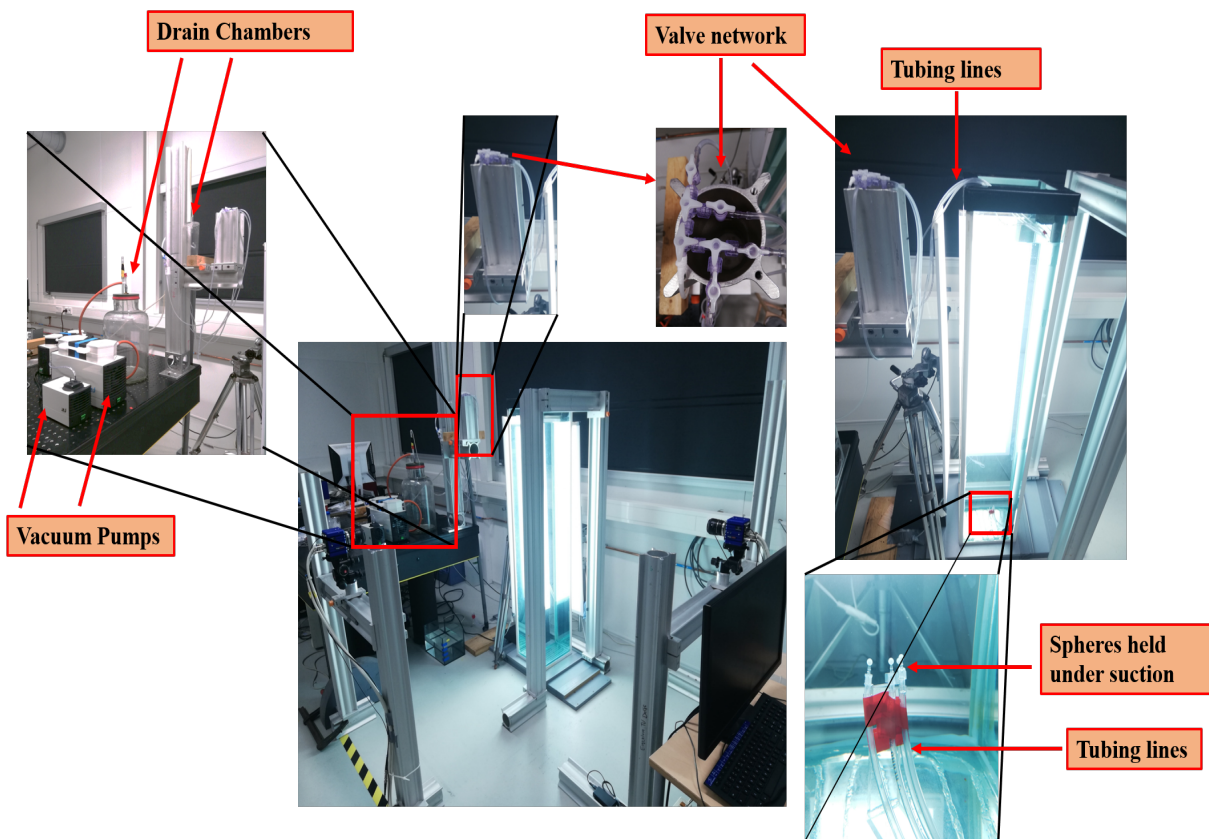
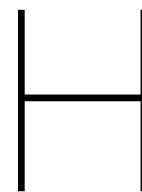


Figure G.1: Release mechanism setup -releasing a sphere from the bottom of a tank



Other Images



Figure H.1: Weighing Scale

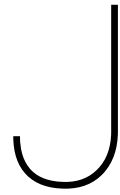


Figure H.2: Individual spheres stored in separate Eppendorf tubes



Experimental Procedure

1. Decide on the desired range of Ga and $\bar{\rho}$ required to perform the experiments. Based on the specifications provided by the supplier, narrow down the sphere material and diameter.
2. This diameter and the mass will have a tolerance and hence the Ga can be potentially off by even 40-50 in number. This is usually not the case for ceramic spheres owing to the high quality (the values specified by the supplier will have very low tolerance). Hence take at least a sample of 10-15 spheres and weigh the mass upto 0.01mg accuracy and measure the diameter using a microscope. With the measured values, the Ga can be predicted.
3. Number each sphere and store them separately as each will have a different Ga and $\bar{\rho}$. Later, when performing the experiments, the required spheres can be chosen as different test cases.
4. The desired Ga can be further tweaked by modifying the temperature of the room. Set the temperature so that the regime can be further narrowed down.
5. Perform calibration of the cameras and leave the cameras untouched post calibration. Provide at least a gap of 2 hours between the calibration and the experiment so that the residual disturbances caused due to the immersion of the grid into the tank in the fluid die down.
6. Synchronize the cameras and set the required frame rate.
7. Release the sphere and record the motion. Provide adequate gap between the experimental runs.
8. With the acquired images, compute the trajectories and other higher-order statistics of motion with the particle tracking code.



Take-aways from doing experiments the wrong way (Experimental Intricacies)

1. Prewetting the sphere - Always pre-wet the sphere before release. This can rule out the possibility of formation of bubbles on the sphere surface which will otherwise be inevitable due to surface chemistry of the sphere. Even the presence of a single micro-bubble will be detrimental to the regime of motion observed.
2. Usage of a screw-micrometer - It is advised not to use a screw-micrometer to measure the diameter of the sphere, especially for plastic spheres like Nylon and polypropylene as it can easily deform the sphere thereby changing it from being perfectly round.
3. Purchasing low spheres of diameter 1mm or lower - Since the present work deals with systematic measurement of mass and diameter for each sphere separately, for spheres with diameter ≤ 1 mm, the weighing scale used, reads erroneous values. This is mainly due to the extremely low weight and hence, a better-quality weighing scale should be used or spheres of greater mass should be used.
4. Cleaning the tank - It is advisable to clean the tank once in 3-4 days. This is due to the increase in contamination with time in still water. The fastest and wise way to remove the water from the tank is to use a water vacuum pump. Once the water is removed, the dust/dirt in the bottom of the tank can be removed using a vacuum cleaner (after water dries out completely). Possibility of using a siphon is not recommended, owing to the long time taken to drain and also due to the decrease in the rate of draining with decrease in head. Possibility of using a hole at the bottom of the tank is ruled out since the tank is made of glass and drilling isn't an option. However, employing a plexiglass tank can overcome this difficulty.
5. Usage of multiple vacuum pumps - For releasing the sphere from the bottom of the tank, since the vacuum pump should be switched on for 2 hours or more, using reserve vacuum pumps is recommended owing to overheating of the vacuum pump with time. Usage of a pressure relief valve in the tubing line to the vacuum pump is also an option to consider.
6. Length of tubing line for releasing spheres from the bottom of the tank - In the present work 4 spheres are held in suction at the bottom and hence 4 different tubing lines are required to independently control the release of each sphere one by one. If the length

of each tubes vary, the distribution pressure distribution along the tubing will also vary there by creating excess pressure in some tube lines where the sphere will not release on closing the valve (it will be held in position owing to the excess suction pressure along the tubing line).

7. Camera synchronization - Using 'Davis' software for recording operation will ensure that the cameras are synchronized automatically. This is because a programmable timing unit (PTU) will be used. But this is not the case when using other software like 'Photron' and 'PCO Camware' where it mandatory to manually synchronize the cameras (by switching on the 'Master' and 'Slave' option). In order to be sure that the cameras are in sync, it is recommended to focus both the cameras simultaneously on a timer and check if the time lapse in the images from both the cameras match up to milli-second level.
8. Obtaining the desired water temperature - Due to the large volume of the tank reaching the desired water temperature will roughly take close to 12 hours. So, it is recommended leaving the air conditioner switch on overnight, to perform experiments the following day morning. Also, set the air conditioner 1 or 2 degrees higher than the desired temperature, to reach the desired temperature the next day morning This is also applicable to lowering the temperature (set the air conditioner 1 or 2 degrees lower than the desired temperature). Moreover, in the multi-meter, set the mode of operation to '3926', the default '385' isn't applicable to the PT-100 sensor that is used in the present work.

Bibliography

- [1] M., Horowitz and C.H.K. Williamson. The effect of Reynolds number on the dynamics and wakes of freely rising and falling spheres. *Journal of Fluid Mechanics*, 651:251–294, 2010.
- [2] C.T., Crowe, J.D., Schwarzkopf, M., Sommerfeld, and Y Tsuji. Multiphase flows with droplets and particles. *CRC Press*, 2012.
- [3] M. Jenny, J. Dušek, and G. Bouchet. Instabilities and transition of a sphere falling or ascending freely in a newtonian fluid. *Journal of Fluid Mechanics*, 508:201–239, 2004.
- [4] M., Uhlmann and T. Doychev. Sedimentation of a dilute suspension of rigid spheres at intermediate galileo numbers: the effect of clustering upon the particle motion. *Journal of Fluid Mechanics*, 752:310–348, 2014.
- [5] Huisman, S.G., Barois, T., Bourgoïn, M, Chouippe, A., Doychev, T., Huck, P, Morales, C.E.B., Uhlmann, M., and Volk, R. Columnar structure formation of a dilute suspension of settling spherical particles in a quiescent fluid. *Physical Review Fluids*, 1(7): 074204, 2016.
- [6] W., Zhou and J. Dušek. Chaotic states and order in the chaos of the paths of freely falling and ascending spheres. *International Journal of Multiphase Flow*, 75:205–223, 2015.
- [7] F., Auguste and J. Magnaudet. Path oscillations and enhanced drag of light rising spheres. *Journal of Fluid Mechanics*, 841:228–266, 2018.
- [8] Farid F Abraham. Functional dependence of drag coefficient of a sphere on reynolds number. *The Physics of Fluids*, 13(8):2194–2195, 1970.
- [9] Zhongli Ji, Zhiyi Xiong, Xiaolin Wu, Honghai Chen, and Hongxiao Wu. Experimental investigations on a cyclone separator performance at an extremely low particle concentration. *Powder Technology*, 191(3):254–259, 2009.
- [10] O’Melia, C.R. Coagulation and sedimentation in lakes, reservoirs and water treatment plants. *Water science and technology*, 37(2):129–135, 1998.
- [11] E. Guazzelli. Sedimentation of small particles: how can such a simple problem be so difficult? *Comptes Rendus Mecanique*, 334(8-9):539–544, 2006.
- [12] P. Ern, F. Risso, D., Fabre, and J. Magnaudet. Wake-induced oscillatory paths of bodies freely rising or falling in fluids. *Annual Review of Fluid Mechanics*, 44:97–121, 2012.
- [13] C.H.J., Veldhuis and A. Biesheuvel. An experimental study of the regimes of motion of spheres falling or ascending freely in a newtonian fluid. *International Journal of Multiphase Flow*, 33(10):1074–1087, 2007.

- [14] C.H.J., Veldhuis, A. Biesheuvel, L. van Wijngaarden, and D. Lohse. Freely rising light solid spheres. *International Journal of Multiphase Flow*, 35(4):312–322, 2009.
- [15] C.E., Brennen. Fundamentals of multiphase flows. *Cambridge University Press*, 2005.
- [16] B., Ghidersa and J. Dušek. Breaking of axisymmetry and onset of unsteadiness in the wake of a sphere. *Journal of Fluid Mechanics*, 423:33–69, 2000.
- [17] R. Mittal. Planar symmetry in the unsteady wake of a sphere. *AIAA journal*, 37(3):388–390, 1999.
- [18] R. Natarajan and A Acrivos. The instability of the steady flow past spheres and disks. *Journal of Fluid Mechanics*, 254:323–344, 1993.
- [19] D., Ormières and M. Provansal. Transition to turbulence in the wake of a sphere. *Physical review letters*, 83(1):80, 1999.
- [20] A.G., Tomboulides and S.A., Orszag. Numerical investigation of transitional and weak turbulent flow past a sphere. *Journal of Fluid Mechanics*, 416:45–73, 2000.
- [21] D. Fabre, F. Auguste, and J. Magnaudet. Bifurcations and symmetry breaking in the wake of axisymmetric bodies. *Physics of Fluids*, 20(5):051702, 2008.
- [22] A.W. Preukschat. *Measurements of drag coefficients for falling and rising spheres in free motion*. PhD thesis, California Institute of Technology, 1962.
- [23] D.G., Karamanev and L.N. Nikolov. Free rising spheres do not obey newton’s law for free settling. *AIChE journal*, 38(11):1843–1846, 1992.
- [24] D.G., Karamanev, C., Chavarie, and R.C. Mayer. Dynamics of the free rise of a light solid sphere in liquid. *AIChE journal*, 42(6):1789–1792, 1996.
- [25] C.H.J., Veldhuis, A. Biesheuvel, L. van Wijngaarden, and D. Lohse. Motion and wake structure of spherical particles. *Nonlinearity*, 18(C1), 2004.
- [26] V., Mathai, X., Zhu, C., Sun, and D., Lohse. Flutter to tumble transition of buoyant spheres triggered by rotational inertia changes. *Nature communications*, 9(1):1792, 2018.
- [27] A., Chouippe, M., Kraymer, M., Uhlmann, J., Dušek, and T., Kiselev, A., Leisner. Heat and water vapor transfer in the wake of a falling ice sphere and its implication for secondary ice formation in clouds. *New Journal of Physics*, 21(4):043043, 2019.
- [28] R., Di Felice and E., Parodi. Wall effects on the sedimentation velocity of suspensions in viscous flow. *AIChE Journal*, 42(4):927–931, 1996.
- [29] Engineering toolbox, 2001. [online] available at: <https://www.engineeringtoolbox.com> [accessed 10/11/2019].
- [30] C., Toupont, P., Ern, and V., Roig. Kinematics and wake of freely falling cylinders at moderate reynolds numbers. *Journal of Fluid Mechanics*, 866:82–111, 2019.
- [31] S.M., Soloff and R., Adrian. Distortion compensation for generalized stereoscopic particle image velocimetry. *Measurement science and technology*, 8(12):1441, 1997.

-
- [32] H.G., Maas, A., Gruen, and D., Papantoniou. Particle tracking velocimetry in three-dimensional flows. *Experiments in fluids*, 15(2):133–146, 1993.
- [33] O.T., Nicholas, H., Xu, and E., Bodenschatz. A quantitative study of three-dimensional lagrangian particle tracking algorithms. *Experiments in Fluids*, 40(2):301–303, 2006.
- [34] B., Daniel and E., Dufresne. The matlab particle tracking code repository. 2008.
- [35] Richard Hartley and Andrew Zisserman. *Multiple view geometry in computer vision*. Cambridge university press, 2003.
- [36] A., Savitzky and M.J, Golay. Smoothing and differentiation of data by simplified least squares procedures. *Analytical chemistry*, 36(8):1627–1639, 1964.
- [37] K., Ellingsen and F, Risso. On the rise of an ellipsoidal bubble in water: oscillatory paths and liquid-induced velocity. *Journal of Fluid Mechanics*, 440:235–268, 2001.
- [38] P.C., Fernandes, F, Risso, P, Ern, and J., Magnaudet. Oscillatory motion and wake instability of freely rising axisymmetric bodies. *Journal of Fluid Mechanics*, 573:479–502, 2007.
- [39] L.B., Esteban, J, Shrimpton, and B, Ganapathisubramani. Three dimensional wakes of freely falling planar polygons. *Experiments in Fluids*, 60(7):114, 2019.